Augmenting Wiring Diagrams of Neural Circuits with Activity in Larval *Drosophila*

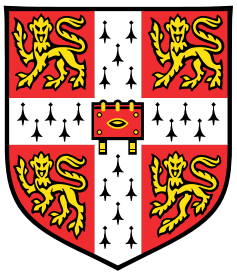

Andrew S. Champion

Department of Physiology, Development and Neuroscience
University of Cambridge

This dissertation is submitted for the degree of
Doctor of Philosophy

Gonville and Caius College November 2020

Declaration

This thesis is the result of my own work and includes nothing which is the outcome of work done in collaboration except as declared in the Acknowledgements and specified in the text. It is not substantially the same as any that I have submitted, or, is being concurrently submitted for a degree or diploma or other qualification at the University of Cambridge or any other University or similar institution except as declared in the Acknowledgements and specified in the text. I further state that no substantial part of my thesis has already been submitted, or, is being concurrently submitted for any such degree, diploma or other qualification at the University of Cambridge or any other University or similar institution except as declared in the Acknowledgements and specified in the text. It does not exceed the prescribed word limit for the relevant Degree Committee. This dissertation contains fewer than 60,000 words exclusive of tables, footnotes, bibliography, and appendices.

Andrew S. Champion
November 2020

Abstract

Augmenting Wiring Diagrams of Neural Circuits with Activity in Larval *Drosophila*

Andrew S. Champion

Neural circuit models explain an animal's behavior as evoked activity of different circuit elements of its nervous system. Synaptic wiring diagrams mapped from structural imaging of nervous systems guide modeling of neural circuits on the basis of connectivity. However, connectivity alone may not sufficiently constrain the set of plausible circuit hypotheses for empirical study. Combining structural imaging of synaptic connectivity with functional information from activity imaging can further constrain these hypotheses to create unequivocal neural circuit models. This thesis develops computational methods and tools to cross-reference structural and activity imaging of explant larval *Drosophila* central nervous systems at cellular resolution. Augmenting synaptic wiring diagrams with activity maps via these methods relates circuit structure and function at the neuronal level on a per-behavior basis.

Neuronal activity of larval central nervous systems expressing pan-neuronal calcium indicators is imaged in a light sheet microscope, which are then structurally imaged with high throughput electron microscopy. Methods and tools are provided for the assembly of these image volumes, spatial registration between imaging modalities, automated detection of relevant tissue and cellular structures in each, extraction of activity time series, and morphological identification of neurons in structural imaging using reference wiring diagrams mapped from other larvae.

Using these methods, existing wiring diagrams mapped from a reference first instar larva were identified with neurons in a larva augmented with activity information for a neural circuit involved in peristaltic motor control. This demonstrates the feasibility of the contributed methods to associate the wiring diagrams of arbitrary circuits of interest with activity timeseries across multiple individuals, behaviors, and behavioral bouts. To

demonstrate capability to augment wiring diagrams with information besides activity, these methods are also applied to multiple larvae each expressing specific neurotransmitter labels rather than calcium indicators in the light sheet microscopy.

This work scaffolds future modeling of circuits underlying behavior that can only be mechanistically understood in the context of multi-modal observation of synaptic connectivity, functional activity and molecular markers. The methods developed also enable comparative connectomics between multiple individuals, which is necessary to study inter-individual variability in circuits and to observe experimental intervention in the development, structure, and function of neural circuits.

To my many teachers, but most of all the first, Sharon, my mother.

Acknowledgements

I have wound in, out, and around research for so long I must first thank those that kept me in its attractor prior to this PhD, especially when it would have been easier to let me escape. The greatest of these is Nancy Nersessian, who at three distinct stages offered mentorship and support to remind me that no path would capture my curiosity if it did not involve the mechanistic basis of intelligence and the embodied computation of life. Between those three stages Ronald McClendon and Walter D. Potter supported my early graduate work at the University of Georgia even when my interests turned away from artificial intelligence, and Kristine Nagel and Lonnie Harvel of Georgia Gwinnett College patiently guided my professional development while allowing me to keep one foot in research. Many faculty during my Masters at Georgia Tech went beyond their responsibilities to pave the peculiar path between computer science and neuroscience I charted that eventually made my work in this PhD possible, but I extend special thanks to May D. Wang and Christopher Rozell for their time and resources.

The joint PhD program between Cambridge and Janelia was one of almost intimidatingly vast resources and possibility. I am grateful and humbled to have taken part and thankful to those who helped me navigate it: Sue Jones, Erik Snapp, Ashley Munteanu, and Aileen Jordan. I am also indebted to Stephanie Young and Kerry Sobieski for their administrative support. I thank Howard Hughes Medical Institute for funding my studentship.

I spent many years knocking on the inboxes of connectomics community, so special acknowledgement must go to Albert Cardona not only for the years of work he has facilitated as my PhD supervisor, but also as the person to finally grant me an opportunity in this field. I thank my advisors both for their guidance and the role models of scientific and personal excellence they have provided: Stephan Saalfeld for his clarity in winnowing what matters from what does not and as a model of how to build tools that extend the reach of feasible science; Kristin Branson for building the most rigorous yet most interdisciplinary and pedagogical machine learning community I have encountered; and Richard Adams for his generous time spent helping me develop perspective, adaptability, and contingencies in my plans early during my PhD. From Cambridge I also thank Stephen Eglen for his valuable

feedback during my first year assessment and David Parker for the generous accommodation in his lab during my transition from Janelia.

All work is collaborative, and I have had the benefit of sharing labors with people much stronger and more skilled than myself. Nadine Randel brought this project into existence, performed all bench work for dissection, fixation, and staining, and organized all imaging. Without her data I would be hopeless, and she has contributed neuroscientific expertise to strategy, data annotation, analysis, and interpretation at nearly every stage. Song Pang and Shan Xu from the lab of Harold Hess provided state of the art electron microscopy. Raghav Chhetri and Chen Wang from the lab of Philipp Keller provided light sheet microscopy and data preprocessing, and their labmate Léo Guignard performed additional data processing. Fellow current or former Cardona lab members Stephan Gerhard, Casey Schneider-Mizell, Christopher Barnes, Katharina Eichler, and Tom Kazimiers worked on many requisite and related projects and datasets, and were indispensable sources of feedback, critique, and support. Rebecca Arruda annotated several datasets in this project, and William Patton contributed to segmentation tools. Michael Winding of Marta Zlatic's lab created crosses for neurotransmitter labeling and collaborated on the annotation of reference landmarks for the larval ventral nerve cord. Philipp Hanslovsky and John Bogovic from the Saalfeld lab provided generous support and assistance for their tools.

Beyond the professional community above, I would never have made it into or through this PhD without astounding personal support. The sacrifices some made to carry me through are so great that listing them here could only be inadequate. To those people, thank you.

Table of contents

List of figures

List of tables

Acronyms

CATMAID the Collaborative Annotation Toolkit for Massive Amounts of Image Data. 20, 25–27, 29, 31, 32, 39, 41, 51, 55, 61, 64

CNN convolutional neural network. 15, 28, 44

CNS central nervous system. xiii, 1, 6, 7, 9, 15–17, 23, 28–30, 34, 40, 45–50, 52–55, 57, 60, 67

DnB down-and-back neuron. 12, 13

EM electron microscopy. 46, 47, 51, 54, 60, 61

FFN flood-filling network. 30, 31, 38, 41, 42, 44

FIBSEM focused ion beam scanning electron microscopy. xiii, xv, 7, 9, 18, 20–25, 29–31, 34, 35, 37, 40, 43, 45–56, 61, 62, 65

GFP green fluorescent protein. 49

GPU graphics processing unit. 15, 28, 30, 44, 51

ISNR inter-segmental nerve root. 29

ISNR-a anterior branch of the inter-segmental nerve root. 29, 30

ISNR-p posterior branch of the inter-segmental nerve root. 29, 30

KLB Keller lab block format. 51

LSM light sheet microscopy. xv, 8, 15–17, 19, 23, 28, 35, 37, 43, 45–57, 60

NB neuroblast. 59, 61, 62

RFP red fluorescent protein. 51

SEZ subesophageal zone. 12, 34

SIFT scale-invariant feature transform. 24

SNR segmental nerve root. 29, 30

SPIM selective plane illumination microscopy. 15

ssTEM serial section transmission electron microscopy. 7, 9, 16, 24, 29–31, 33, 35, 41, 42, 64

SVM support vector machine. 28, 38, 40

VNC ventral nerve cord. 11, 12, 28, 33, 38, 46, 48, 52–56, 59, 61

WASM web assembly. 26

Chapter 1

Introduction

Study of the mechanisms of neural systems has principally operated from two regimes of observation: structure and function. When studying neural systems from a circuit perspective at cellular resolution, these regimes most often correspond to observation of the structure of neuronal morphologies and synaptic connectivity, and observation of the functional dynamics of ions or transmitters via fluorescent indicators or electrophysiological recordings. Much work has modeled the relationship of structure and function within neural circuits, particularly the inference of one from the other, such as simulation of compartment or cellular ion dynamics in neural circuit graphs, or statistical inference of structural connectivity on the basis of observed activity. In contrast, the goal of this thesis is to contribute methods for the joint observation of structure and function, so that rather than being only independently useful to model one modality from the other, they are jointly useful to constrain, model, and explain neural circuits as the mechanistic basis of behavior. Further aims of these methods are to allow this joint observation at scales and scopes comparable to those of structural observation of synaptic wiring diagrams. That is, these methods allow observation of entire systems, namely the entire central nervous system of larval *Drosophila melanogaster* (henceforth *Drosophila*), do so at the resolution of individual neurons, and do so with completeness approaching pan-neuronal.

To perform these observations efficiently for many behaviors, behavioral bouts, and individual animals to permit sufficient observation of the variable dynamics of function, this is not a direct joint observation of activity and synaptic connectivity in a single animal. Rather, the methods jointly observe activity and partial structural information in one animal to allow the mapping of observed activity onto the complete synaptic wiring diagram of a reference animal. I refer to this combination as an *activity-augmented wiring diagram* because it augments the adjacency matrix of the wiring diagram with data of identical dimension with respect to neuronal identity, but data of a different type and origin sample. This nomenclature

emphasizes the central role of the wiring diagram in providing a common reference to index, structure, and develop models integrating dense, multi-modal observation of neural circuits.

To motivate combining connectivity and activity constraints for neural circuits models, consider the coordination of peristaltic motor control in larval *Drosophila*. Motor systems must integrate control from disparate inputs – action selection, central pattern generation, proprioception, somatosensation, and local dynamics – into coordinated behaviors. Motor systems must also support a variety of behaviors while for each specific behavior efficiently reusing control components, such as musculature, circuitry, and sensory afferents [1]. Though the animal's repertoire may include *antagonistic behaviors* – behaviors which are mutually exclusive in time as they require incompatible dynamics or motion – this coordination and modular reuse must produce decisive, efficacious behavior [2]. In larval *Drosophila*, many neuronal motor control circuits triggering a specific locomotive behavior or modulating specific actuations have been described, yet study of mechanisms and loci coordinating these per-behavior circuits are generally limited to single pathways of competitive inhibition for specific pairs of antagonistic behaviors. This is a consequence of the difficulty and time required to functionally dissect the circuit via experiments which target only few or single neurons. Thus these models incorporate only a sparse subset of the motor control circuitry, while the functional role of most circuit elements and consequently the dynamic regimes of motor circuitry as a whole remain unknown. A more exhaustive inventory of mechanisms that selectively recruit and coordinate modulatory circuitry between distinct motor behaviors would provide insight into how these circuits are reused. Such an inventory would also establish what modulatory capabilities descending control exercises beyond action selection. Activity-augmented wiring diagrams enable such analysis because they provide observation of which circuit elements are active in each behavior, during behavioral transitions, and the correlation of circuit dynamics with behavioral modulation. In contrast, unaugmented wiring diagrams either require extensive theoretical analysis and speculative modeling, incidental prior knowledge of functional correlates of specific circuit elements, or numerous and resource intensive targeted experiments to produce a similar analysis of circuit modularity and function.

To introduce the contributed methods, the remainder of this chapter elaborates the stated problems in reverse order: the non-triviality of mechanisms for coordinating distinct motor behaviors and modulatory control, the difficulty of disambiguating competing neural circuit models of coordination mechanisms via single observation modalities, and the difficulty in combined multi-modal imaging at the scope of whole organisms, systems, or circuits.

1.1 Coordinating Motor Control in Larval *Drosophila*

The *Drosophila* larva is a good model for analyzing circuitry underlying motor behavior selection and coordination because its biology and experimental tools developed around it allow the study of systems-level questions through tractable cell-level manipulation and observation. The nervous system of the larva is small in cell count and physical extent, yet stereotyped for inter-individual study and homologous for inter-species comparison [3]. This reduced complexity makes system-spanning neural circuits tractable to image with electron microscopy [4]. Cell-type specific genetic tools in *Drosophila* allow targeting few or individual neurons for mutation or protein expression [5], and these interventions can be screened with automated behavior observation and analysis [6]. The larva's performance of fictive locomotion in ex vivo preparations [7] makes the entirety of these circuits amenable to activity imaging and electrophysiology.

To identify a circuit that coordinates other modulatory circuits between two motor behaviors, a fruitful strategy is to choose a set of behaviors that are known to recruit an intersecting set of musculature, yet the dynamics of the recruitment are incompatible between behaviors. Antagonistic behaviors are a subset of these behavioral pairs. That is, if two motor behaviors require related but conflicting motion, there must be some coordinating circuitry to inhibit the pertinent modulatory circuitry of the conflicting behavior, but also the possibility for partial or selective recruitment of that same modulatory circuit for the active behavior. By this criterion, circuitry controlling the propagation of the peristaltic wave in the *Drosophila* larva is a good candidate for studying coordination of modulatory control.

Larvae crawl forward by sequentially contracting their body segments in a peristaltic wave from tail to head [8]. Backward crawling functions similarly with a contraction wave from head to tail. The timing of the anterior wave propagation for forward peristalsis is modulated by a segmentally repeating circuit which relaxes the body segment anterior of the contraction wave front using premotor proprioception [9, 10]. This is necessary for fast and robust forward crawling. The posterior wave for backward peristalsis is modulated by an analogous circuit, which also inhibits the anterior wave propagation circuit to prohibit forward crawling [11]. However, this does not establish an unequivocal mechanism of coordination between forward and backward locomotion, as other pathways between the putative backward command neurons and the anterior wave propagation circuitry are known but functionally uncharacterized because they are not amenable to targeted genetics. The unidirectional nature of the circuit model also lacks a mechanism preventing interference from backward circuitry during forward crawling, and no mechanism by which other antagonistic behaviors such as rolling participate in mutual exclusion has been identified. Further, in backward peristalsis there is a phase offset between the dorsal and ventral contraction, unlike

in forward peristalsis where they are synchronized [12]. A specific set of interneurons has been identified as modulating the activity of premotor neurons to affect this phase offset [13], but they are distinct from the wave propagation coordination pathway [14]. Therefore the mechanisms coordinating recruitment of these multiple pathways and the control motif they employ – whether via central pattern generation, distinct command pathways, local dynamics among premotor neuron population, or other possibilities – remain elusive.

A neural circuit model accounting for peristaltic coordination is elusive not only because multiple pathways modulating individual aspects of control have no known coordination mechanism, but also because existing models only include a small portion of the motor system. 118 hemisegmentally repeating premotor neurons have been identified [14], while the models cited above account for approximately 19. While it is possible this majority population of premotor neurons is vestigial or quiescent, recruited only during other behaviors from the larva's modest repertoire, functional only for behavioral modulation necessary outside of laboratory experimental contexts, or simply functional adult neurons generally irrelevant during the larval stage, these are all unlikely given the demonstrated inductive heuristic of wiring and neuronal efficiency [15]. This incompleteness is evident not only from populations, but also from control mechanisms for other aspects of motor execution yet to be described. Circuit mechanisms known to control other aspects of forward peristalsis, such as the proprioceptive lateral amplitude control circuit [16], are likely to have a analogous functional role in backward peristalsis. Such mechanisms, their coordination path with other modulatory circuits for backward peristalsis, and their coordination pathway with lateral amplitude control for other behaviors have yet to be identified.

Motor control circuitry in larval *Drosophila* is surveyed in more detail in Section 2.1.

1.2 Disambiguating Competing Models of Neural Mechanisms

Peristalsis in *Drosophila* larvae illustrates a recurring challenge to explaining behavior via neural circuit models. While sub-circuits synaptically proximate to sensation and motor output are amenable to experimental tools and modeling, and the models are both predictive and explanatory, the same does not necessarily apply when the methods are applied to whole systems. The above discussion of peristaltic motor control has shown existing circuit models account only for a small percentage of the premotor neuron population. This suggests that the mechanisms to simultaneously recruit the many described pathways for antagonistic behavior coordination must in part be distributed among this larger premotor population

or synaptically further removed in the circuit. That is, coordination of motor control for antagonistic behaviors is achieved at the scale of the motor systems. Yet at the scale of systems, models are often under-constrained. Many hypothetical circuit mechanisms could underlie observed behavior because of the high dimensionality of the circuit hypothesis space and limited information in the behavioral output and stimulus control. Consequently the likelihood is greatly decreased that models' predictions generalize or that their functional interpretation corresponds with the modeled system in an explanatory manner.

The size of the space of plausible hypotheses when constrained only by behavioral output and sparse observation of neuronal activity and structure may also make it infeasible to empirically test an unequivocal neural circuit mechanism hypothesis. In the case of peristaltic motor control, the circuit mechanism hypothesis space is large because coordination could occur centrally for the whole organism, local to each body region, within the premotor neuron population, or in multiple stages throughout any subset of these loci. Each source of descending control or proprioceptive sensory input may target subsets of these loci independently. Likewise the mechanism of integration for each could be convergence, competitive inhibition, or many other network motifs. Electrophysiology and genetic behavioral screens can inform how individual circuit elements participate in a specific behavior, but the combinatorial number of possible control circuits, loci for coordination, and interfering dynamics make it intractable to functionally distinguish all plausible mechanisms for selection and coordination across behaviors.

Imaging contributes information which constrains the space of plausible neural circuit mechanism hypotheses. For example, activity imaging contributes functional information that constrains dynamics, which is one projection of the space of possible circuit mechanisms. Thus functional information constrains the set of plausible mechanisms. As the circuit models above have demonstrated, this is also the case for structural imaging which contributes information about neuronal connectivity: while multiple hypothesized control models may explain some motor behaviors and modulation [17], neuronal motor control circuitry concretely establishes which are structurally plausible [18]. When imaging with a single modality, however, the remaining space of plausible circuit mechanism may still be intractably large because it is only constrained by one projective aspect. In the case of structural imaging, a single neuronal circuit can underlie many regimes of functional dynamics [19]. Dynamics are even less constrained when the neuronal circuit is abstracted to a circuit wiring diagram. Likewise one functional activity observation can be realized by many distinct circuits, especially when activity is observed via low temporal resolution integrative indicators.

While a single observation modality may not sufficiently constrain the mechanism hypothesis space, the intersection of multiple modalities may. That is, constraints on plausible mechanisms from the structural information of wiring diagrams can be combined with constraints on dynamics from the functional information of activity maps. The intersection of those two sets of constraints may yield a set of plausible hypotheses of mechanisms small enough to be distinguished with a tractable number of experiments such as behavioral assays or electrophysiology.

Constraining mechanism hypotheses via intersections of multi-modal imaging generalizes to information besides ion activity indicators. Labeling neurons in wiring diagrams with neurotransmitters, gene expression, and other molecular markers reduces the set of compatible mechanism hypotheses. Methods to identify these properties for individual or sparse subpopulations of neurons usually employ the same genetic tools and imaging techniques as activity imaging, and therefore face the same time and resource constraints previously described.

1.3 Combined Functional and Structural Imaging of Neural Circuits

When interest in electron microscopy based connectomics resurged in the last two decades, early work included joint observation of connectivity and functional imaging [20]. However, this was only done for sparse or specific neurons in order to demonstrate the correlation of observed synaptic connections with evoked post synaptic activity – that is, to study the correlated information of wiring diagrams and activity dynamics rather than their independent components. Much of the power of connectomics to predict and explain previously opaque systems, computations and behaviors is due to the density or completeness the wiring diagram, which allows the data itself to guide circuit discovery and modeling when prior hypotheses from other methods are incomplete, incorrect or unavailable. Expanding the explanatory and predictive power of wiring diagrams by augmenting them with activity information should strive for a similar degree of completeness and density in the joint observation of activity.

Directly combining activity and structural imaging is challenging because of conflicting practical limitations of each modality. Activity imaging of fluorescent calcium indicators throughout the central nervous system at single-cell resolution is feasible in explant preparations [21]. The viable time window for motor behaviors in such preparations, as well as the need to induce motor behaviors via opto- or thermo-genetic stimulation of driver line targeted sensory neurons that may evoke only a limited repertoire of behaviors, require imaging

of multiple animals to acquire sufficient functional information. However, EM structural imaging at resolution sufficient to reliably reconstruct synaptic connectivity, as well as the reconstruction process, is time- and resource-intensive. Typically only one or few animals are imaged and used to study multiple research questions over many years. While functional and structural imaging could be performed in different larvae, cellular identity cannot be reliably mapped between modalities because most observed fluorescence is somatic, which are ambiguously localized between individuals.

Instead, following activity imaging larvae can be imaged with low-resolution, high-throughput structural imaging which, while insufficient for synaptic reconstruction, is sufficient to reconstruct morphology of primary, low-order neuronal processes. This data acquisition process is shown in Figure 1.1, and was conducted by Nadine Randel via a collaboration with the laboratories of Harold Hess, Philipp Keller, and Marta Zlatic. An explant larval CNS expressing the pan-neuronal fluorescent calcium activity indicator (either GCaMP6s [22] or jRGECO1a [23]) is imaged in a multi-view, multi-objective light sheet microscope [24]. In addition to spontaneous activity observation, optogenetic activation with Chrimson or Chronos [25] of Basin neurons, which integrate nociception and mechanosensation, can evoke fictive locomotion including peristalsis, bending, and hunching [4]. Following activity imaging the CNS is fixed, stained, and imaged via focused ion beam scanning electron microscopy (FIBSEM). FIBSEM of whole CNS samples of this size is possible due to recent advances minimizing restarts or other artifact-inducing process limitations [26]. Activity information acquired from each CNS can then be used to augment the wiring diagram of a reference CNS acquired via serial section transmission electron microscopy (ssTEM). This ssTEM dataset has proven sufficient for identification, mapping, and analysis of neural circuits involved in proprioceptive modulation and motor program selection [4, 9, 27, 28, 11, 13, 14].

Figure 1.2 overviews the methods and data flow of this process. Morphology of primary, low-order processes is stereotyped for each neuronal cell type in *Drosophila* larva, allowing identification of each neuron in the FIBSEM volumes with existing reconstructions from the ssTEM reference animal. This reference dataset is imaged at resolution sufficient to identify synaptic connectivity and reconstruct circuit wiring diagrams. On the basis of this cell type identity mapping, per-behavior activity time series for each neuron can be cross-referenced with mapped circuit wiring diagrams to intersect constraints from connectivity with those from dynamics, limiting the space of plausible circuit mechanism hypotheses. Properties of cellular identity relevant to circuit function are conserved across development and between individual larvae [28], so although functional and connectivity information are acquired

from different animals, they can be integrated in a way meaningful to understanding circuit mechanisms. Further details of specific processes are elaborated in their respective chapters.

1.4 Structure of This Thesis

Chapter 2 surveys literature spanning all aspects of this thesis across two scopes. The first is background pertinent to the problem domains of the developed methods but not specifically employed in the chosen approach. The second is methods, analyses, and results employed if they apply to the broad scope of the thesis rather than individual aspects covered in later chapters. Background specific to the employed methods or topic of each chapter is instead covered there. Alternative approaches to cross-reference connectivity and activity information about neural circuits or multi-modal imaging are also discussed.

Chapter 3 introduces methods for establishing neuronal identity from high-throughput electron microscopy. This includes tools for aligning, inspecting and annotating these data; using segmentation to accelerate reconstruction of neuron morphology; registration and algorithms for matching near-complete populations of neurons in multiple electron microscopy volumes based on morphological stereotype; computer vision algorithms to detect relevant tissue structures and nuclei; and computational techniques to automate categorization of cell types. Challenges in the imaging and analysis related to the sample condition following light sheet microscopy are identified, their impact on the viability of the overall augmentation method are discussed, and future directions for refinement are proposed.

Chapter 4 introduces techniques for matching neuronal somatic signals in light sheet microscopy with morphological reconstruction in electron microscopy. Several methods of multi-modal image registration are compared, including their impact on the accuracy of somatic activity extraction from the activity imaging.

The developed methods are applied in Chapter 5 to circuits involved in peristaltic motor control. To demonstrate capability to augment wiring diagrams with information besides activity, these methods are also applied to larvae expressing fluorescent labels for specific neurotransmitters rather than calcium indicators in the LSM.

Chapter 6 summarizes methods contributed by this thesis and results of their application to motor control circuits and neuronal neurotransmitter identification in larval *Drosophila*. Problems encountered and consequent recommendations for future work are discussed.

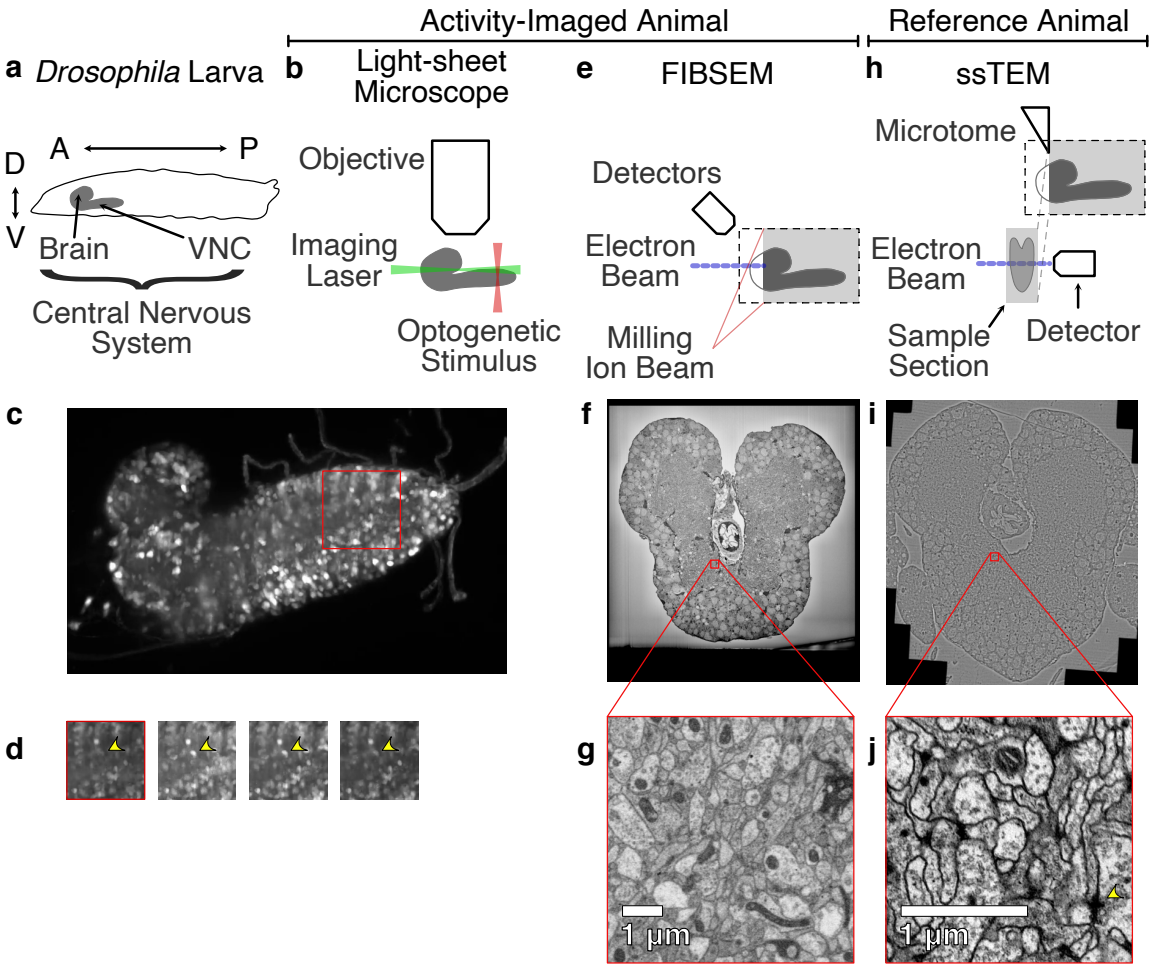

Fig. 1.1 Data Acquisition Process for Augmenting Wiring Diagrams in Larval *Drosophila*. **(a)** Cartoon of the *Drosophila* larva showing the body profile and approximate location of the CNS. In this and all other figures A, P indicate the anteroposterior axis while D, V indicate the dorsoventral axis. **(b)** Cartoon of light sheet imaging of a CNS explant. An illuminating laser light sheet sweeps the sample while an objective and camera image from an orthogonal direction. Simultaneously the CNS may be optogenetically activated on another light frequency. An example perspective rendering of a light sheet volume is shown in **(c)**, with **(d)** showing a timeseries of transient activation of a motor neuron (yellow arrow) during fictive behavior. **(e)** Cartoon of FIBSEM imaging of the CNS. An electron beam scans the block-face of the embedded sample while detectors collect reflected and scattered electrons. Once finished, an ion beam mills material off of the block-face surface. An example image is shown in **(f)**, with full 12 nm planar resolution detail in **(g)**. The imaging has few disruptive artifacts and high whole-field consistency, but lower contrast and fine structure resolvability compared to ssTEM. **(h)** Cartoon of ssTEM imaging of the CNS. A microtome cuts ultrathin sections from the block-face of the embedded sample in series. Detectors in a transmission electron microscope image an electron beam projected through each section. An example montaged section image is shown in **(i)**, with full 3.8 nm planar resolution detail in **(j)**. Fine structure and synapses (yellow arrow) are resolvable.

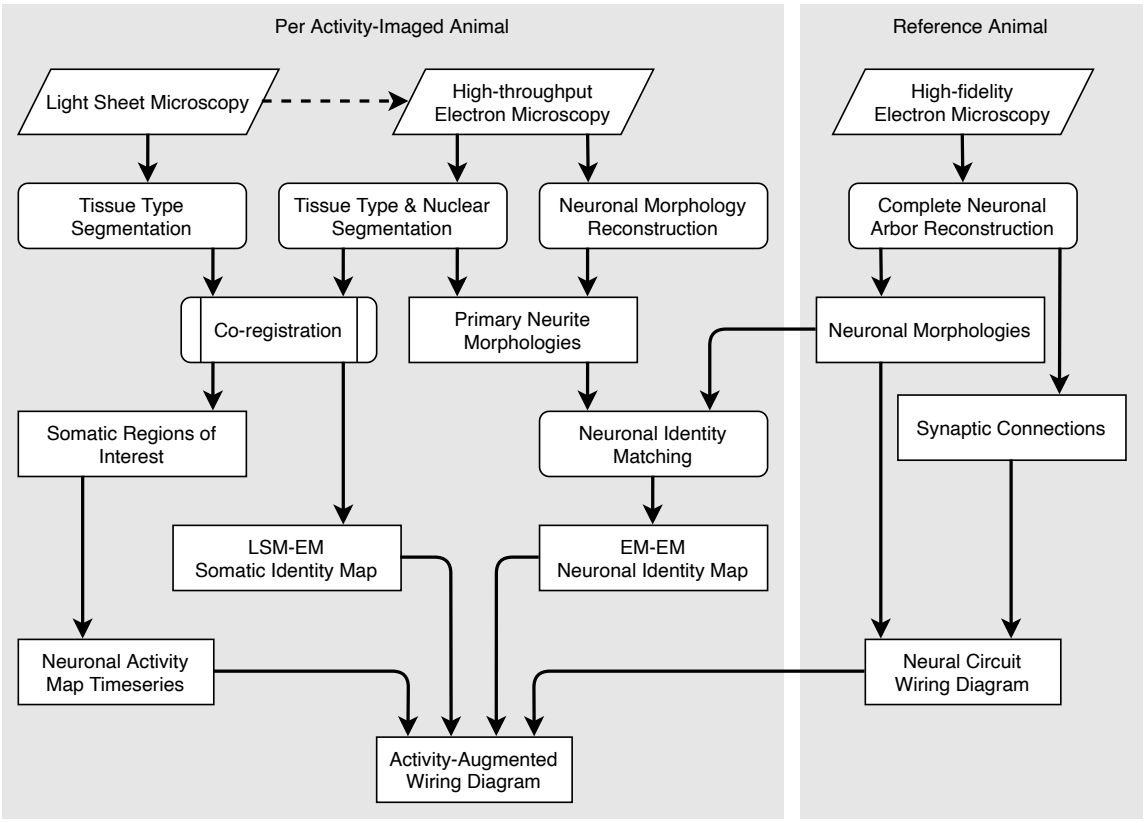

Fig. 1.2 Data Flow Diagram of Wiring Diagram Augmentation. Rhomboid nodes are data inputs, rounded nodes are data processing steps, and rectangular nodes are data artifacts. The left shaded area indicates the data flow process contributed by this thesis performed for each animal used for wiring diagram augmentation, while the right shaded area indicates the existing wiring diagram mapping process.

Chapter 2

Background

2.1 Neural Circuits Underlying Motor Control in Larval *Drosophila*

The body of the *Drosophila* larva is segmented into three thoracic segments (T1-T3) at the anterior and nine abdominal segments (A1-A9) at the posterior. This segmentation is reflected in the structure of the ventral nerve cord (VNC), being similarly composed of neuromere segments each attached by two peripheral nerves, one per side, to the corresponding body segment [29]. Abdominal neuromeres also send a dorsomedially rooted transverse nerve to the corresponding segment's body wall. Peripheral and transverse nerves convey both sensory input and motor neuron outputs. Each segment of the VNC is composed of two bilaterally symmetric hemisegments, each containing a repeating complement of homologous neuronal lineages. These lineages tile the superficial cell body rind surrounding the VNC neuropil and project their primary neurites into the central neuropil via a bundled tract shared with their lineage. The neuropil is spatially organized into motor and sensory domains along the axial plane [30, 31]. Via these developmental mechanisms of segmentally repeating spatial organization and stereotyped homologous neuronal fates, the VNC is principally composed of overlapping, segmentally repeating circuits. However segmental circuitry is not identical; different lineages and gene expressions take effect across segments, most notably between thoracic and abdominal segments, in segment A1, and in the joined tail segment A8/9 [32].

31 motor neurons in each VNC abdominal hemisegment innervate a repeating set of approximately 30 somatic muscles in the body wall of the corresponding body hemisegment [33, 12]. Body wall musculature is organized into groups actuating independent longitudinal contraction of the segment ventrally and dorsally, transverse contraction laterally, and oblique and acute muscle groups between these [34]. The spatial arrangement of these muscle groups

is myotopically mapped to the motor domain of the VNC neuropil by stereotyped dendritic arborization of the motor neurons innervating them [35, 36]. Larvae's locomotive behavioral repertoire involving segmental somatic musculature includes forward and backward crawling, rolling, head casting, hunching, bending, and burrowing. Locomotive behaviors participate in the larva's repertoire of complex behaviors including foraging [37], feeding, wandering [37], predation escape (nocifense) [38], and conspecific grouping (sometimes described as social behavior) [39, 40].

2.1.1 Behavior Selection

Motor control requires coordinated selection and initiation of behaviors over time at the scope of the entire organism. In *Drosophila* larvae, motor circuits in the VNC receive input from descending axons from neurons in the brain in addition to sensory input from nerves [41]. The brain is connected at the anterior, dorsal end of the VNC, joined by the subesophageal zone (SEZ), with the esophagus passing between the VNC and the brain's symmetric hemispheres via the foramen. Brain circuitry has been shown to perform sensory processing [42], sensory integration [43, 44], and learning [45] for effective behavior selection. However, larvae will autonomously and spontaneously perform many locomotive behaviors in the absence of brain input [46]. This implies motor coordination circuitry sufficient for selection and initiation must be distributed, decentralized, or hierarchical, with the VNC being independently capable of some degree of selection and coordination between behaviors, rather than descending control exclusively and exhaustively recruiting and inhibiting the appropriate circuit modules based on descending behavioral selection.

VNC-local selection, initiation, and maintenance of behavior has been extensively studied in the escape response of larvae to abdominal mechano-nociceptive stimuli. When stimulated with a probe along the lateral surface of the abdomen, larvae will often interrupt their current behavioral state to engage in one of fast crawling, backward crawling, rolling, hunching, or bending. This response may be an evolved defense to attempt escape from parasitic wasps or predators [38], or to prolong the encounter to reduce the opportunity to attack other larvae. The response is mediated by a hemisegmental population of Basin neurons [4] and down-and-back neurons (DnBs) [47], which locally integrate mechanosensory and nociceptive information. Direct optogenetic or thermogenetic activation of Basin neurons is sufficient to initiate response behaviors locally. Further, selection of the response behavior and maintenance of that behavioral state is mediated by a local circuit involving the Basins, rather than a centralized brain mechanism [27].

This model of Basin-mediated behavioral selection contributes a concrete circuit motif for selection in reciprocal feedforward inhibition and for maintenance in locally recurrent mutual

inhibition, while providing a mechanism for extrinsic modulation of selection by descending control. Similar motifs may recur in other pathways coordinating pairs of responses to particular stimuli. However, accounting only for selection between bending and hunching, and being a parallel pathway to DnB, the limitations described in Section 1.1 also apply here: how local sub-circuits interact to coordinate between not only pairs of behaviors but across behavioral repertoires and how this is coordinated organism-wide remain unknown.

2.1.2 Peristalsis and Antagonistic Behaviors

Both forward and backward crawling activate overlapping but non-identical groups of body wall muscles sequentially in each segment in phase with the peristaltic wave; both waves predominantly recruit first longitudinal muscles to contract the segment, then transverse muscles to increase the rigidity of the segment after longitudinal muscles have relaxed and the contraction has moved to the next segment [12, 14]. Both directions recruit at least 25 of the 31 hemisegmental motor neurons [14]. This implies broad coordination of the 118 premotor neurons is necessary.

As mentioned in Section 1.1, the phase of these sequential contractions is differently coordinated for each crawling direction. In forward peristalsis lateral contraction of the segment occurs earlier in the sequence to be concurrent with the ventral and dorsal longitudinal contraction of the next anterior segment, while in backward peristalsis lateral contraction occurs later and ventral longitudinal contraction earlier such that they are simulatenous between a segment and its posterior neighbor, respectively [12]. This phase offset is modulated by premotor neurons A01d3 in forward peristalsis and A27k in backward peristalsis, which excite an overlapping set of premotor targets in the next posterior or next anterior segment, respectively [13].

Motifs for modulation of analogous aspects of wave propagation are not necessarily as symmetric as for the phase offset circuit. Circuit mechanisms timing the initiating edge of wave propagation have been described via repeating intersegmental, local circuits for forward peristalsis, and via a shared descending neuron for backward peristalsis. In forward peristalsis premotor neuron A27h, which excites motor neurons for longitudinal contraction, projects into the next anterior segment and excites an interneuron that inhibits the A27h in that segment, which prevents the peristaltic wave from propagating until the appropriate phase sequence [9]. In backward peristalsis, putative backward crawling command moonwalker descending neurons (MDNs) initiate the peristaltic wave via excitatory premotor neuron A18b, while preventing forward propagation of the wave by inhibiting A27h via descending neurons Pair1 [11]. The dynamics of this circuit are not fully known as MDN also excites premotor neurons A27l via ThDN, and neither of these have genetic driver lines with specific

expression [11]. While a specific driver line exists for A27k [13], which is also excited by ThDN, single cell targeting driver lines do not allow for observing co-activity and relative timing between multiple neurons. Therefore activity-augmented wiring diagrams could yield more comprehensive understanding of backward wave initiation, propagation, and inhibition of antagonistic behaviors.

2.2 Mapping Structural Wiring Diagrams of Neural Circuits

Neural circuit wiring diagrams are graph representations of a nervous system that encode neuronal elements as nodes and their interactions – most typically chemical synapses, but possibly gap junctions, ephaptic coupling, neuropeptide exchange, or other information signals or ultrastructural markers – as edges. The predominant method of mapping circuit wiring diagrams is by structural imaging of neuronal morphology, although methods besides imaging such as combinatorial genetic sequencing are possible [48]. For the typical case of mapping wiring at the resolution of individual synaptic connections and neurons or neuronal compartments – micro-scale connectomics – either electron microscopy of fixed neural tissue prepared with electron-dense membrane and synaptic stains, or light microscopy of fluorescent protein markers is employed. Most light level methods can not densely express markers while preserving the resolvability of individual structures, so are often used for targeted mapping, generating unions of multiple sparse maps [49], with random labelings of multiple fluorescent channels [50], or combinations of these. Electron microscopy is inherently suited for dense mapping of wiring diagrams as it captures contrasting agents that have been stained into the sample with high resolution and relative uniformity of signal to noise throughout the volume [51].

Whole-system mapping of neural circuit wiring diagrams via electron microscopy began with *Caenorhabditis elegans* [52] and has become an increasingly common method for neural circuit study over the past 15 years, with whole nervous system or brain volumes having been acquired for multiple *Caenorhabditis elegans* [53, 54], *Ciona intestinalis* [55], the annelid *Platynereis dumerilii* [56], *Drosophila* larva, adult *Drosophila* [57, 58, 59], and zebrafish [60]; incomplete but large regions have been acquired for zebra finch [61] and mice [62]. Electron microscopy connectomics' recent popularity is primarily due to two areas of technological development: improved microscopy techniques for reliable and rapid acquisition of large samples, and computational techniques for accurately reconstructing neuronal ultrastructure from those volumes, most notably from machine learning based com-

puter vision. In microscopy, the key developments are methods for mechanized, repeatable, and eventually automated imaging of volumes in 2D sequences [63]. This branched into approaches using serial sectioning techniques, eventually with tape or grid section handling [64, 57, 65], many compatible with transmission electron microscopy, and approaches using serial scanning electron microscopy and tissue removal of the face of the block containing the remainder of the sample [66, 67, 26, 68, 69, 70].

In computer vision, the key developments have been driven by continuous improvement of image and label data, machine learning algorithms, and computational hardware. For data, improvement of the volume, image quality, registration quality, and ground-truth labeling size of electron microscopy [71] have both simplified the task of automated or semi-automated detection and segmentation of relevant morphological structures and refined the quality of labels for supervised learning. Algorithms for segmentation of neuronal morphology began with voxel-wise prediction of membranes with random forests or convolutional neural networks (CNNs) [72], regression-based agglomeration of watershed supervoxels from membrane predictions [73], or energy-minimizing propagation of membrane profile contours across serial sections [74]. They have progressed mainly through contemporary improvements in CNNs, representations of regions of intracellular affinity rather than boundary detection [75] and related improvements in loss metrics [76] more robust to false merges, more sophisticated agglomeration algorithms [77, 78, 79], and novel approaches with per-compartment recurrent CNNs [80]. Finally, increased computational capacity, especially due to improvements in graphics processing unit (GPU) hardware determining the performance of CNNs, has allowed for application of more complex algorithms using larger image context to larger microscopy volumes.

Background on software tools for mapping neural circuits is discussed in Chapter 3.

2.3 Activity Mapping of Neural Circuits

Proxies for membrane potential activity of large neuronal populations can be imaged using fluorescent indicators of either ions binding proteins [81, 82] or voltage [83]. While confocal or laser scanning microscopy is sufficient for imaging sparse neuron populations over large planar or multi-planar fields of view in tissues such as mouse cortex [84], imaging whole larval CNS samples or organisms at timescales comparable to fluorescent calcium ion indicator dynamics while retaining the ability to distinguish signal from individual cell bodies or processes often requires advanced volumetric microscopy. Light sheet microscopy (LSM) (also referred to as selective plane illumination microscopy (SPIM) [85]) is a super-resolution-capable imaging method that rapidly sweeps a thin laser "sheet" of illumination

over a sample, exciting fluorophores whose emitted light is detected by objectives oriented orthogonally to the sheet [86]. Two opposing objectives can image a single sheet or opposing set of co-planar sheets for multi-view LSM [87]. Two orthogonal arrangements of multi-view emitters and objectives can be temporally interleaved to image in a pseudo-isotropic arrangement referred to as iso-view LSM [24]. LSM has been used to acquire whole-CNS volumetric timeseries of neuronal activity for larval zebrafish [88] and larval *Drosophila* [21]. Illumination on a second channel can be used for optogenetic activation, either over broadly or over targeted regions of interest, and in either an open-loop or closed-loop control [89].

2.4 Combined Function and Structural Observation of Neural Circuits

This section surveys existing and alternative methods for either combining functional and structural imaging or enhancing imaging techniques for augmenting wiring diagrams.

2.4.1 Augmentations to Electron Microscopy

Besides neuronal morphology and synaptic structures, electron microscopy can detect other spatially-structured features of cell and biomolecular state. To aid this detection, methods have been developed to augment electron microscopy with markers in addition to basic membrane and synaptic staining. Markers can be genetically encoded, to tag specific structures or proteins with electron-dense molecules [90, 91]. Alternatively, subsets of sections in a ssTEM volume can be labeled with antibodies to mark proteins of interest with electron-dense gold, effectively augmenting the electron microscopy with an independent channel of information so long as the labeled target is sparsely expressed [92]. Both approaches can be enhanced by depositing multiple markers with known, distinct spectra that can be energy filtered in transmission electron microscopy, allowing for the independent identification of multiple types of target structures in a single volume [93].

While potentially effective for augmenting wiring diagrams with information like neurotransmitters, these methods are not applicable to ion activity dynamics, other than perhaps integrals over single time intervals via convertible markers akin to those used in fluorescent imaging [94]. In comparison, the multi-modal methods presented in this thesis for similar identification of biomarkers have the advantages of relying on fluorescent labeling and imaging techniques that are already in the domain of many *Drosophila* labs' expertise and do not require time-intensive and error-prone section handling. Direct augmentations of electron microscopy have the advantage of relying on a single, high-resolution imaging modality,

obviating difficulties from ambiguous localization and identification of cellular signals in LSM and registration between microscopy modalities.

A potential shared by direct electron microscopy augmentation techniques and those presented in this thesis is that either may allow discovery of latent but detectable features in unaugmented electron microscopy. Besides membranes, synaptic sites, and similar structures, existing electron microscopy volumes contain extensive imaging of ultrastructure that is not annotated or not analyzed in most wiring diagram mapping. These image features may be difficult to detect or beyond reliable human interpretation (super-perceptual), but statistically learnable from the data. For example, machine learning computer vision can classify some synaptic neurotransmitters in adult *Drosophila* based on supervised learning from synapse-local image data of neurons with known transmitters [95]. Augmentations to electron microscopy directly or via this thesis' methods could provide rapid, large-scale ground truth for development of similar techniques to more fully exploit latent ultrastructural features in existing and future electron microscopy volumes.

2.4.2 Light-Level Approaches

While the barrier to electron microscopy's use for activity imaging is the necessity of fixing and sectioning or otherwise destroying the tissue, thus limiting observation to a brief instant in time, for light-level microscopy the barrier to structural imaging is spatial: resolution, signal deep in tissues, and the resolvability of separate, neighboring structures. These limitations can be addressed by either making the structural signal more sparse across channels [50] or improving the effective imaging resolution. LSM achieves resolution of approximately 1x1x2.5µm in whole larval CNS [21]. If higher absolute spatial resolution is not optically possible, tissue expansion [96] can achieve higher effective resolution for connectomics on the order of 100 nm [97] or at lower resolution for much larger samples [98].

A common difficulty for light-level methods is the ability to resolve synapses. Synapses can be inferred at process appositions, but for many neural circuits it is known synapse distribution deviates from apposition surface area. Separate synaptic labels can be expressed, but can complicate and interfere with other measures to improve process resolvability. For the augmentation strategy proposed by this thesis, however, direct observation of synapses is not needed, only primary neurite morphology. Future variations of this approach could substitute light-level structural imaging for high-throughput electron microscopy to observe neuron morphology and associate it with cell body signals.

2.4.3 Multi-modal Imaging Approaches

Recent work has acquired whole-sample GCaMP activity imaging prior to electron microscopy for large volumes, enabling direct correlation of function and structure [60, 99, 62]. This demonstrates how functional information aids mechanistic interpretation of mapped circuit wiring diagrams. While direct joint observations of function and structure in the same sample are necessary in mammalian cortex and similar neural systems without stereotyped, identifiable neurons, the relative advantage of this thesis' proposed approach is the ability to augment wiring diagrams with functional observation of multiple animals and incrementally with new experimental interventions and aims.

Though not applied to neural tissue, recent work has also combined super-resolution light microscopy of fluorescent markers with large-volume FIBSEM [100]. Cell tissue applications demand similar methods development for registration, ultrastructural segmentation, and multi-modal analyses [101].

Methods similar to those for augmenting electron microscopy can alternatively use a separate modality, such as fluorescent imaging, to detect genetically-expressed or immunostained markers, while also detecting the marker in electron microscopy for correlative interpretation [102, 103, 104]. These methods are most useful when the entire system of interest can not be imaged with electron microscopy due its size, therefore light-level imaging can observe sparse large-scale structure or identify common neurons across distinct electron microscopy regions of interest.

Recent work has applied synchrotron tomography to structural questions in connectomics [105, 106, 107, 108]. Synchrotron tomography offers dense, low-artifact structural imaging of tissue contrast similar to electron microscopy, but non-destructively and with high throughput. While resolution is not the same order as electron microscopy, on the order of 100 nm, targeted contrast can follow morphology of individual neurons and tracts across volumes many times those possible with electron microscopy. This novel niche in the envelope of imaging quality, resolution, and speed may allow for new multi-modal approaches building on the function-structure augmentation of this work.

Chapter 3

High Throughput Structural Neuroanatomy of Larval *Drosophila*

The purpose of electron microscopy in this project is to identify neurons on the basis of their stereotyped arbor morphology in *Drosophila*. This structurally established identity transitively identifies the cell-body-localized activity signal in the co-registered light sheet microscopy (LSM) of the same sample and allows cross-referencing the neuron with its correlates in synaptic wiring diagrams mapped from other electron microscopy volumes. Neuroanatomical information that must be extracted from each LSM-imaged volume for the overall activity augmentation workflow (Figure 1.2) includes:

- Detection of nuclei for localizing cell bodies of all neurons of interest, for association with somatic activity signals in LSM.
- Tissue structure labeling for co-registration with LSM.
- Reconstruction of primary neurite morphologies for all neurons of interest, for morphological identification.
- Registration with the reference electron microscopy volume, for morphological neuron identification.

Imaging multiple animals to observe many behavioral repetitions and transitions is rate limited by electron microscopy and subsequent neuroanatomical analysis, as those require timescales of weeks in contrast to hours for LSM. Therefore improvement over existing electron microscopy image analysis methods is required to adapt for two limitations of the data: the requirement for high throughput imaging, and degradation of the sample and interference with preparation processes caused by prior LSM.

3.1 Background

Image analysis of electron microscopy volumes begins with registration, a process assembling individual image tiles sequentially acquired from the microscope into a three-dimensional volume that optimizes the alignment of tissue structures between tiles. Registration can be performed as a transform optimization problem of point- or patch-wise matching via many models of image transforms and interest point similarity [109, 110], or as a deformed image or deformation field inference problem [111, 112]. In the case of FIBSEM, the acquired image is of the whole block face surface, removing the need for aligning a mosaic of tiles for each sample section, and the low inter-section distortion of the sample due to ion milling rather than mechanical sectioning greatly simplifies registration.

Neuronal morphology can be reconstructed from electron microscopy volumes either by manual annotation of neurite's centerline geometry (skeletonization) or volume, or by semi-automated assembly of the same representations from computer vision. Many tools exist for both manual [113, 114] and semi-automated [115] reconstruction, but in *Drosophila* larva the largest community is built around manual reconstruction using the Collaborative Annotation Toolkit for Massive Amounts of Image Data (CATMAID) [116, 117]. CATMAID facilitates distributed reconstruction by allowing neuroanatomists to work collaboratively on a shared reconstruction via a web browser. Crucial to this thesis' methods, CATMAID also integrates analysis tools and cross-instance federation, which enable morphological matching and guiding new reconstructions in one sample by existing reconstructions in another. Neurons can be identified based on their stereotyped morphology using the morphological similarity metric NBLAST [118].

3.2 Methods

Figure 3.1 outlines how information necessary for augmenting wiring diagrams is extracted from each microscopy volume. Each process of these methods is described below.

3.2.1 Datasets

Imaged fluorescent calcium ion indicator expressing larvae for activity imaging are listed in Table 3.1 and neurotransmitter label expressing larvae are listed in Table 3.2, with their constructs in Table 3.3. Sample serial identifiers reflect approximate order of acquisition. Volume sizes listed are for the bounding box volume of the imaged embedding block, not the tissue-occupied region. In total 6 activity and 3 neurotransmitter larvae were acquired and used for all subsequent methods.

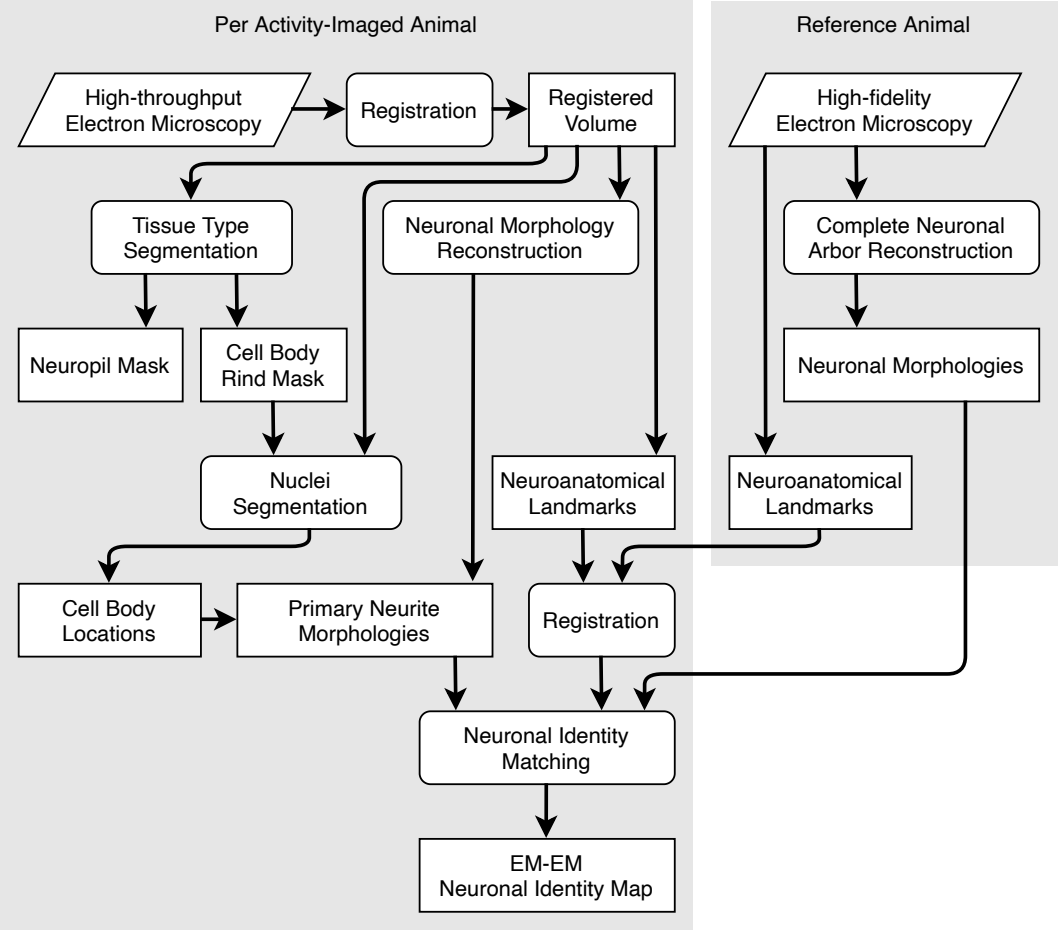

Fig. 3.1 Data Flow Diagram of Electron Microscopy Processing. This diagram details the contributed methods for processing high-throughput electron microscopy to establish transitive identity between cell body locations and neurons mapped in a reference animal. See Figure 1.2 for an abstracted overview.

Sample	**Instar**	**Acquisition** (days)	**Resolution** (nm)	**Volume** (TVox)
1019	1	12	16	1.28
1018	1	24	12	2.14
1038	3	30	12	4.75
1085	3	38	12	7.19
1097	1	26	12	3.06
1099	1	21	12	2.03

Table 3.1 List of FIBSEM Imaged Activity Indicator Larvae

Sample	Instar	Neurotransmitter	Acquisition (days)	Resolution (nm)	Volume (TVox)
1123	1	Acetylcholine	9	12	3.23
1126	1	Glutamate	8	12	3.03
1128	1	GABA	9	12	2.79

Table 3.2 List of FIBSEM Imaged Neurotransmitter Larvae

Sample	Construct
1019 1018	$\frac{\textit{LexAop-Chrimson (attP18)}}{+/Y}$; $\frac{\textit{72F11-LexA (JK22)}}{\textit{HisAv-RFP}}$; $\frac{\textit{57C10-GAL4 (attP2)}}{\textit{UAS-GCaMP6s (VK0005)}}$
1038 1085 1097 1099	$\frac{\textit{LexAop-Chronos (attP18)}}{+/Y}$; $\frac{\textit{72F11-LexA (JK22)}}{+}$; $\frac{\textit{UAS-RGECO1a (VK0005)}}{\textit{57C10-GAL4 (attP2)}}$
1123	w; $\frac{\textit{UAS-nls.GFP (attP40)}}{+}$; $\frac{\textit{LexAop-nls.tdTomato (VK00040), 57C10-LexA (attP2)}}{\textit{ChAT-GAL4 [MI04508]}}$
1126	w; $\frac{\textit{UAS-nls.GFP (attP40)}}{\textit{VGlut-GAL4 [MI04979]}}$; $\frac{\textit{LexAop-nls.tdTomato (VK00040), 57C10-LexA (attP2)}}{+}$
1128	$\frac{w}{wy/Y}$; $\frac{\textit{UAS-nls.GFP (attP40), tub-DBD}}{+}$; $\frac{\textit{LexAop-nls.tdTomato (VK00040), 57C10-LexA (attP2)}}{\textit{Gad1-AD[MI09277]}}$

Table 3.3 Genetic Driver and Effector Line Constructs of Imaged Larvae

Following LSM (Chapter 4), each larval CNS is removed from the embedding agarose and prepared for FIBSEM according to the protocol in Table 3.4. All larva handling, dissection, fixation, constrasting, and embedding was performed by Nadine Randel, along with creation of genetic crosses for activity indicator larvae. Genetic crosses for neurotransmitter larvae were created by Michael Winding.

	Activity indicator samples	**Neurotransmitter samples**
Fixation	4% Glutaraldehyde / 0.1 M Sodium-cacodylate buffer (pH 7.4) for 1 h	Glutaraldehyde / 2.5 Formaldehyde / 0.1 M Sodium-cacodylate buffer (pH 7.3) for 1 h
Post-Fixation (I) – step 1	1% OsO_4/1.25% Potassium hexacyanoferrate (II) trihydrate, in 0.1 M Na-cacodylate buffer for 0.5 h	0.5% OsO_4 in 0.1 M Sodium-cacodylate for 40 min; 0.8% $K_4Fe(CN)_6$ in 0.1 M NaCacodylate buffer for 2 h
Post-Fixation (I) – step 2	1% Thiocarbohydrazide for 10 min	1% Thiocarbohydrazide for 10 min
Post-Fixation (II)	1% OsO_4 in 0.1% Sodium-cacodylate buffer for 30 min	2%OsO_4 in ddH_2O for 30 min
Contrast (I)	1% Uranyl acetate in water over night	0.5% UA in ddH_2O for 20 min
Contrast (II)	Walton lead[119] @ 64 °C for 1 h	Walton lead[119] @ 64 °C for 0.5 h + 2 h room temperature
Contrast (III)	0.8% OsO_4 in ddH_2O	-
Dehydration	Acetone	PLT-LTS[120]
Embedding	Durcopan	Durcopan

Table 3.4 Fixation, Constrasting, and Embedding for FIBSEM

3.2.2 Imaging and Alignment of Electron Microscopy Volumes

All FIBSEM imaging was acquired by Shan Xu and Song Pang through a collaboration with the laboratory of Herald Hess at Janelia Research Campus. For all calcium ion indicator datasets, imaging was performed at a beam rate of 2.5 MHz with a Zeiss Nvision 40 FIBSEM capable of acquiring entire larval CNSs with minimal restarts or other artifact-inducing process limitations [26]. Neurotransmitter datasets were imaged at a beam rate of 10 MHz with a Zeiss Merlin FIBSEM capable of faster acquisition due to a much higher primary electron current.

All datasets other than samples 1018 and 1019 were registered using a cluster-distributed pipeline I developed in collaboration with Albert Cardona. Point matches between pairs of tiles with adjacency up to 5 sections away in the sequence are extracted using grid-sampled image blocks in a local neighborhood [121]. If point matching fails, scale-invariant feature transform (SIFT) feature matches [122] across the entirety of the further downsampled tile pair are extracted. A second attempt of point match extraction is made after applying a rigid alignment to the tile pair from the SIFT matches; if this also fails the SIFT matches are used for the final alignment. Due to the low distortion of the imaged tiles, a translation transform model is used for alignment [109].

Samples 1018 and 1019 were registered with TrakEM2 [113]. Sample 1018 was aligned with a rigid-regularized affine model, except for regions surrounding two large FIBSEM waves in the brain (see Figure 3.7a(ii)), which were elastically aligned [110]. FIBSEM waves and other variations in milling depth can be more comprehensively detected, estimated, and corrected [123], but as few were encountered this optimization has not been applied. A 10^3 μm^3 cutout of sample 1019 was elastically aligned, as described below.

Registered volumes are normalized with contrast limited adaptive histogram equalization, exported as N5 datasets [124], and downsampled into scale pyramids [125].

3.2.3 Cross-Environment Software for Volumetric Image Data

The size of FIBSEM image data acquired for this project presents challenges for existing larval connectomics analysis workflows and tools such as those in [117]. While due to the lower mean spatial resolution most individual FIBSEM samples are smaller image data than the existing ssTEM first instar larva (4.3 TVox), the requirement for multiple samples to observe sufficient behavioral bouts requires much larger data in total. It also requires tools and a data processing pipeline that can be reproducibly applied to each sample with minimal marginal effort. Further, while isotropic data has been used in many other connectomics tools ecosystems [114, 126], and I had previously extended CATMAID and other larval tools for rudimentary isotropic data support, the majority of tools were designed around anisotropic data presuming tiled stacks of 2D images. Due to the reduced contrast of FIBSEM relative to ssTEM, rapidly navigating image data to exploit optic flow and viewing locations from multiple orientations is critical to resolving ambiguous ultrastructure.

To accommodate isotropic access to the acquired FIBSEM samples, the N5 N-dimensional tensor storage format [124] is used for storage of all registered image volumes and subsequent volumetric annotations and segmentation. The original Java implementation is sufficient for many image processing tasks, but integration with the existing larval connectomics workflow requires availability to additional environments: a systems-level language for cross-platform

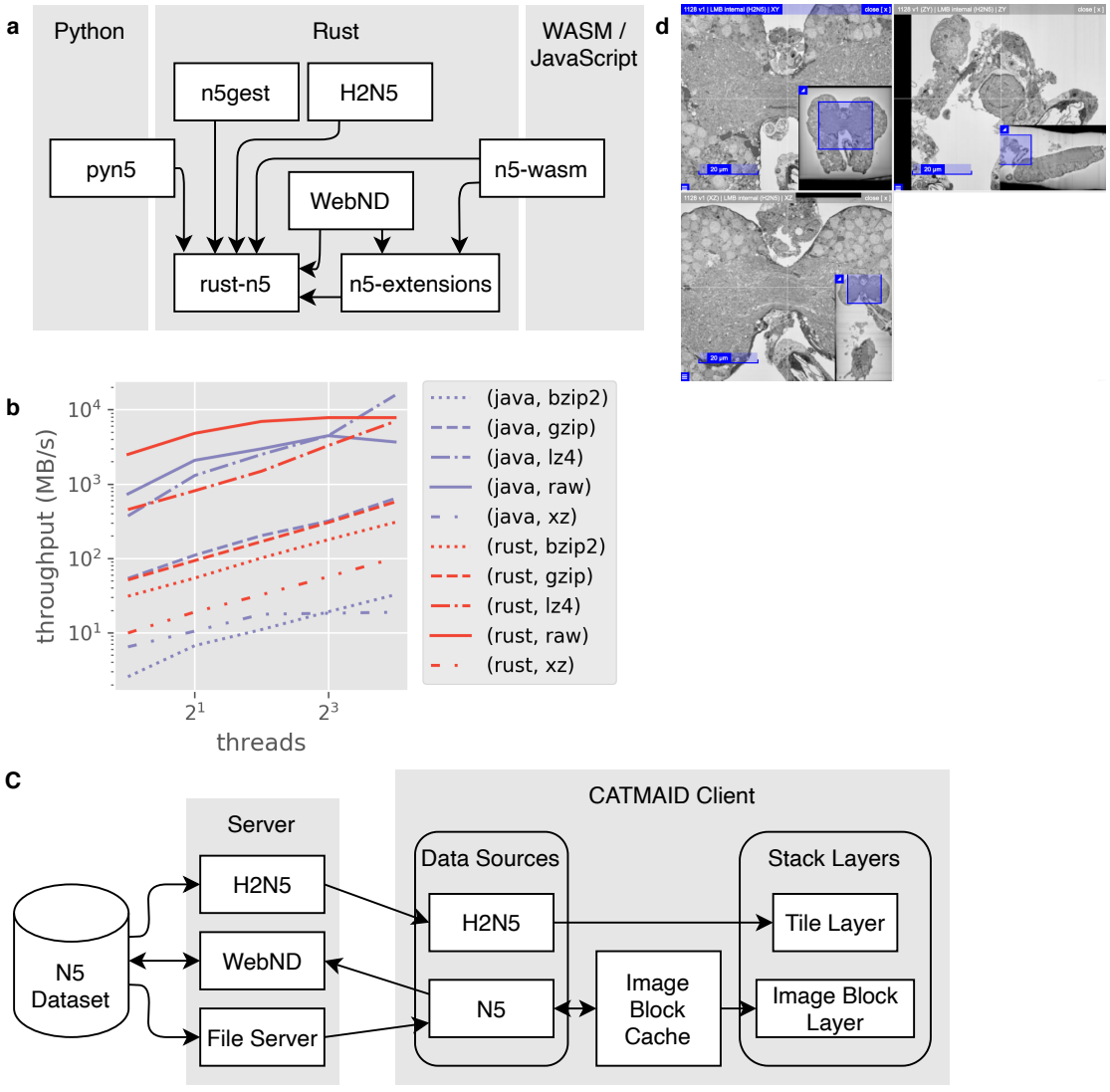

Fig. 3.2 Software for Processing and Visualization of Volumetric Image Data. **(a)** Dependency diagram of libraries created for cross-environment volumetric data processing. **(b)** Performance comparison of the contributed Rust N5 implementation with the reference Java implementation for varying compression schemes. **(c)** Diagram of N5 access from CATMAID. Arrows indicate image data flow direction. **(d)** Example of orthogonal views into an N5 dataset of one of the acquired FIBSEM larvae from within CATMAID.

data shepherding and high-throughput bulk processing, Python for compatibility with many image analysis and machine learning tools, and the browser for access from the distributed, collaborative reconstruction environment of CATMAID. To this end I created a suite of libraries and tools based around a re-implementation of the N5 interface and format in the Rust programming language. Rust provides a performance envelope similar to C/C++ while also guaranteeing memory safety and enabling trivial binding to Python and use in web browsers via web assembly. While interfaces exist for accessing N5 from Python [127, 128] and JavaScript [129, 130], this new suite provides a bridge for volumetric data between the extensive Java image processing ecosystem, CATMAID and future web assembly-based browser applications, and the young Rust image processing and high-performance computing communities. The constituent softwares' dependency structure is shown in Figure 3.2a and listed below:

rust-n5 [131] A high performance, memory- and concurrency-safe re-implementation of the N5 N-dimensional tensor interface and filesystem format in the Rust programming language. Throughput matches or exceeds the reference implementation in most execution contexts, as shown in Figure 3.2b.

pyn5 [132] Python bindings and NumPy-compatible interfaces for rust-n5 that allow ergonomic, pip-installable access to N5 datasets. While having fewer features than similar library z5py [128], this Python package avoids the need for Conda environments and provides the guarantee of a consistent backend with the browser libraries below. This library was written in collaboration with William Patton and Christopher Barnes.

n5gest [133] Command line utilities for parallel execution of common data shepherding tasks such as import and export to image formats, filesystem usage and metadata statistics, verification of file integrity, and empty data deletion.

H2N5 [134] An HTTP service that serves N5 datasets as tiled 2D slices of common image formats such as JPEG and PNG. This allows a wide variety of existing tools including CATMAID to access N5 data without the need for new development. H2N5's features include minimal allocations and least-recently used caching for data blocks and image tiles to achieve latency for warm data access at the same millisecond order as pre-rendered tiles.

n5-wasm [135] Web assembly (WASM) bindings for rust-n5 and JavaScript wrappers for a HTTP browser request based backend. Web assembly is a binary instruction format to which many languages including Rust can be compiled and is executable by most

current web browsers. This provides web applications access to N5 datasets directly served over HTTP.

n5-extensions Extension traits for N5 including access to scale pyramids via conventional dataset group naming and content hash metadata for state checking for capable backends. This library has been used for minor work in this thesis but is not yet publicly available. Christopher Barnes contributed to this library.

WebND HTTP service exposing mutating interfaces for N5 datasets. The service optionally performs state checking to prevent data inconsistency and provides atomic operations across multiple data blocks. This library has been used for minor work in this thesis but is not yet publicly available.

In addition to these libraries, a library abstracting interfaces for N-dimensional, chunk-based tensor storage with both N5 and Zarr [136] backends has been created, but is unpublished pending the finalization of the Zarr version 3 specification. This will allow all dependent tools such as n5gest and n5-wasm to access Zarr format datasets as well.

Figure 3.2c shows how CATMAID accesses N5 data via these libraries. Two pathways serve different access patterns and networking contexts: as tiled 2D images via H2N5, and as N-dimensional chunks via n5-wasm. Access as tiled images via H2N5 reduces per-field-of-view bandwidth and latency, but requires separate transfers for orthogonal views onto the data and does not make use of data locality or prefetching. This is most appropriate for migrating legacy data to volumetric storage for consistency, while preserving a tiled access for bandwidth constrained scenarios such as remote work, for sparse browsing when data locality and orthogonal views are not critical for workflow efficiency, and for resource-limited devices. In contrast, volumetric access via n5-wasm is implemented via a new set of image data sources and stack visualization layers in CATMAID that allow for multiple views or dimensional slicing into the same N5 dataset to share retrieved data blocks. This includes a caching layer (in addition to existing GPU caching for sliced views) with capabilities for write-back or write-through mutation to WebND or other services. Preemptable prefetching of data blocks neighboring the view orthogonally, in the periphery, or at neighboring scale levels is also supported. Data fetching is performed in parallel via browser web workers. Volumetric access is suitable for high-bandwidth contexts such as when working with a locally networked image mirror, and when focused, sustained visualization of local data regions is critical, such as during reconstruction of fine-scale or ambiguous structures.

I developed many related extensions to CATMAID to accommodate these uses, including support for multiple mirrors for image data sources (written with Tom Kazimiers) to enable seamless switching between H2N5 and direct N5 mirrors based on context, interfaces for

effortlessly importing N5 datasets, support for arbitrary anisotropy in data including between viewing plane dimensions, support for arbitrary downsampling factors in image pyramids (building on my work enabling multiple-resolution tracing [60]), support for 16-bit per channel image data and rendering, support for 64-bit label data, and rendering optimizations to allow for browsing and visualizing image data at 60 Hz or greater.

BigDataViewer [137] and 3Dscript [138] were additionally used for visualization and analysis.

3.2.4 Segmentation of Tissue and Cellular Structures

To determine regions of interest for later processing and detect the surface of the CNS for later registration with LSM, a tissue type classifier segments each volume into three regions: non-tissue, cell body rind and other non-neuropil tissue, and neuropil. This classifier is based on a convolutional neural network (CNN) using the U-Net architecture [139]. The classifier is 2D so that it could be applied prior to registration if needed (such as for masking point matches to tissue regions) and operates at 48 nm resolution. The network was implemented in TensorFlow [140] and trained with Gunpowder [141].

Following tissue type classification, nuclei are detected in the predicted cell body rind region using a similar classifier that predicts a binary nuclear label. The classifier CNN uses a 3D U-Net architecture [142] to incorporate volumetric information and improve the spatial consistency of prediction. Implementation and training are similar to the tissue type classifier. Binary prediction of nuclei is sufficient in most cases as nuclei are well-separated at 48 nm. Subsequent morphological erosion can easily separate false merges as the goal is only to detect nuclei centroids as points and not to generate precise segmentation. Both segmentations and post-processing are distributable across GPUs and clusters.

Ground truth training data was densely annotated in one first instar larva for three slabs of the volume along the anteroposterior axis: one near the front of the CNS to have labeled training data for the esophagus attached to many samples, one through the brain, and one in the VNC. Label annotations were made by Rebecca Arruda and myself in TrakEM2 [113].

For filtering spurious, non-neuronal, and non-glial nuclei detections, such as musculature in the esophagus, nuclei detections are classified with a simple support vector machine (SVM) using morphological features of the detected connected components. Labeling of detections for classification was performed in Napari [143].

3.2.5 Landmarks for Comparative *Drosophila* VNC Connectomics

To register between electron microscopy volumes, segmentally repeating neuroanatomical landmarks were annotated in each volume. These landmarks are based around the following large scale anatomies from [29] and are placed in each hemisegment:

- The dorsal and ventral neuropil entries of dorsoventral channel of the neurohemal organ separating the medial commissures in each segment neuropil. To be robust to variation in the contour of the neuropil profile and the morphology of glia surrounding the dorsoventral channel, the point location of the landmark is taken during annotation to be the visualized center of mass of a cone with its vertex near the intersection of the channel with the neuropil and its base on the tangent plane connecting the respective dorsal or ventral extents of each hemisegment's neuropil.

- The split point of the peripheral nerve into the segmental nerve and the intersegmental nerve.

- The entry of the segmental nerve root (SNR) into the neuropil. For robust placement this point location is where the center of the nerve bundle on its trajectory at entry would intersect the interpolated surface of the neuropil were the nerve not present. This criterion is necessary to disambiguate placement across variable entry orientations of nerves between segments and the biases of placement between isotropic FIBSEM and anisotropic ssTEM.

- The entry of the inter-segmental nerve root (ISNR) into the neuropil, at both the anterior (ISNR-a) and posterior (ISNR-p) branches where applicable. The same criterion for placement as SNR is used.

Shown in Figure 3.3, these landmarks were selected to optimize invariance to inter-segmental and inter-animal variability in tissue structure in collaboration between Michael Winding, who placed them in the ssTEM volume, and myself. For the FIBSEM larvae, landmarks were placed by Nadine Randel and myself.

Building on cross-instance landmark registration in CATMAID created by Tom Kazimiers, I allowed for constraining for proper transforms, preventing mirroring when registering between differently oriented larval volumes, and choice of fit transform model from the affine group [144]. Interfaces were created for rapidly mapping registrations for large sets of landmark groups between commonly annotated CATMAID instances, which is necessary for performing analysis across many whole-CNS volumes for comparative connectomics.

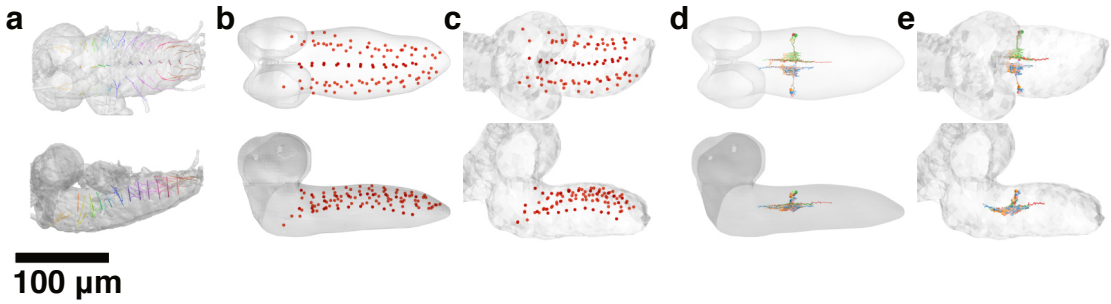

Fig. 3.3 Neuroanatomical Landmarks for Comparative Connectomics. **(a)** Neuroanatomical structures as described in subsection 3.2.5 reconstructed for illustration in a first instar CNS (sample 1128). For all eleven segments, neuropil-transiting dorsoventral tracts of the neurohemal organs along the midline and the peripheral nerves' tracts through the cell body rind, including SNR, ISNR-a, and ISNR-p are shown. **(b)** Point locations of the described landmarks placed in the reference ssTEM first instar larva and **(c)** in a FIBSEM first in larva (sample 1018). **(d)** Basin neurons (see subsection 2.1.1) reconstructed in the reference larva in segment A1. **(e)** Basin neurons from **(d)** transformed into FIBSEM via landmark registration.

3.2.6 Recursive Instance Segmentation of Neuronal Morphology

One limiting factor for combining functional and structural information using high-throughput electron microscopy is the rate at which neuronal morphology can be reconstructed to establish neuron identity. Automating or semi-automating morphological reconstruction by segmenting structural imaging with computer vision can increase reconstruction rate. A prepublished approach to neuronal segmentation based on recursive instance segmentation, flood-filling networks (FFNs), was potentially suited for the constraints of this project because its accuracy is comparable to or surpassing all published algorithms for isotropic electron microscopy [145]. Further, the object-focused rather than region-focused nature had potential for efficient application to sparse reconstruction targeting particular neurons. FFNs have since been published and applied to multiple petascale volumes from FIBSEM and ssTEM [80, 146, 59].

As no implementation was available (until December 2017), I replicated the algorithm in a new implementation and made it publicly available under an open license [147]. This implementation is based on the TensorFlow [140] and Keras [148] deep learning research libraries. In addition to the ResNet network architecture used in the original flood-filling algorithm [149], the implementation also supports the U-Net architecture [139, 142], which more efficiently learns multi-scale image feature representations and can process larger fields of view with fewer parameters. Data-parallel training and inference can be distributed over multiple graphics processing units (GPUs) with high utilization due to parallelized work

queues and data prefetching. Data augmentation of training data with axis permutation, mirroring, additive and multiplicative Gaussian noise, contrast rescaling (to simulate low-contrast sections), data masking (to simulate missing sections), and artifacts (to simulate precipitate, tears, and support film folds) are integrated, as is regularizing dropout. Training data is augmented with elastic deformation separately [79]. All volumetric data access and storage is backed by block-sparse data structures to allow processing of arbitrarily large out-of-memory volumes so long as the volume of the segmented structure and its local neighborhood are within system memory constraints The implementation also supports FFN algorithm variants such as alternative movement queue prioritizations and boundary distance prediction. Integrated visualization is provided by Neuroglancer [129].

Segmented volumes are skeletonized for import into CATMAID and analysis. Skeletonization is based on the TEASAR algorithm [150, 151]. To allow efficient in-memory and parallelized skeletonization, the adjacency graph of the block-sparse octree representation of the segmented volume is partitioned to minimize inter-subgraph adjacencies between partitions [152]. Each partition is skeletonized separately, and the resulting skeletonizations are stitched to yield a single skeleton representation.

All flood-filling networks presented here were trained on ssTEM of adult *Drosophila* neuropil from the CREMI challenge [71]. While ssTEM rather than FIBSEM, this dataset was chosen for implementation and evaluation of FFNs because the FIBSEM samples had not yet been imaged at the time of analysis, CREMI has the largest high quality ground truth annotation for any available *Drosophila* dataset, and was a representative sample for evaluating the applicability of FFNs to the reference ssTEM datasets. CREMI samples A and B were used exclusively for training. As the most difficult neuropil volume, the lesser z half of Sample C was used for training, while the greater z half was used for validation to stop network training and select final models.

To assess rates of morphological reconstruction, the implementation was made available as part of a semi-automated reconstruction tool that interfaces with CATMAID. The process diagram of this tool, including the FFN algorithm, are shown in Figure 3.4. This approach evolved into a tool written by William Patton for using seeded segmentation to proofread existing neuronal skeletons rather than produce de novo reconstructions [153].

The potential increase in the rate of morphological reconstruction can be modeled as a speedup versus fully manual tracing. Speedup depends on several parameters: the length of cable returned by automated segmentation, l_{cable}; the rate of fully manual tracing of bare cable, r_{manual}; the context-switch time for expert attention when completing review of one skeleton fragment and progressing to the next, t_{cs}; and the ratio of the rate at which skeleton cable can be reviewed versus manually traced de novo, c_{review}. A model predicting

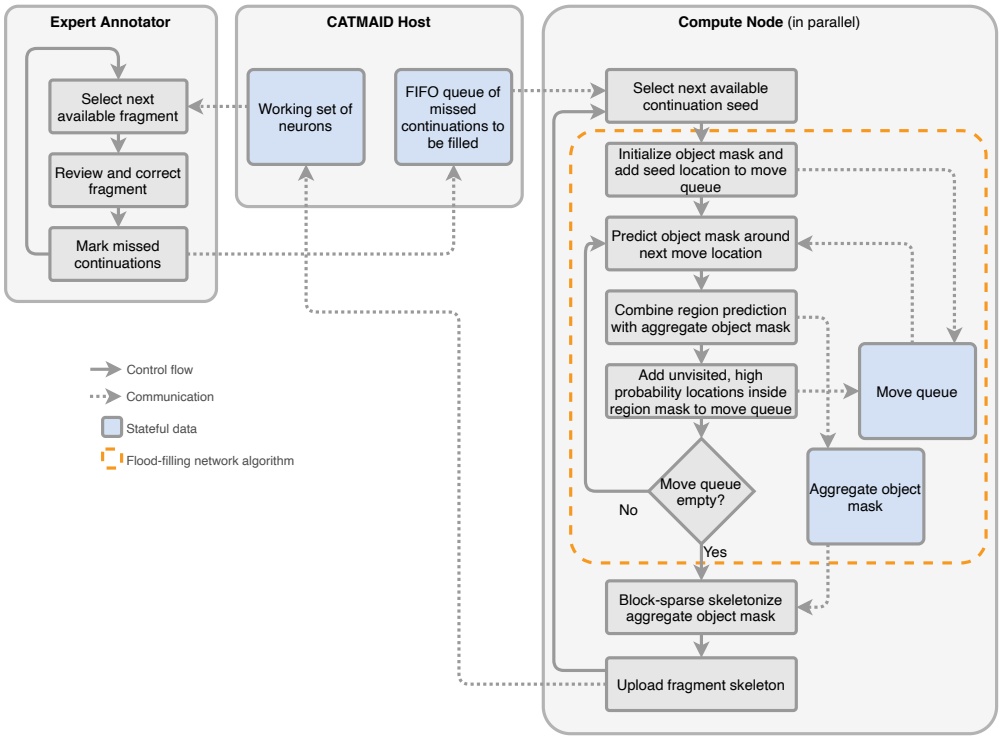

Fig. 3.4 Workflow for Sparse, Semi-Automated Skeletonization. Within CATMAID expert neuroanatomists annotate locations to seed reconstruction within neuronal processes of interest. These seed locations are asynchronously flood-filled, skeletonized, and imported into CATMAID. Once the skeletonization is imported, it is added to a queue of such skeletons for the expert to review. As the expert reviews each skeletonized segmentation fragment, she splits skeletons at locations where neuronal processes are falsely merged (similar to fully manual tracing workflow [117]), and annotates locations where false splits were made, i.e., the neuronal process continues but segmentation did not. These locations are added to segmentation just as with seed locations, and when their skeletonized segmentation fragments are imported they are stitched into the existing skeletons as morphological continuations. These continuations are reviewed in the same workflow as newly seeded skeletons.

approximate speedup S_t is given by:

$$S_t = \frac{c_{review}}{1 + \frac{t_{cs} c_{review} r_{manual}}{\mathbb{E}[l_{cable}]}}$$

Based on existing reconstruction in adult *Drosophila* these parameters are estimated as $r_{manual} = 8\,\mu\text{m/min}; t_{cs} = 0.25\,\text{min}$. Note that t_{cs} may be highly skewed; the median context switch is much shorter, but context switches into difficult processes are much longer. An additional basis for the estimation of review to de novo manual tracing rate ratio is that morphological reconstruction tools that allow experts to trace skeletons by flying through spherical projections of isotropic data have demonstrated a cable reconstruction rate up to four times as fast as manual tracing in CATMAID [114]. While this rate is not achievable for de novo tracing in the reference ssTEM *Drosophila* larva due to different constraints on image quality, alignment, and tortuosity of larval neuronal processes, those limitations do not apply to review of existing skeletons where the skeleton geometry can be used to dynamically prefetch and realign image data.

3.3 Results

3.3.1 Structural Imaging of Multiple Complete Central Nervous Systems

An aligned 10 µm per side cubic region of interest from VNC neuropil of the first acquired pilot sample 1019 (imaged at 16 nm × 16 nm × 8 nm) was used for preliminary assessment of imaging conditions and quality. Seed points for reconstruction were placed near the center of the region of interest in two neurite tracts. Two neuroanatomical reconstruction experts, Casey Schneider-Mizell and Katharina Eichler, and myself were unable to reliably independently reconstruct neurites in these tracts to the boundary of the region, mostly due to low contrast between membranes and intracellular space when processes narrow. Consequently imaging resolution was adjusted to isotropic 12 nm for all subsequent samples.

All eight subsequent samples chosen for electron microscopy were imaged successfully and without tissue loss or anomalies that prevented registration. As shown in Figure 3.5, in some samples and regions ultrastructure critical to the proposed methods is resolvable: intact cell bodies and rind, large neurites in neuropil, and the entry of primary neurite bundles into the neuropil. Registration yields orthogonal views without major distortion or banding along the imaging plane.

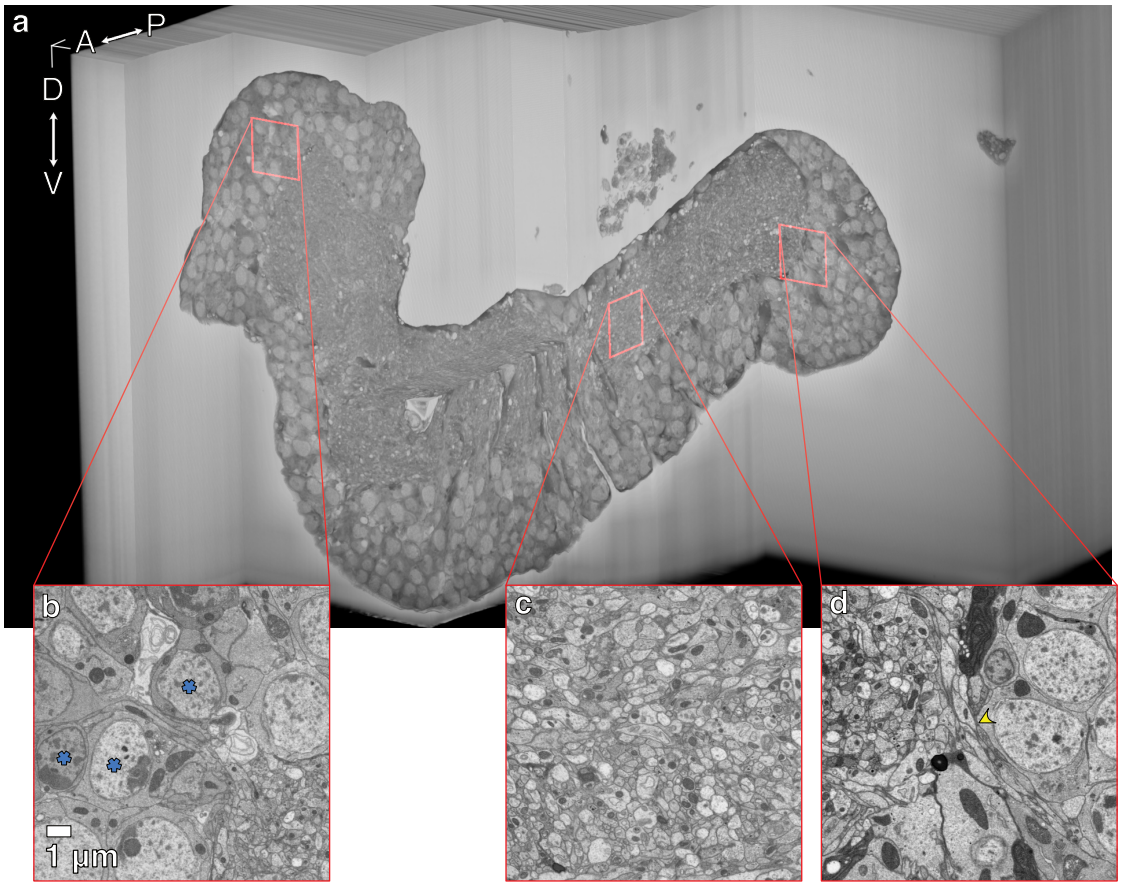

Fig. 3.5 FIBSEM of a Complete Larval *Drosophila* CNS. **(a)** Cutaway rendering of the registered volume of the CNS of a first instar larva (sample 1128). The right brain lobe (image left) is shown in sagittal and frontal section, along with the subesophageal zone (SEZ). A sagittal section extends from the SEZ through the thoracic segments and into the abdominal segments. Finally a frontal section shows the cross section of an abdominal hemisegment. Scale bars are 10 µm. **(b)** Detail of cell bodies in the brain bordering the brain neuropil in the bottom right, with nuclei of varying contrast (blue stars). **(c)** Detail sagittal view of ventral nerve cord neuropil orthogonal to the imaging plane showing imaging isotropy and registration quality. **(d)** Detail of a primary neurite bundle entering the neuropil from cell bodies (yellow arrow).

To assess whether this imaging quality is consistent enough within and between samples for morphological reconstruction, the peduncles of the mushroom body can be compared (Figure 3.6). While the mushroom body is not a system of interest for this work, the peduncle is useful as a representative, stereotyped, and easily identifiable non-branching parallel fiber tract. As such it presents a minimal threshold case for the ability to reconstruct primary neurite morphology. In many samples neurites within the peduncle can not be reconstructed, due to apoptosis, low contrast, or other quality issues. These issues may effect some or all of the peduncle neurites in each sample, and occur in samples from different developmental stages and in both the activity and neurotransmitter samples, which underwent different LSM protocols. While the peduncles for each sample are not necessarily representative of the median image quality of that respective sample, in my observations they are representative of the categories and frequency of image quality issues across all eight samples.

Structural imaging quality issues in these samples leading to unresolvable ultrastructure are categorized in Figure 3.7, broadly in ascending order of severity. While FIBSEM creates imaging artifacts, relative to artifacts in ssTEM including tears, folds, precipitate, and lost sections, FIBSEM artifacts are of very low frequency and low severity and only rarely obstruct reconstruction. As expected, the staining, imaging conditions, and resolution are not sufficient to reliably resolve synapses, post-synaptic partners, or fine dendritic processes.

More importantly for primary neurite reconstruction, low and variable contrast and noise can prevent neighboring processes from being distinguished. In many regions tissue has been damaged or destroyed, preventing any reconstruction or even hypotheses about cell body identity of primary neurites. This occurs most frequently and severely when apoptotic sheathing glia at the interface of the cell body rind and neuropil delaminate the two, severing lineage bundles. Separately from spatially localized regions of cell death, apoptosis and neurite membrane tears occur sparsely throughout all samples with different per-sample frequency. Cell death and tissue destruction may be due to phototoxicity from light sheet illumination and optogenetic stimulation, sustained fictive activity following dissection, and the time and handling required for sequential imaging in two modalities. Recommendations to diagnose and ameliorate these issues are discussed at the end of the chapter.

3.3.2 Manual Reconstruction of Primary Neurite Morphology

To test whether primary neurites for large populations of neurons sufficient for this project's aims could be reconstructed, cell bodies and portions of primary neurites were manually reconstructed for many neurons in first instar GCaMP sample 1018. Because contrast and apoptosis issues often obstruct the entry of lineage bundles from the cell body rind into the neuropil, these reconstructions aimed to map sufficient cable length from the cell body to pass

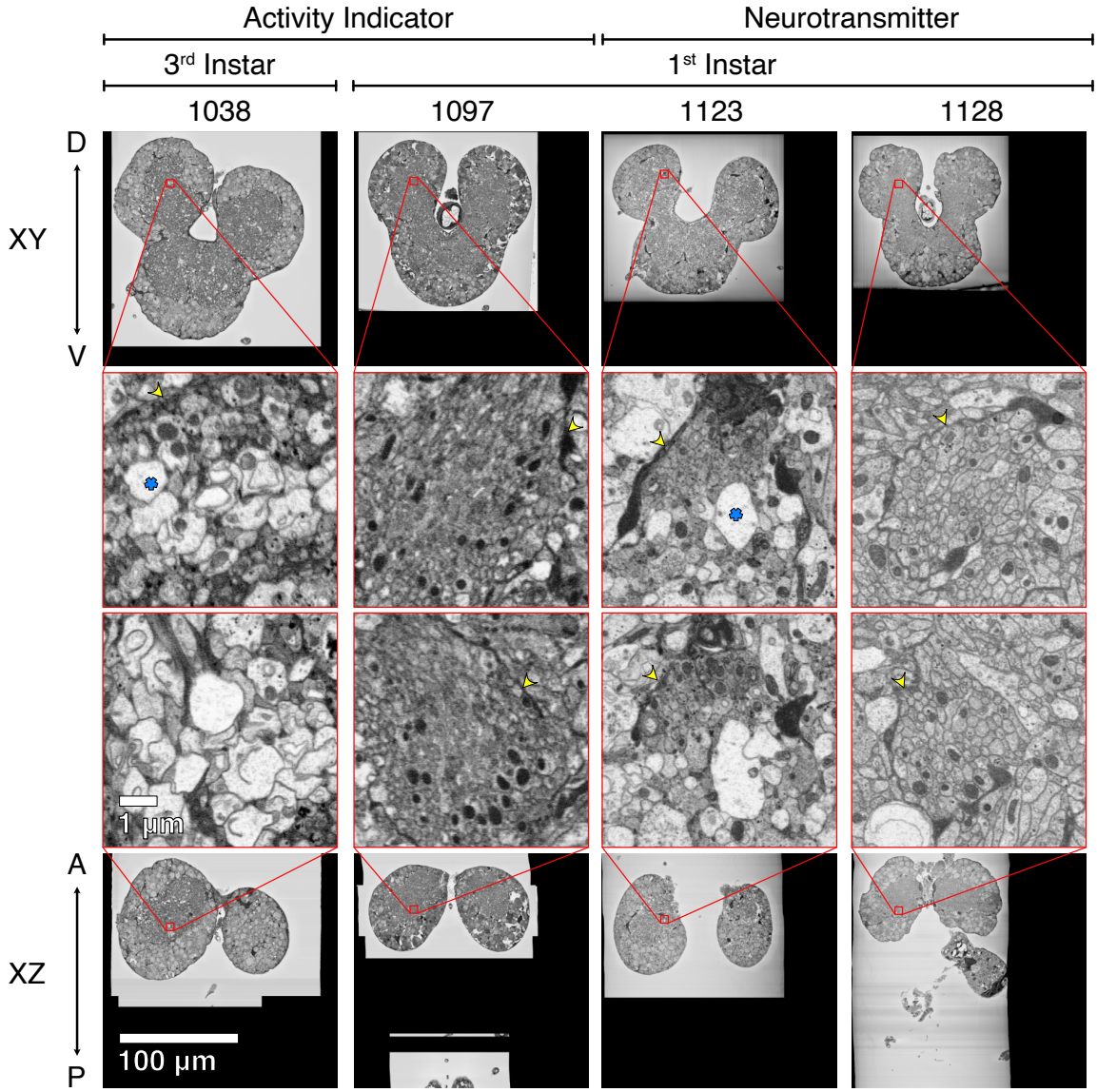

Fig. 3.6 Inter-sample Comparison of Structural Imaging Quality. For each of four larva across developmental stages and prior light imaging representative of the variability of imaging quality (columns), a whole-sample overview in the imaging plane (top row) and a full-resolution region in the peduncle of the mushroom body (second row) are shown. The same are shown for an orthogonal view in the registered volume (fourth and third row, respectively). The boundary of the peduncle is identifiable from glial sheathing (yellow arrows), but integrity of the fibers due to apoptosis (blue stars) and membrane contrast varies between samples.

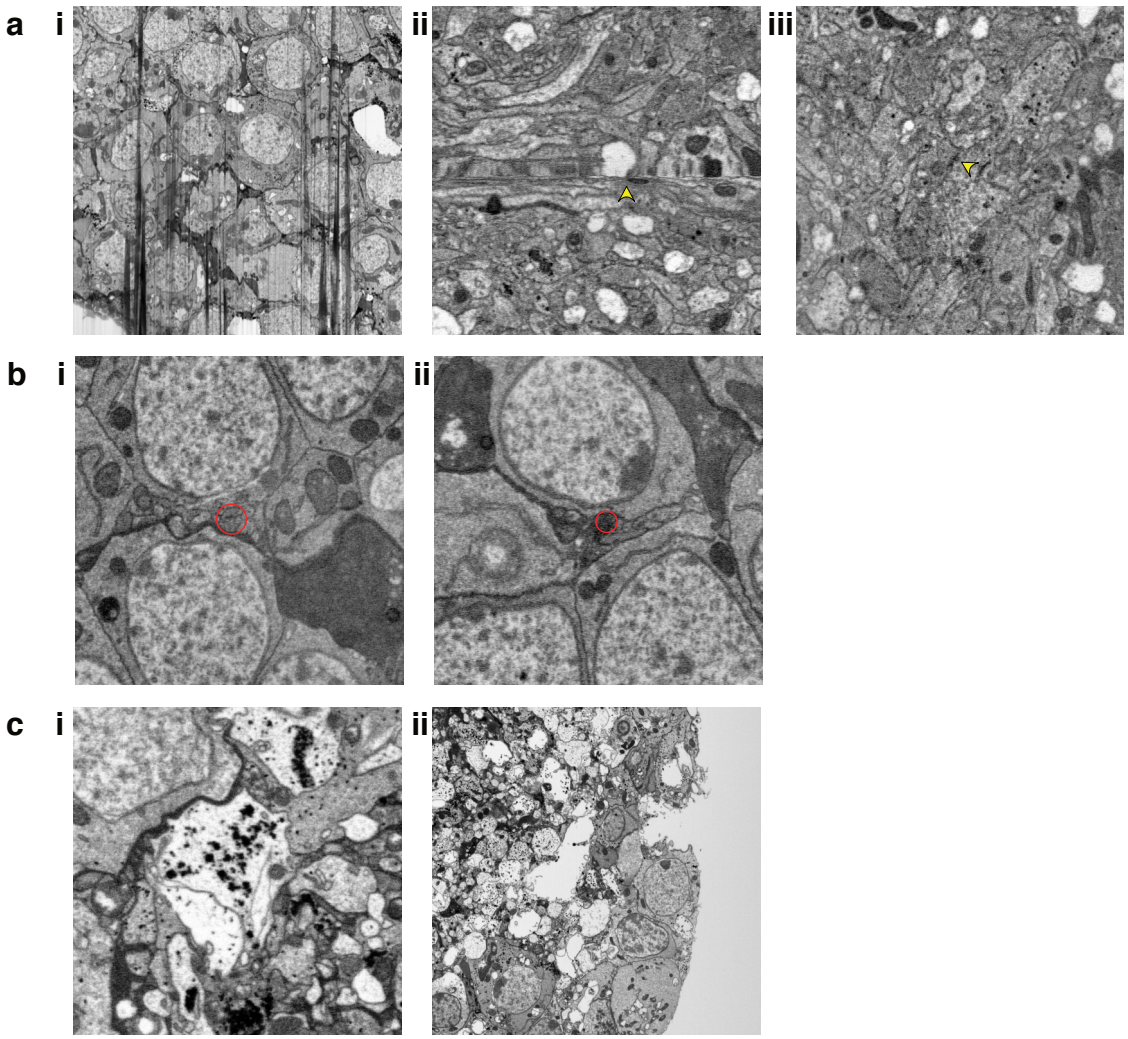

Fig. 3.7 Categories of Sources of Unresolvable Ultrastructure. **(a)** Artifacts and limitations of FIBSEM imaging. *(i)* "Curtains" streaking imaging due to charge buildup. *(ii)* A milling "wave" shown in XZ (transverse section) due to inhomogeneous milling of the sample between each imaged plane. *(iii)* A synapse with presynaptic T-bar (yellow arrow). **(b)** Ambiguous contrast issues from stain and imaging conditions impacting morphological reconstruction. *(i)* Low and inconsistent contrast can create indistinct membrane boundaries, such as here where four primary neurites are within the red circle, but cannot be reliably tracked through this region. *(ii)* High variability in intracellular cytoplasmic contrast can aid tracing in some bundles, but impedes it when dark contrast processes border each other, as shown. Here two primary neurites within the red circle cannot be reliably tracked through this bundle. **(c)** Degradation of tissues preventing morphological reconstruction. *(i)* Membranes and organelles of an apoptotic cell. *(ii)* Cell bodies delaminated from the neuropil through a combination of either apoptosis of the glia and mechanical stress between light sheet microscopy and fixation for electron microscopy.

the entry point for each neuron, so were done with a minimal target length of 25 µm. These reconstructions also scaffold subsequent circuit-targeted work by annotating dense clusters of cell bodies and lineage bundles, so that targeted reconstruction can quickly identify, locate, and extend these. Reconstructions were localized to the right hemisegments of T3 and A1-3 for investigating motor circuitry questions of this thesis, and to two brain regions to assess applicability of these methods to brain circuits for separate systems questions.

For the VNC, reconstruction began at lineage bundle entry points to the neuropil, traced retrogradely to the cell body, then out from the entry point into the neuropil to complete the target cable length. Rebecca Arruda and Nadine Randel also contributed to these reconstructions that are overviewed in Figure 3.8.

71% of neurites could be reconstructed to the target cable length. This metric is a lower bound on the proportion of neurites that can be traced into the neuropil, as review, targeted reconstruction effort, consensus, or semiautomated methods could extend some neurites. However, it is not a bound on the proportion of neurons that can be identified via morphological matching, as 25 µm of cable is insufficient for reliable, accurate NBLAST matching. While this bound limits the proportion of a wiring diagram than can be augmented using the proposed methods (see Figure 5.1), the reconstructions still demonstrate the feasibility of these methods if the ultrastructure and imaging quality present in regions of the samples can be more consistently achieved throughout samples by refinement of the process.

3.3.3 Neuronal Populations of the Central Nervous System

Tissue classification (Figure 3.9) accurately segments cell body rind sufficient for subsequent nuclei segmentation and for mesh generation for orientation in annotation tools. Spurious detections are easily filtered with morphological opening. SVM classification of detected nuclei was sufficient to filter most spurious detections from large organelles and esophageal cells that the remaining detections can be used to check for missed cell bodies of manual reconstructions. While spurious detections remain, they are infrequent enough to be manually discarded.

3.3.4 Suitability of Flood-Filling Networks for Sparse Segmentation

One feature of FFNs that made them potentially relevant to the proposed methods is the ability to segment specific neurons of interest individually. This would allow computational costs of segmentation to be applied sparsely or iteratively to reconstructing particular neurons of interest based upon evolving, circuit-analysis-guided understanding of which neurons' activity augmentation would most clarify circuit model hypotheses. As shown in Figure 3.10,

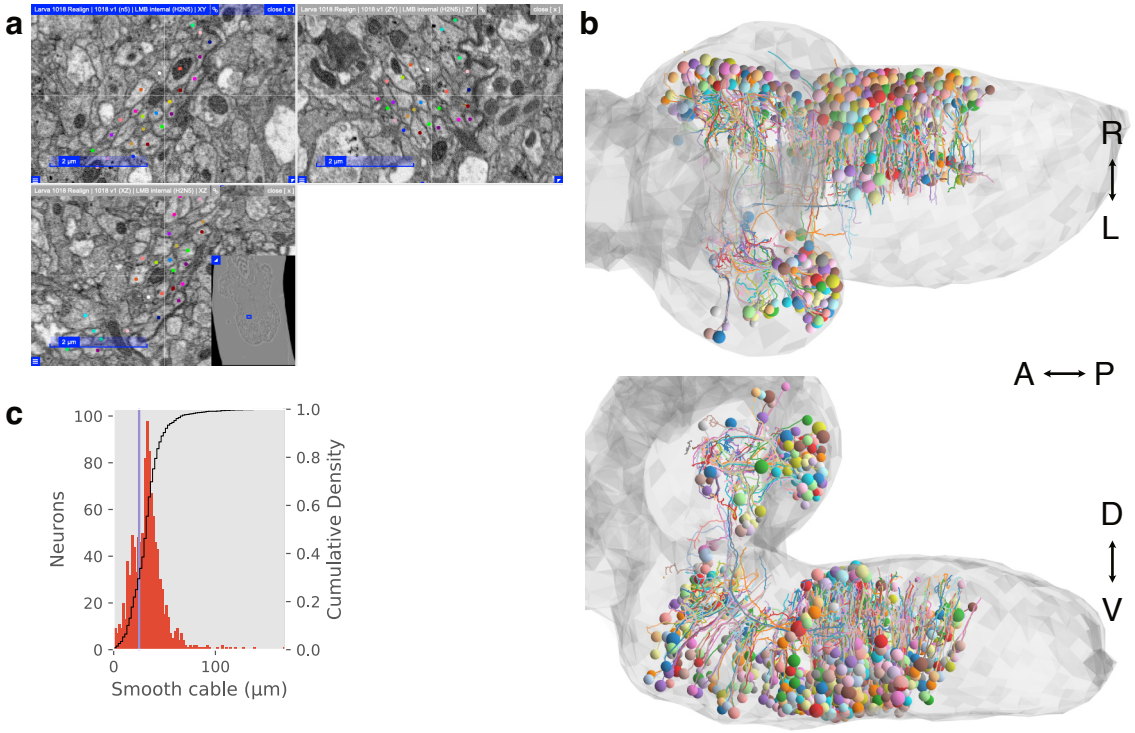

Fig. 3.8 Manual Reconstruction of Primary Neurite Morphology. **(a)** Orthogonal views of the neurite tracing interface in CATMAID. **(b)** Transverse and sagittal views of reconstructed neuron morphologies (sample 1018, $N = 1061$). **(c)** Histogram of cable lengths of reconstructed neurons. The cumulative density (black line) shows that 29% of neurons reconstructed in exploratory tracing could not be quickly traced to the minimum target length of 25 µm.

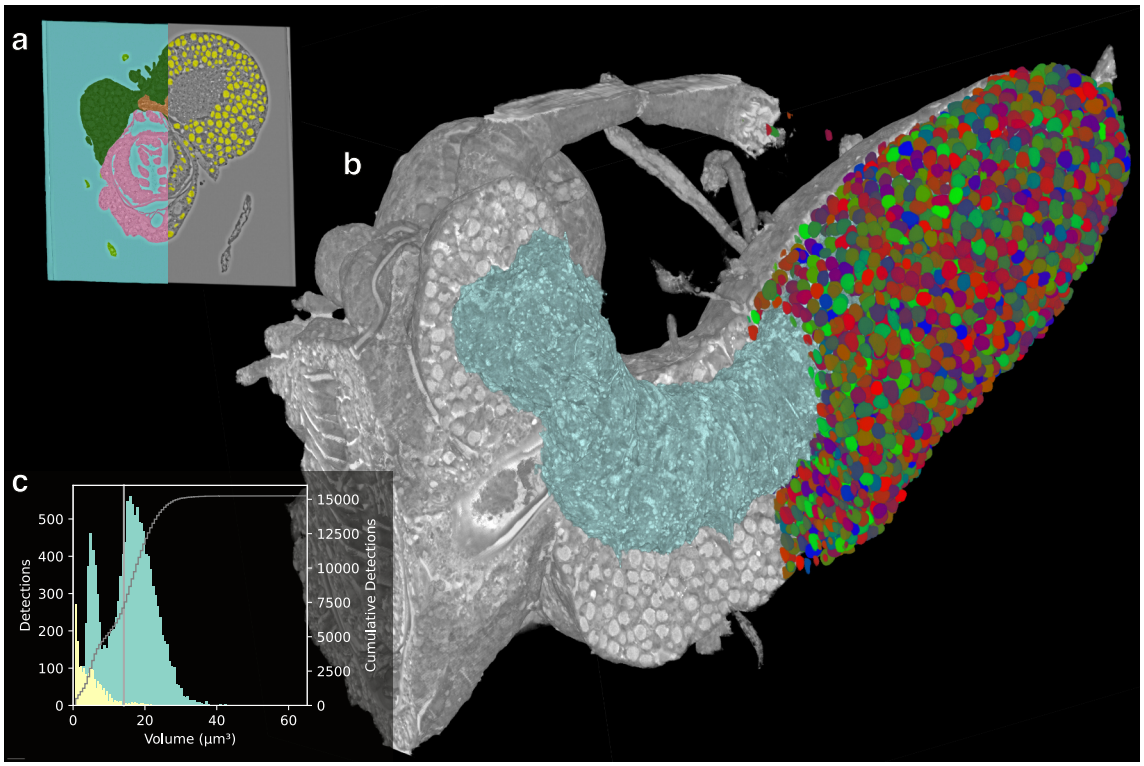

Fig. 3.9 Tissue and Nuclei Segmentation of the CNS. **(a)** Example ground truth annotation for tissue type classification (left) and nuclei detection (right). **(b)** Rendering of FIBSEM of a first instar larva (sample 1018) masked with segmentation and nuclei labeling. The cell body rind mask exposes the tissue from the embedding material, with the esophagus and peripheral nerves visible, along with cell bodies tiling the CNS. In the foreground the neuropil mask is exposed (blue). Posteriorly labeled nuclei detections are shown, and can also be seen in the esophagus. **(c)** Histogram of volumes of nuclei in this sample classified as neural or glial (blue, $N = 13173$) or other (yellow, $N = 2077$) by SVM. The volume of the mean measured manually anotated neuronal nuclei radius of 1.5 µm is shown in gray.

while dense segmentation of sub-volumes can produce segmentation with few merges when the intersection of all process-seeded segmentations is taken, individually seeded segmentations frequently falsely merge. Further, because false merges can introduce recurrent object mask probabilities unlike the distribution from training, and because the network has no means of resolving these (no local choice about which process is correct can be made because it is a global consideration), once a false merge has been made it can lead to many more. Fine processes like sheathing glia are especially susceptible. In the case of dense segmentation with intersecting labels, these frequent false merges are still evident as false split boundaries at axis-aligned planes corresponding with the edge of the output region of interest for individual predictions of the network (Figure 3.10c). Such splits can be trivially detected and merged before any more sophisticated agglomeration is applied.

To investigate network- or object-specific biases towards merging, two networks with the same training procedure but identically, independently drawn initial parameters and training data were repeatedly used to segment the same single objects in sub-volumes of varying size (Figure 3.10e). For each trial, random seed points interior to the object were chosen to initiate the segmentation, but the same sequence of random points is used for both networks. The F_1 metric of the final segmentation and the ground truth is then computed. There is little consistency to when false merges occur, other than that as expected larger sub-volumes have low F_1 more frequently because there is more opportunity for false merging. This variability of behavior, both within and between network segmentations, suggests that FFNs' accuracy may be due to ensemble consensus of segmentations and not only single-object accuracy. One interpretation is that FFNs are modeling and repeatedly sampling from some posterior distribution of segmentations, though other possibilities are listed in the discussion below.

To assess potential speedup versus manual reconstruction for the single-object, targeted skeletonization case, the CATMAID-integrated FFN was used to segment randomly seeded neurites in mushroom body calyx in an adult *Drosophila* ssTEM volume [57]. For narrow-radius processes correct cable lengths are short, while for large processes correct cable lengths are more variable. However, the mean correct cable length yields expected speedup over manual de novo tracing. Since these results, semi-automated approaches based on FFNs [146] and other segmentation methods [115] have achieved speedups over manual reconstruction orders of magnitude greater.

3.4 Discussion

The ability to perform most steps of acquisition, processing, and analysis necessary for augmenting wiring diagrams with high throughput has been demonstrated. With high-current

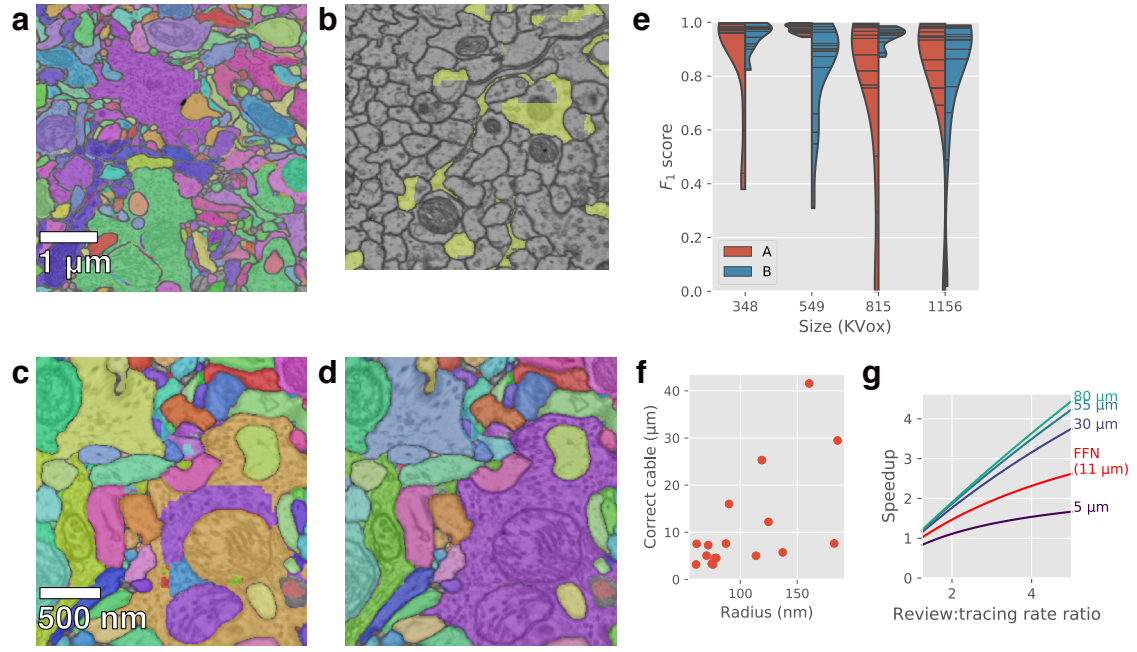

Fig. 3.10 Flood-Filling Networks for Sparse Segmentation. **(a)** Example region of adult *Drosophila* ssTEM densely segmented with the flood-filling implementation from Section 3.2.6. **(b)** Flood-filling of a single object falsely merging into many objects, in this case including a glia. **(c)** False splits in dense flood-filling with characteristic axis-aligned boundaries due to region of interest effects. **(d)** Agglomeration of **(c)** via trivial merging of checking-plane-aligned boundaries. **(e)** Analysis of single-object segmentation between two similarly trained networks. For varying sizes of region of interest volumes, a single object is selected and flood-filling is seeded at random interior locations. After exhausting the FFN's movement queue, F_1 metric of the resulting segmentation with the ground truth is taken. **(f)** Correct cable lengths versus neurite radius for sparse skeletonizations in adult *Drosophila* mushroom body [57]. **(g)** Estimated speedup versus manual tracing for the results in **(f)** based on a simple model accounting for a rate ratio of review versus de novo tracing.

FIBSEM microscopes, first instar larval volumes can be acquired in less than two weeks. A fully distributable processing pipeline allows registration, tissue segmentation, nuclei detection, and import into analysis environments in under a day. Landmark placement for morphological identification requires a similar scale of time for robust placement once per sample. These capabilities all minimize the marginal time and cost required per augmentation sample, which allows for collection of many samples representative of inter-individual variability or diverse experimental conditions.

Damaged and ambiguous ultrastructure limits both the throughput of this process and the proportion of the wiring diagram that can be augmented. Manual reconstructions found up to 29% of neurons in one sample may not be identifiable. For a sample of neurons that passed that threshold, a neuroanatomical reconstruction expert achieved a mean cable rate of 3.3 µm/min (Figure 5.3), demonstrating structural imaging quality issues limit reconstruction rate in addition to feasibility.

Future work can address these issues in three ways: reducing tissue damage, improving imaging, and automating reconstruction. Tissue damage can be reduced by limiting the exposure of the sample during LSM. While acquiring functional imaging for long intervals to observe many behavioral bouts is valuable for activity analysis, improvements in the throughput of methods elsewhere have reduced the time and resources required for each sample, thus reducing the need to maximize observed activity in each individual sample. Observation of apoptosis onset [154] can inform reduction in functional imaging time.

For structural imaging, improvements in the acquisition rate of FIBSEM microscopes allow for a larger envelope of imaging parameters to be considered. Relatively low resolutions for *Drosophila* connectomics of 16 nm and 12 nm were chosen to allow acquisition of several samples in a period of months and each in a sufficiently short window based on the microscopes' mean time between failures. With higher acquisition rates and more reliable microscopy, higher resolution acquisition could prevent some ultrastructure ambiguities.

Computer vision-based semi-automated reconstruction can both improve the rate of reconstruction of currently reconstructable neurites and aid in reconstructing challenging cases. Segmentation-based semi-automation can yield expected correct cable lengths of 163 µm in 8 nm isotropic FIBSEM of partial adult *Drosophila* brain [59]. While the imaging and tissue conditions are less ideal for the high-throughput context here, orders of magnitude speedup versus manual reconstruction are likely. Complementary to this, the density of reconstruction in the reference dataset can be exploited to create priors for agglomeration of over-segmentations. Via the existing landmark registration, reconstructions in the reference dataset can be transformed into each augmentation sample. Where reconstruction is spatially dense, segmentation fragments should merge in a way that maximizes the quality of

bijective morphological matches with the reference reconstructions, which can be posed as a constrained optimization problem for automation. Such neurite morphology priors can also help resolve ambiguous cases when they occur sufficiently distal from the cell body.

3.4.1 Flood-Filling Networks

The potential factors behind FFNs' accuracy and robustness at dense instance segmentation can be broadly factored into four aspects of their operation:

1. Single-object focus
2. Multiple hypotheses
3. Recurrent context
4. Incremental improvement (recurrent attention)

While these factors are not independent, they do seem to be exhaustive, as other proposed explanations for FFNs' accuracy can be synthesized from them (e.g., the relative simplicity of the network architectures required is principally due to 1 and 3, the anti-merge bias is principally due to 2 and 4).

Another proposed factor, multi-scale context and operation, is in published FFN work implemented identically to factor 2 [80]. The results here are evidence that factor 1, single-object focus alone is not sufficient explanation. Future work could investigate alternative algorithms that employ only subsets of these factors to disentangle their contributions and inform design of more accurate or efficient approaches.

As FFNs' low incidence of false merges was not preserved for single-object segmentation, they do not have particular suitability for the sparse, circuit-guided, semi-automated reconstruction that originally motivated its investigation for this project. Dense segmentation with FFNs requires computationally intensive consensus of many segmentations and merging of the resulting over-segmentation [80]. However, the computational costs of this process are less restrictive than they were at the time the above results were produced, due to improvements in GPU performance for CNNs. Therefore dense segmentation with FFNs may still accelerate high-throughput neuroanatomy for wiring diagram augmentation in the future.

Chapter 4

Correlation of Light Sheet and Electron Microscopy

To associate activity or fluorescent markers from light sheet microscopy (LSM) with neuronal identity established in subsequent focused ion beam scanning electron microscopy (FIBSEM) of the sample via the methods in Chapter 3, somatic fluorescence loci in the LSM must be matched with cell bodies in the FIBSEM. This is achieved by spatial co-registration between the two modalities. Several inherent problems must be addressed for co-registration and somatic identity mapping:

- LSM and FIBSEM capture distinct features of samples with complex and non-uniform generative relationships.
- LSM's spatial resolution is orders of magnitude lower than FIBSEM, and highly anisotropic. Unlike FIBSEM it is subject to inhomogeneities across tissue depths and distance from the objective.
- LSM's axial spatial resolution is similar in scale to the somatic activity of interest. As described below, light sheet thickness in the acquired data is approximately 2 µm, similar to the radius of a cell body in first instar larvae. This can create difficulty in distinguishing neighboring somatic signals especially when adjacent orthogonal to the light sheet.
- Unlike some other types of neural tissue where cell bodies are distributed or layered throughout, in larval *Drosophila* central nervous system (CNS) cell bodies are densely packed in the rind. This complicates the matching problem as one or a group of somatic signals to be matched may alias with many false matching sets neighboring the correct match. Cell bodies and somatic activity signals are also relatively self-similar, so little

information about correct matching is contributed by individual matching candidate pairs and most processes must rely on group-wise match information. Likewise the grouping structure of cell bodies in the CNS has dimensions of partial self-similarity, most notably the axially repeating and locally rotationally similar structure of the VNC,which makes aliasing along the anteroposterior axis possible.

- While larval CNS have on the order of 10,000 neurons (see Figure 3.9), functional imaging of fictively moving explants have sparse activity on the order of 200 neurons [21]. Matching between the sparsely detected somatic signals of LSM and the nearly complete neuronal cell body detections in structural imaging exacerbates the aliasing problem described above, as each detected somatic activity has many potential matches with few constraints.

- The CNS must be handled after LSM to remove it from the agarose embedding and prepare for FIBSEM imaging. Consequently the sample deforms and may be damaged.

As few manual processes are involved in the proposed methods, these problems are not potential limitations to the throughput of augmenting wiring diagrams, but to their completeness and accuracy (see also Figure 5.1).

4.1 Background

Before LSM can be co-registered to electron microscopy (EM), it must be registered to itself to align images from multiple cameras and acquired at successive times, a similar process as EM registration (Section 3.1) These times may be either within each sweep of the illuminating light sheet, representing serial optical slices of the sample to be registered into 3D, or across multiple sweeps of the light sheet, representing timepoints to be registered into 4D. Registration between cameras is challenging because of the variation of the image of a given sample location between cameras and between sheet-camera sets in iso-view LSM (Section 2.3). This is caused by scattering, both absorption and refraction, of each illuminating light sheet and the fluorophore-emitted light detected by each camera.

Many approaches to registration use similar point-matching strategies to those employed in EM. Unlike the primarily 2D registration of EM, since the most difficult steps are the between-camera and across-sweeps registrations, these strategies often exploit the 3D structure of the individual registered time-point-per-camera volumes and the sparsity of the data. For example, constellation features representing the relative arrangement of fiducial markers can augment traditional features based on local image statistics [155]. Sample points of

interest can be extracted from tissue features such as cell body locations to perform similar registration in the absence of fiducial markers [86].

Once registered, somatic signals, either of functional activity or other fluorescent markers, can be detected in the volume. Methods may detect likely somatic signals with traditional, designed computer vision features such as compositions or derivatives of Gaussian filters and clustering across time, or with supervised machine learning based models [156].

Several possible strategies for multi-modal registration of LSM and EM are explained in Figure 4.1. Problems in LSM-EM registration listed above affect each differently. Registration based on manually annotated neuroanatomical landmarks, such as those for registration between EM datasets in subsection 3.2.5, are sparse, often ambiguous due to different imaging characteristics of the modalities, and lack the spatial localization required to approach cell-body-radius, single axial voxel accuracy necessary for establishing somatic identity. Point-cloud registration of somatic detections with FIBSEM cell body segmentations, such as by iterative closest points [157] or with soft pair assignment by robust point matching [158], is under-constrained due to the sparsity of detections and aliasing problems. Mesh-based registration of the surface of segmented tissue structures is often employed in biomedical imaging applications for matching imaged tissues against templates [159, 160]. A similar approach can be employed here between the surface meshes of segmented CNSs. In Figure 4.1e and the methods below, a point sampling is taken and registered with point-cloud algorithms. Direct registration between meshes without point sampling is also possible [161].

Coherent point drift is a point-cloud registration algorithm used below that rather than considering point-wise matches creates a kernel mixture model estimate of the deformable point set's distribution at each iteration [162]. The deformable points (as constituents of the mixture model) are then transformed to maximize the expectation of the fixed point set as a posterior of the model, constraining for coherent deformation. This approach is adaptable to rigid and nonrigid transformation models.

A shortcoming of these approaches is that, other than feature-based point matching, they do not exploit direct information of the multi-modal image data, only features and segmentations derived from it. This limits the registration from being learned or optimized end-to-end. Other approaches can learn generative models or similarity metrics between image pairs, either unsupervised or supervised [163], to fit deformable transforms or infer deformation fields.

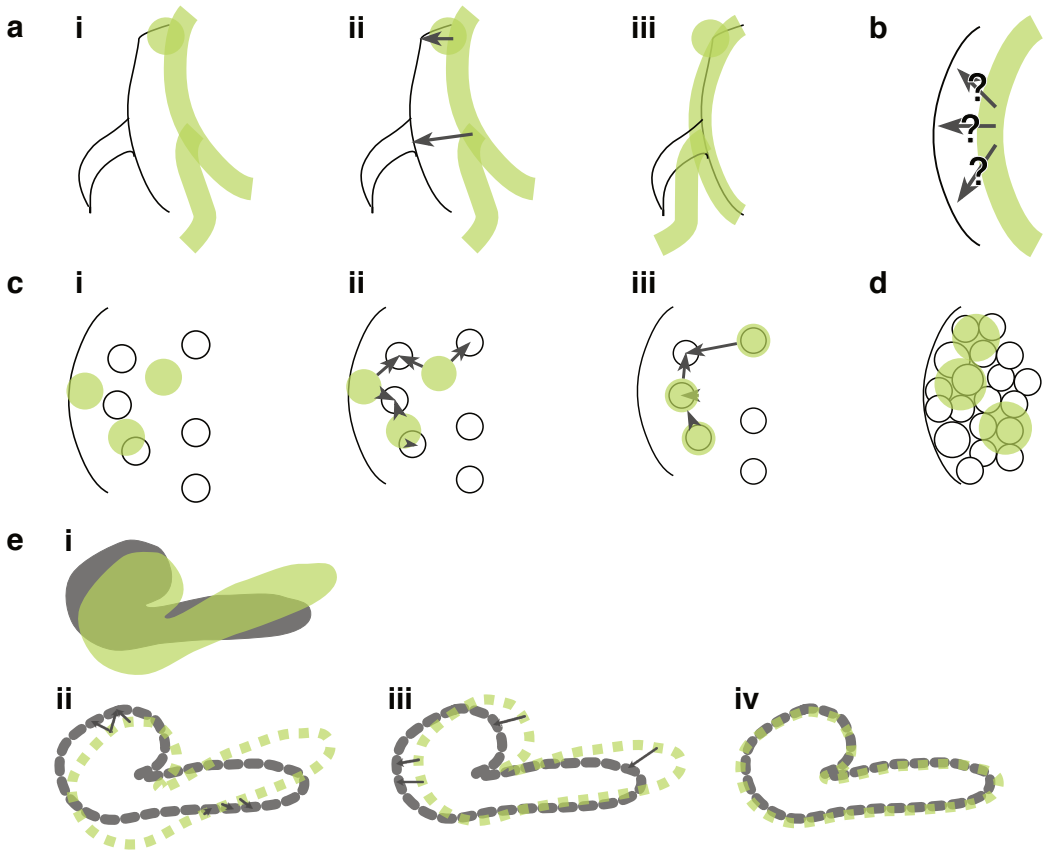

Fig. 4.1 Cartoon of Possible LSM-EM Registration Methods. In these cartoons a moving LSM image (green) is registered to a fixed FIBSEM image (black), but either direction is possible. **(a)** Landmark-based registration. **(i)** Along visible structures such as the contour of the VNC profile in FIBSEM (black line) and LSM (green line), pairs of distinctive point locations such as protusions or peripheral nerves in **(ii)** can be identified either manually or with block matching and a generative cross-modality model. Transformation can align these when sufficient landmarks are available. **(b)** Even when correlated structures are visible, landmark-based registration can not be accurately applied if no distinctive feature locus is present, such as for tissue surface boundaries. **(c)** Constrained point-cloud registration of somatic detections. **(i)** Given a set of FIBSEM cell body detections (black circles) and LSM somatic signal detections (green circles), coherent individual matching may not be possible due to multiple candidates in a local neighborhood as in **(ii)**. **(iii)** The matching assignment can be formulated as a constraint satisfaction preventing multiple assignments to the same match while maximizing local consistency of the resulting transform. **(d)** Due to density of cell bodies in the CNS rind, sparse activity during functional imaging, and low LSM localization, point-cloud registration of somatic detections is subject to ambiguous cases and aliasing. **(e)** Mesh-based tissue registration. **(i)** From a segmented mesh of the tissue, sampled point locations **(ii)** can undergo a similar point-cloud registration as **(c)**, but with soft assignment allowing points to transform to maximize fit to a distribution estimate of their neighbors rather than to particular matches. **(iii, iv)** The process is applied iteratively.

Sample	Ca_2^+ Indicator	Optogenetic	LSM Type	Planar Res. (µm)	Axial Res. (µm)
1019	GCaMP6s	Chrimson	IsoView	0.40625	2.03125
1018	GCaMP6s	Chrimson	IsoView	0.40625	2.03125
1038	jRGECO1a	Chronos	MultiView	0.40625	2.5
1085	jRGECO1a	Chronos	MultiView	0.40625	2.3
1097	jRGECO1a	Chronos	MultiView	0.40625	2.3
1099	jRGECO1a	Chronos	MultiView	0.40625	1.7

Table 4.1 List of LSM Imaged Activity Indicator Larvae

Sample	NT Reporter	Pan-Nuclear	LSM Type	Planar Res. (µm)	Axial Res. (µm)
1123	GFP	tdTomato	MultiView	0.40625	1.7
1126	GFP	tdTomato	MultiView	0.40625	1.7
1128	GFP	tdTomato	MultiView	0.40625	1.7

Table 4.2 List of LSM Imaged Neurotransmitter Larvae

GFP is green fluorescent protein [164].

4.2 Methods

Figure 4.2 outlines the multi-modality co-registration process for each dataset, elaborated in the subsections below. These methods employ a combination of the co-registration strategies discussed in the background, pre-registering with manual landmark annotations, using computer vision to segment large-scale tissue structure, registering with the FIBSEM tissue segmentation, and iteratively correcting the result with further landmark-based registration.

4.2.1 Datasets and Acquisition

Dissection and embedding of each CNS was performed by Nadine Randel identically to the methods in [21]. Embedded and mounted samples were imaged through a collaboration with the laboratory of Philipp Keller at Janelia Research Campus. Corresponding with the use of iso-view or multi-view LSM given in Table 4.1 and Table 4.2, samples 1018 and 1019 were imaged by Raghav Chhetri, while the remainder were imaged by Chen Wang. Refer to Table 3.3 for genetic constructs.

Samples 1018 and 1019 did not have targeted optogenetic manipulation of the Basin neurons via the Chrimson channelrhodopsin; due to its absorption spectrum Chrimson is stimulated continuously by the imaging laser [25]. Subsequent activity imaging samples use jRGECO1a [23]) instead of GCaMP6s [22] paired with Chronos to allow independent imaging and stimulus for closed- and open-loop manipulation. As the focus of this thesis is

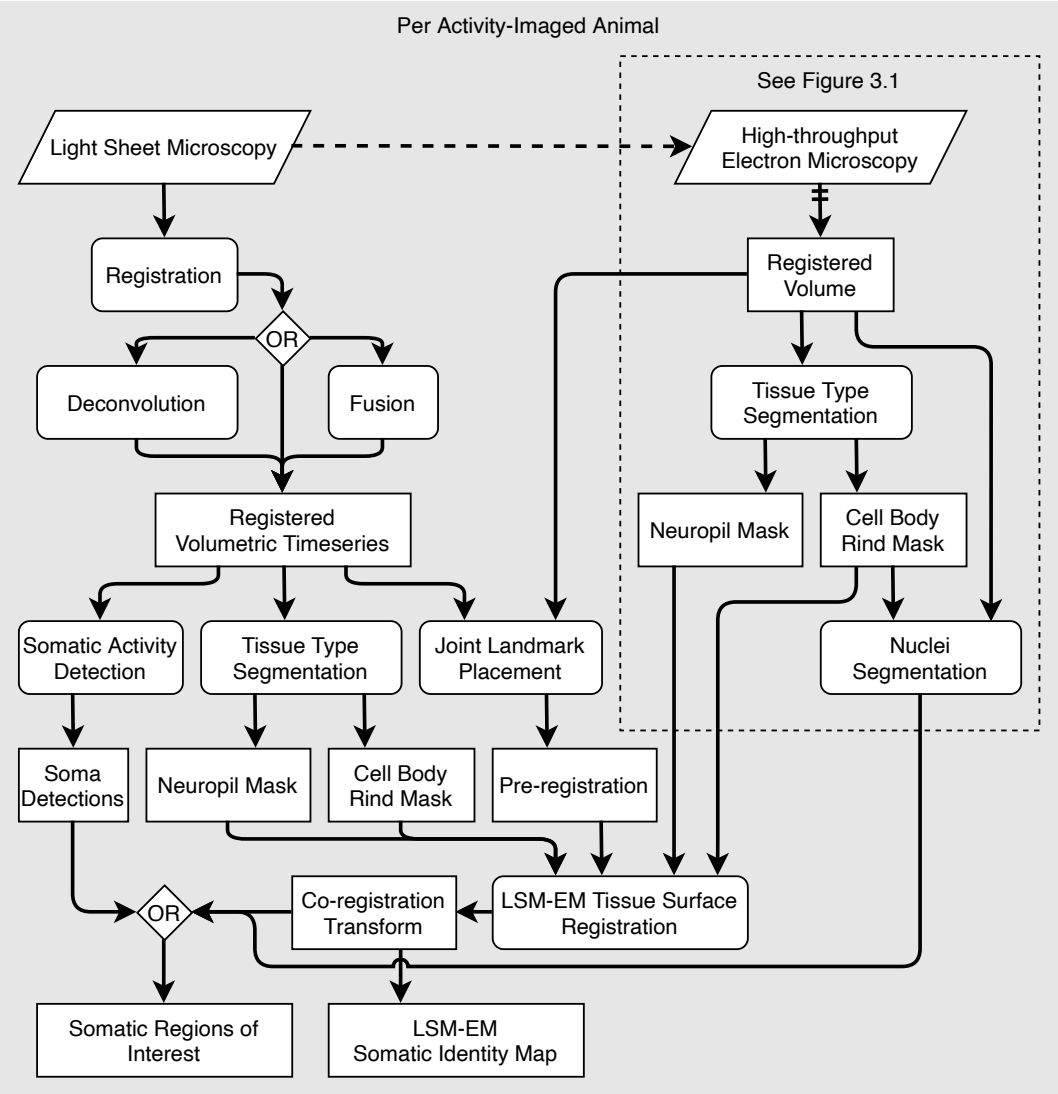

Fig. 4.2 Data Flow Diagram of LSM-EM Registration. This diagram details the contributed methods for co-registering LSM and high-throughout FIBSEM of the same *Drosophila* larva CNS, detecting somatic activity or marker signals, and identifying those detections with cell body detections in the FIBSEM. "Or" nodes represent multiple alternatives which have been used for one or more of the datasets. See Figure 1.2 for an abstracted overview.

methods for creating augmented wiring diagrams and not their analysis, no activity analysis is performed here and the manipulation protocols are omitted. Activity indicator larva are imaged for 30-45 min, preluded by 15-30 min for microscopy calibration.

Samples 1018 and 1019 expressed histone binding red fluorescent protein (RFP), which was imaged in the light sheet subsequent to GCaMP imaging [21]. The separate channel is intended to be used to build template images of nuclear fluorescence to assist in registration of the activity imaging and for co-registration with FIBSEM. Due to apoptosis observed in structural imaging (Figure 3.7), this second imaging process was not performed in subsequent calcium activity indicator animals to reduce the time and phototoxicity of the light sheet microscopy and thus the progression of apoptosis before fixation. A *UAS-H2bGFP* cross for the second chromosome could be used for nuclear imaging otherwise. Neurotransmitter samples expressed nuclear tdTomato [165] to allow for pan-neuronal detection of cell bodies regardless of neurotransmitter label expression, which was imaged.

4.2.2 LSM Registration and Overview

As shown in the LSM-EM data flow diagram (Figure 4.2), several distinct registrations are required: between the multiple cameras' views in LSM and across time for each or all jointly, an approximate LSM-EM pre-registration, and a final LSM-EM co-registration. Additionally, the process must support incremental correction to the LSM-EM co-registration based on proofreading and circuit-analysis-guided discovery of somatic identity matching errors, which may be accomplished by re-registering or a separate post-registration.

Registration between views and over time in LSM is an active area of research with recent methods surveyed above. While it contributes to image and registration quality and thus the feasibility of this thesis' contributed methods, it was not in the scope of explored methods. Multiple existing methods and tools were applied variously to the datasets, including MultiView Reconstruction [155, 166], and block-matching-based registration and GPU deconvolution [167]. Nadine Randel, Raghav Chhetri, Chen Wang, Léo Guignard, Albert Cardona, and myself all created registrations used in subsequent methods.

Acquired and registered LSM volumes are stored in Keller lab block format (KLB) [168], with registered copies or projections exported to N5 [124] for LSM-EM registration and visualization and annotation in CATMAID.

4.2.3 Landmark Registration

Manual landmark annotation is used to create an initial pre-registration been the LSM and FIBSEM image volumes with BigWarp [169]. Rigid registration is used to not introduce any

overfitting distortions given the ambiguity and poor localization of many landmarks. While subsequent registration performs well without this pre-registration, it is useful to inspect the sample for any issues that need to be manually addressed in later steps, such as tissue loss in the FIBSEM significant enough to require manual infilling of its tissue segmentation to match the LSM sample condition. Generating an elastic registration with the same landmarks also allows for estimation of large scale tissue deformation between modalities, such as bending of the brain relative to the VNC or torsion along the VNC, that may require tuning later registration parameters.

4.2.4 Mesh-Based Tissue Registration

Cell body rind and neuropil are segmented from background using a random forrest classifier trained with label data created in Ilastik [170]. Labeling can be ambiguous where CNS boundaries are not distinct, especially along quiescent regions such as the lateral brain, and the ventral surface of the VNC where the sheet-parallel alignment of the tissue causes large regions of low-intensity-variance scattering that make the boundary vague. By inspecting the quality of the resulting co-registration, additional labeling around these regions must be placed in each LSM volume to tune the segmentation classifier.

As peripheral nerves attached to the CNS move during re-embedding protocols for FIBSEM, they create noise if included in registration. Both the LSM and FIBSEM CNS surface mask (rind combined with neuropil) are cleaned with image processing morphological opening to remove these. Manual adjustments may be made to the mask due to tissue loss, brain hemisphere separation, or other issues identified during pre-registration visualization. If the esophagus is attached to the CNS, it must also be removed from the FIBSEM mask, as it does not fluoresce in LSM, although it still contributes to scattering. As esophageal tissue was labeled in its ground truth, the tissue type classifier from Chapter 3 can be optionally trained to output this mask separately.

A mesh is extracted from each segmentation, the LSM mesh is smoothed to match the resolution of the FIBSEM mesh, and both are point sampled. Coherent point drift is applied to the resulting point sets, with LSM as the target and FIBSEM as the deformable set, as being higher resolution its transformed volume interpolates better for visualization. First an affine registration is applied, then a deformable registration is applied. If inspection in napari [143] and BigWarp [169] identifies quality issues, points can be resampled, registration parameters can be adjusted, or transformations from multiple samplings can be averaged.

Following mesh registration, proofreading, refinement, and corrections are made in BigWarp with an elastic registration.

4.2.5 Improving Activity Analysis with Structural Segmentation

An advantage in detection and filtering of activity indicators or other fluorescent markers in this augmented approach as opposed to LSM alone is that once co-registered, structural information from FIBSEM can be used as regions of interests and masks. In these methods, rather than using LSM-derived somatic signal detections, cell body segmentation from the FIBSEM can be transformed into the LSM space and used to extract $\frac{\Delta f}{F}$ activity timeseries or fluorescent label presence for that neuron. If LSM-derived activity detection is still used, transformed FIBSEM neuropil tissue segmentation can mask out neuropil regions in the LSM, which introduce many spurious detections and are difficult to filter with the LSM-segmented neuropil, as scattering makes it less accurate than the rind segmentation.

4.3 Results

4.3.1 LSM-EM Registration of Complete Larval CNS

Mesh-based registration of the CNS (Figure 4.3) yields variable accuracy based on LSM quality, tissue segmentation, and condition of the tissue when it is structurally imaged (Figure 4.4). For some regions of the VNC, mesh-based registration is sufficient for sub-cell-body-diameter accuracy for correct matching. In most regions this is not the case, but the mesh-based registration aids in proofreading identification of landmarks and disambiguation of candidate matches for iterative improvement of the registration. Lack of distinct fluorescence signal of somata or tissue structures, as well as tissue damage following LSM imaging, still yields un-aligned regions without clear corrections.

Due to its much sparser activity during activity imaging in these samples, registration in brain lobes is both less accurate and less densely assessable. Ongoing work is registering neurotransmitter datasets with nuclear markers enabling cell body point-cloud matching (see Figure 4.1 and discussion below) that have more features for registration than activity indicator sample results here.

4.4 Discussion

Mesh-based tissue registration aligns regions in some larval CNS samples with sufficient accuracy to enable subsequent iterative manual proofreading to unambiguously identify matching pairs of cell bodies or regions of interest. Using transformed cell body detections from FIBSEM as regions of interest for somatic signal extraction obviates many problems with detecting distinct somata directly from LSM. However, future work could make use of

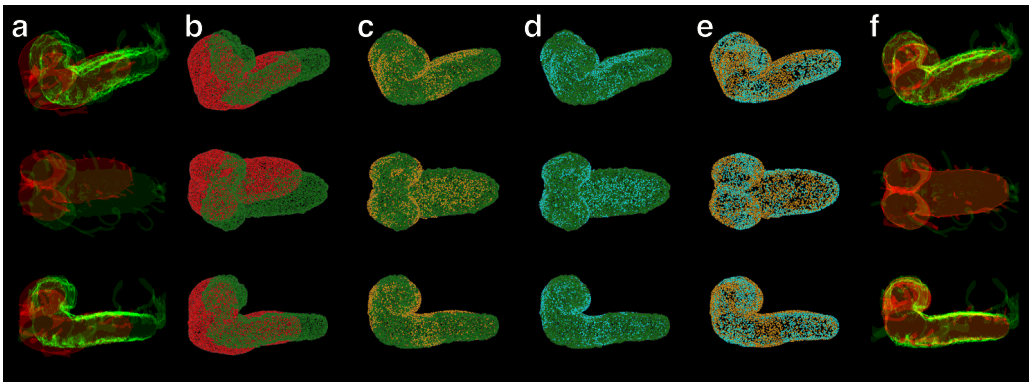

Fig. 4.3 Mesh-Based Registration of Larval *Drosophila* CNS. (a) Meshes of LSM (green) and FIBSEM (red) segmented CNS (sample 1038) shown in perspective, transverse, and sagittal views. **(b)** Point sampling of the mesh. **(c)** Affine registration of the FIBSEM points (orange) to LSM by coherent point drift. **(d)** Deformable registration of the affine-transformed FIBSEM points (blue). **(e)** Comparison of affine and deformable registration steps, as an indicator of deformation of tissue between LSM and FIBSEM. Flattening of the brain lobes and curvature of the VNC are visible. **(f)** Co-registered mesh of the FIBSEM CNS (red) after application affine and deformable transforms.

LSM-derived somatic detections to introduce another constrained point-cloud registration following mesh-based registration and prior to manual landmark correction. While point-cloud registration of somatic detections to segmented FIBSEM is too sparse and under-constrained to be effective as an initial registration or following pre-registration, given the within-cell-radius accuracy of the mesh registration in many locations it could reduce the amount of manual correction required. As discussed in the background, it also functions effectively as mechanism of enforcing manual matching constraints rather than a landmark-based final registration.

The lack of a separately imaged nuclear marker channel as in [21] complicates both the LSM registration and the LSM-EM co-registration. A dense neuronal marker would make the point-cloud cell body registration problem much better posed and potentially eliminate the need for mesh-based registration and most manual correction. While this process was not performed for the majority of activity imaging samples to reduce both time- and phototoxicity-induced damage to the sample, from the results in Chapter 3 it is not clear that it was effective (see Figure 3.6). Imaging the second channel requires time because the microscope must be recalibrated after changing the illumination laser to the appropriate wavelength (15-30 min) during which the sample is being illuminated, while the acquisition itself is only seconds as the signal is not time-varying. Future instrument and protocol improvements could reduce calibration time for both channels, allowing acquisition of both in a similar or shorter interval than the single channel acquisition for existing samples.

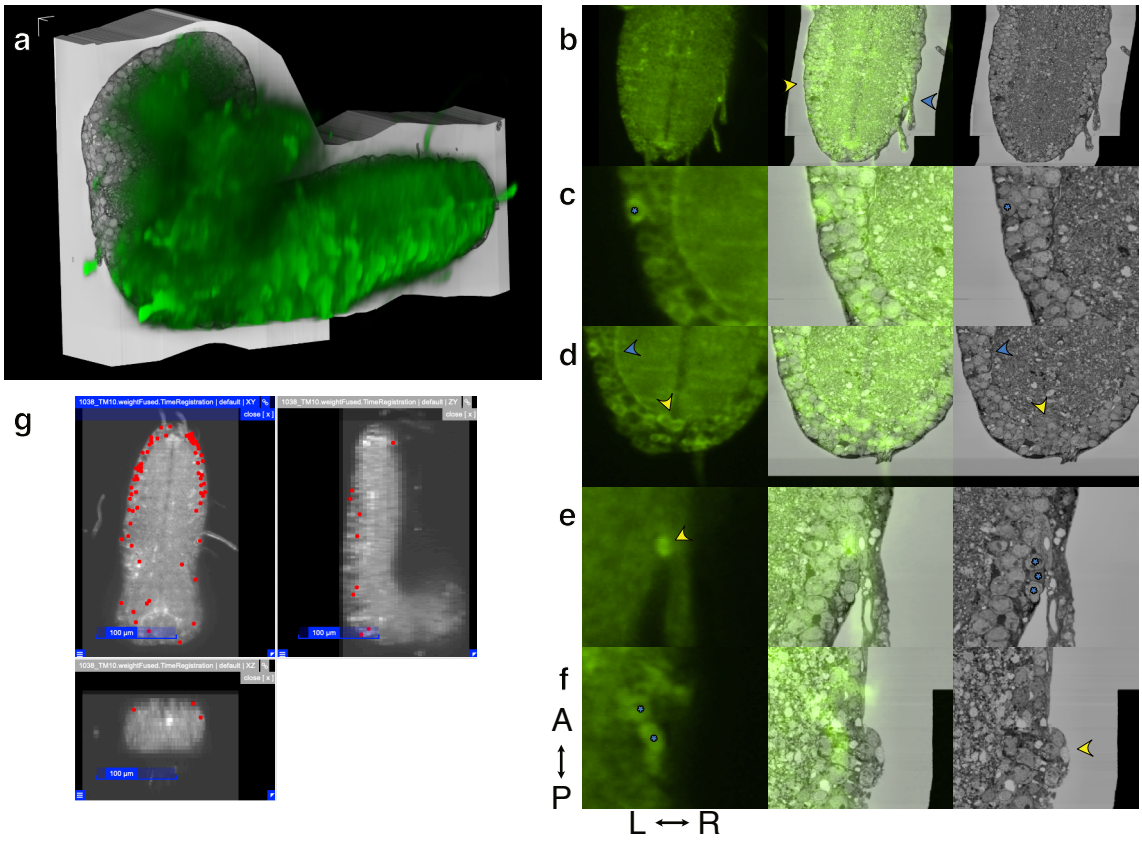

Fig. 4.4 LSM-EM Registration of a Complete Larval *Drosophila* CNS. (a) Perspective rendering of a cutaway of FIBSEM of a complete larval *Drosophila* CNS (sample 1038) registered with calcium indicator fluorescence in LSM. Scale axes are 10 µm. **(b)** Overview of registration quality of mesh-based registration prior to correction. LSM, LSM-overlaid FIBSEM, and FIBSEM sections of the VNC show fit of the cell body right surface (yellow arrow), but less precise fit contralaterally (blue arrow). Transverse sections are shown for all subfigures because low axial resolution hinders interpretation without volumetric or interactive visualization. **(c)** Example of sub-cell-body-radius accuracy in a posterior VNC segment for a well-imaged soma in both modalities (blue star). **(d)** Example of region correctable with landmarks. While the neuropil surface (blue arrow) is well registered, a difficult task for landmark registration, the convergence of two well-imaged somata with the midline (yellow arrow) is offset by approximately half a cell body radius. The registration makes placement of this landmark correction unambiguous, while in the unregistered volumes many candidate convergences for the landmark exist. **(e)** Even when somatic signals are evident in LSM (yellow arrow), matching may be ambiguous. Three candidates in FIBSEM (blue stars) and at least two more ventrally are possible. **(f)** Regions with clear somatic signals (blue stars) can be difficult to match due to tissue damage subsequent to LSM deforming the local arrangement of cell bodies (yellow arrow). **(g)** For ongoing quantification of registration and matching quality, ground truth somatic detections can be labeled or transformed cell body locations from co-registration can be proofread in CATMAID.

Methods and results contributed here allow for augmentation of wiring diagrams with activity or labeling markers in regions of good registration, subject to proofreading and the presence of fluorescent signal. In the absence of signal or somatic detection, interpretation is more nuanced. When the neighbors of a FIBSEM-determined cell body location are matched with fluorescing somata in LSM, the absence of signal for that cell can be verified. However for some indicators and markers, absence of signal does not necessarily imply negative indication; for example, markers may have variable expression, or in adult *Drosophila* some neurons are known to be electrotonically extensive so lack of somatic calcium indicator activity is not a guarantee of lack of dendritic activity [171]. This specific case is unlikely to apply to larval neurons due to their smaller spatial extent. When inaccurate or imprecise registration or poor LSM quality interfere with matching, there is conjunctive uncertainty from localization and ambiguity about a given locale's interpretation. These and other factors impacting the likelihood of augmenting a given neuron and interpretation of that result are modeled in Figure 5.1.

One mitigation for these uncertainties applicable to motor control in the VNC is redundancy in the data from stereotyped, repeating circuitry. Depending on the circuit of study, one may only need to identify a single hemisegment that jointly maximizes the quality of all imaging conditions. Alternatively, if activity dynamics are believed to be segmentally identical for propagating behaviors like peristaltic waves, representatives for each stereotyped cell type in a circuit can be pooled from wherever in the VNC a hemisegmental neuron of that type is reconstructable, identifiable between modalities, and has reliable LSM signal.

4.4.1 Future Directions

Mesh-based registration would be improved by jointly making use of the neuropil segmentation with the rind segmentation as a labeled point-cloud matching registration in samples where LSM is of sufficient quality for accurate neuropil segmentation. More generally, mesh-based registration could improve by removing the stochasticity and potential overfit problems of point sampling. The expectation maximization approach could operate directly from the distance transform of the mesh rather than re-estimation of density from the sample, or direct mesh-to-mesh methods as described in the background can be applied. None of the methods applied exploit image features of the multi-modal data. The existing methods can be used to create manually curated ground truth registration, which can be used to train inter-modal generative or similarity models, allowing the application of image-based registration inference methods. Unsupervised methods are also possible [172, 173].

Another approach would be to introduce fiducial markers into the sample. Beads in the sample embedding material can be used to register multiple cameras and acquired regions

in LSM [155, 174]. Because the embedding material is exchanged between modalities, this particular technique would not apply to multi-modal larval imaging, but it may instead be possible to affix markers onto the surface of the CNS. Fiducial markers that both do not interfere with LSM and remain attached to the sample through fixation, contrasting, embedding, and the many washes in between may be challenging to engineer.

Chapter 5

Augmenting Wiring Diagrams of VNC Circuits

To demonstrate the feasibility and circuit-targeted workflow of augmenting wiring diagrams, this chapter applies methods contributed by the previous chapters to neuronal populations in the larval *Drosophila* ventral nerve cord (VNC). Populations participating in motor circuitry described in Section 1.1 and subsection 2.1.2 are targeted, building a foundation for future work modeling motor coordination between antagonistic behaviors.

Feasibility encompasses two concerns: whether it is possible to augment wiring diagrams with this approach, and whether it is practical. This chapter addresses the latter. As concerns of possibility identified in previous chapters inform practice, they are summarized in the background below. The practical challenge to augmenting wiring diagrams is if, given these data quality and completeness issues, analysis of a circuit of interest in each augmentation animal can be performed with sufficient throughput and robustness to justify complexity of the process in comparison to alternative targeted experiments. Under this criteria, the critical question is how quickly and reliably circuits of interest can be identified in structural imaging of the per-augmentation animal, as this step requires the most time and is where most factors determining possibility converge.

To investigate this question, neurons in and adjacent to a neuroblast (NB) lineage bundle in the VNC were partially reconstructed in one activity indicator expressing animal and one neurotransmitter marker expressing animal. The process is representative of exploratory reconstruction to find neurons of interest that must be made efficient for augmentation, while allowing for developing new approaches to comparative connectomics. As it is not an aim of activity augmented wiring diagrams to fully reconstruct neuronal morphologies, only to establish identity, there are new approaches to neural circuit reconstruction to explore that jointly maximize certainty of identity while minimizing reconstructed cable by exploiting

dense reconstruction in a reference animal and replicated reconstruction across multiple animals.

5.1 Background

Successful augmentation of wiring diagrams, meaning observation of somatic signals in light sheet microscopy (LSM) (or absence thereof for some signals as discussed in Chapter 4) and accurate transitive identification of that signal's fluorescing neuron with the stereotyped neuron in the wiring diagram, requires overcoming several limitations and sources of error identified in previous chapters. These sources and their interactions are modeled in Figure 5.1 for the augmentation of each neuron independently. Estimating parameters of this model is ongoing work (e.g., estimation of reconstructability in Figure 3.8).

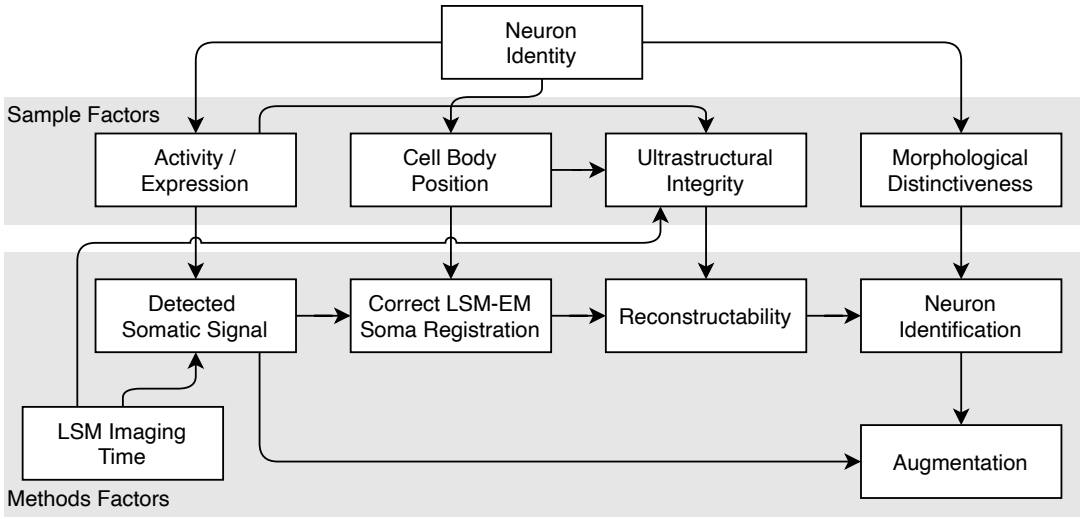

Fig. 5.1 Bayesian Network Model of Successful Wiring Diagram Augmentation. This conceptual probabilistic model summarizes the dependency structure of factors influencing the successful augmentation of the wiring diagram node *of a single neuron* with activity information or other fluorescent marker. Factors are broadly grouped into those drawn for each sample CNS, those determined by methods contributed by this thesis, and the intrinsic factor of neuronal identity in *Drosophila* neurobiology.

The probability of augmenting each neuron in a wiring diagram is not independent, as factors identified in this model have conditional dependence between neurons, especially spatially. For example, correct or corrected LSM-EM registration of one cell body will improve the matching of nearby cell bodies, while apoptosis of a cell can lead to tissue damage reducing the probability of successful reconstruction of many neighboring cells.

Some factors are necessarily conditioned on neuronal populations, such as morphological distinctiveness. However, this per-neuron model is useful both for focusing optimizations and future work for methods, and for designing circuit-targeted annotation and reconstruction strategies. This latter use is relevant to the aims of this chapter.

5.2 Methods

5.2.1 Datasets and Targeted Populations

Two first instar larvae, samples 1018 and 1128, were chosen for reconstruction. They represent an activity indicator and a neurotransmitter marker sample respectively, and are representative of the two FIBSEM apparatuses used and their influence on EM quality. Sample 1128 expresses a GABA marker; GABA is an inhibitory neurotransmitter whose identification in wiring diagrams greatly constrains them. Sample 1018 has the most extensive exploratory reconstruction to demonstrate feasibility (Figure 3.8), while sample 1128 has the best overall imaging quality and tissue condition of the samples (Figure 3.6)

Lineage 6 (NB5-2), entering the VNC neuropil [32] through a ventromedial bundle, was targeted for reconstruction in segment A1 in each larva. This lineage contains several neurons relevant to motor circuit modeling, including motor neuron MN-12, which recruits ventral longitudinal muscles in peristaltic behaviors [14], premotor neuron A05k, and multiple neurons upstream of A27k, which modulates phase offset of backward peristaltic muscle recruitment as described in subsection 2.1.2 [13]. All reconstruction was done through CATMAID as described in Chapter 3. Reconstruction in sample 1018 required a mixture of extension of existing reconstructions and de novo reconstruction, while sample 1128 had no prior annotation. Katharina Eichler, a neuroanatomical reconstruction expert, contributed to these reconstructions.

Reconstruction is seeded by projecting the target neuron set from the reference larva into the augmentation larva via previously created landmark registration (Figure 3.3). Lineage bundles entering the neuropil in that locus are identified and queued for exploratory reconstruction.

5.2.2 Optimizing Population Matching of Neuronal Morphology

Establishing morphological identity with as little reconstruction as possible is key both to efficiency for the practical feasibility of augmenting wiring diagrams and for overcoming unresolvable ultrastructure so that augmentation is possible. Morphological similarity metrics

such as NBLAST [118] can better determine probable identity when they are constrained to bipartite matching between sets of neurons (Figure 5.2).

For these reconstructions two levels of constrained processing of morphological metrics were applied. First, bipartite matching was continuously made between each of the three pairings of larva (i.e., all choices of the two FIBSEM samples and the reference), using the traditional Hungarian algorithm with extensions for non-square matrices [175, 176]. However, a matching does not provide a confidence metric. To both observe convergence in matching and to aid assessment of whether lineages or hemilineages are complete, the putative neuron set of interest was hierarchically clustered independently in each larva with the Natverse analysis toolkit in R [177]. For the reference larva, cluster thresholding was chosen to be 1.1 ($N = 7$), while for the augmentation larvae the threshold was adjusted to yield a similar number of clusters as the reference (sample 1018: $0.8, N = 7$; sample 1128: $0.55, N = 6$). A second bipartite matching is then applied to comparatively match these clusterings between larva. To do this, the count of the edges in the neuronal bipartite matching when clustered are summed and the weights of these inter-cluster edges are used for the objective matrix of the bipartite matching optimization.

Finally, the transitive or cyclic agreement of pairwise neuronal matchings is tracked. That is, if neuron A in sample 1018 is matched with neuron B in the reference larva, which is matched with neuron C in 1128, which is matched with neuron A in sample 1018, it may be an indicator of confidence in the pairwise identifications. A tripartite matching across all three larvae, or more generally n-matching hypergraphs across an arbitrary number of comparative connectomics datasets, should in theory yield a more optimal matching. However, given that tripartite matching is NP-hard, and the goal of these methods is to investigate when morphological matchings are convergent or what their confidence is, observing correspondences between the bipartite matchings is more informative.

5.3 Results

5.3.1 Comparative Connectomic Reconstruction of VNC Linage Bundles

In the initial seeding bundle in the reference larva, 38 morphologically similar cells were identified as belonging to or cofasciculating with lineage 6 (NB5-2). Using the landmark-projected bundle seeding strategy described above, initial candidates were identified in each augmentation volume within 30 min. 38 cells were reconstructed until only uncertain

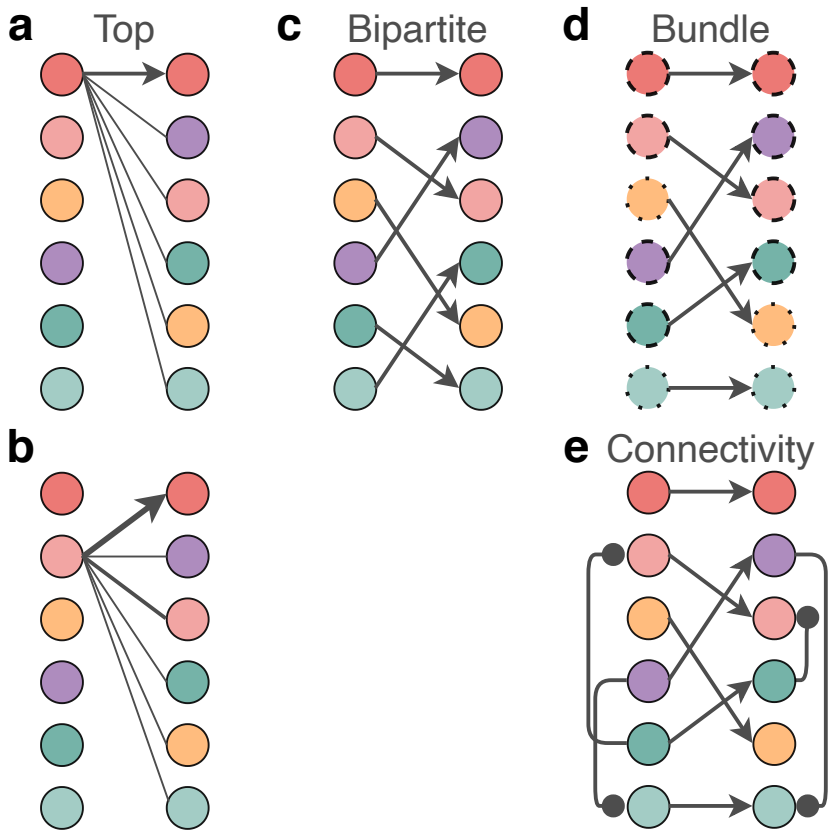

Fig. 5.2 Improving Morphological Matching with Constraints. **(a)** Morphological matching scores neurons (circles) based on similar morphological features. For organisms with stereotyped, identifiable neurons, this can be interpreted as a cell identity (color). For identifying a single neuron from a query set (left column) with a set of candidate matches (right column), scores for each can be considered (edge thickness) and the greatest can be chosen (arrow). **(b)** However, an incorrect match may individually have a better score. **(c)** When querying with sets, an optimal assignment that maximizes the sum score of the set can be chosen by bipartite matching. **(d)** Non-unique but coloring labels (dashed strokes), such as neurotransmitter identity, can further constrain and improve matching, even if they are soft, violable constraints like stereotyped bundle lineage entry that may developmentally vary. **(e)** Non-unary information can further constrain possible assignments, such as sets of neurons being assigned in ways that preserve the isomorphism of connections between them.

continuations remained in sample 1018 that also formed a cofasciculation. An ongoing reconstruction effort in sample 1128 has identified 13 candidates in the corresponding bundle of lineage 6 thus far, though not all have been exhaustively reconstructed. Combined, 9 off-target neurons were partially traced in the augmentation volumes but discarded, and 2 neuronal fragments in sample 1018 were filtered from results because they could not be eliminated as bundle candidates but were not reconstructable to either soma or substantial cable length. Total reconstruction time was 17.76 h in sample 1018 (not including existing exploratory reconstruction from Figure 3.8) and 2.85 h in sample 1128.

As shown in Figure 5.3, bipartite clustered morphological matching identifies some consistent lineage clusters even when bipartite neuronal matching is not unanimous. Transitively consistently identified neurons ($N = 2$) suggest likely stereotyped neuron types even when reconstructable cable length is short. The analysis that generates Figure 5.3b is an interactive tool that will be made available via CATMAID or a compatible environment to continually monitor and guide reconstruction.

Though less reconstruction exists for sample 1128, 1.76x speedup of reconstruction rates due to better imaging quality and tissue condition (5.8 µm/min, $N = 16; R^2 = 0.952$) is measured over sample 1018 (3.3 µm/min, $N = 42; R^2 = 0.867$). For comparison, in previous work I measured estimated cable reconstruction rate without synapse annotation in adult *Drosophila* ssTEM at 8 µm/min (subsection 3.2.6), but the length of cable needed for adequate reconstruction in adult *Drosophila* is far larger due to more spatially extensive arbors. Mean cable length is higher in sample 1128 than sample 1018 (60 µm and 26 µm respectively) despite reconstruction not being exhaustive.

5.4 Discussion

Stereotyped neuron lineages can be reconstructed in multiple larvae enabling augmentation with both activity indicators and neurotransmitter labelings. Rates and reliability of reconstruction are less than those of high-resolution electron microscopy volumes imaged exclusively for long-term mapping of wiring diagrams, but exploiting existing reconstruction through constrained morphological matching reduces the cable length needed for confident identification, reducing overall reconstruction time. Image quality and tissue condition significantly impact reconstruction rate and length of reconstructable cable, therefore improving the possibility and practicality of augmenting wiring diagrams.

Improved quality in structural imaging volumes will also enable the application of computer vision for segmentation-based reconstruction, which complements morphological matching-guided reconstruction. With sufficient reduction in tissue damage and improvement

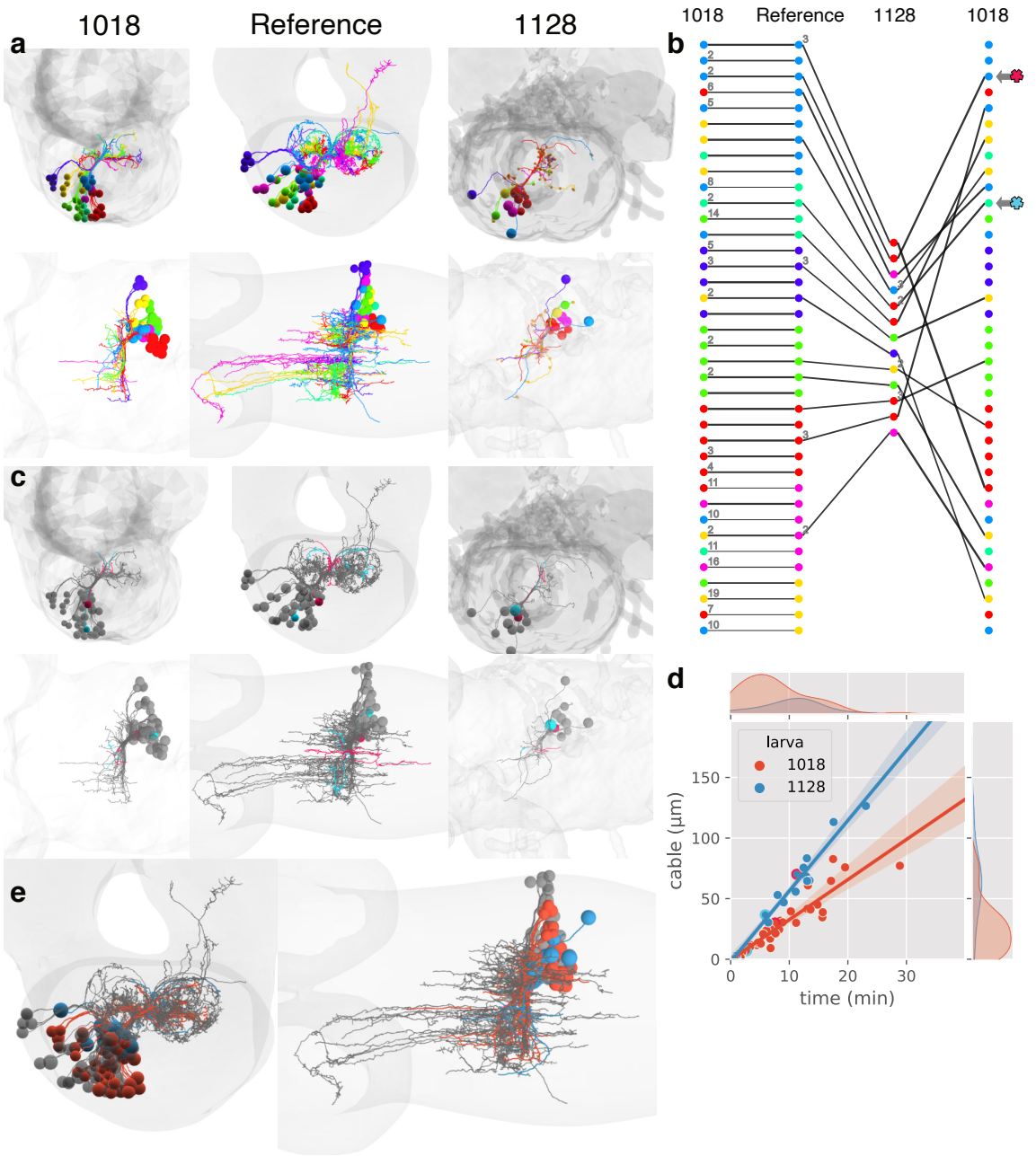

Fig. 5.3 Comparative Connectomic Reconstruction of Lineage 6 Bundle in Three *Drosophila* Larvae. **(a)** Lineage bundle reconstructions in two FIBSEM augmentation larvae and the reference first instar larva. Neurons are colored by inter-larvae morphologically-matched, intra-larva morphologically-clustered groups as described in the text. **(b)** Inter-larvae morphological matching of reconstructed cells. Colors are according to the same clusters as **(a)**. Numbers indicate the individual NBLAST score rank of the assigned match for that neuron when it is not 1. Gray arrows indicate transitive, cyclic matches between the three larvae. **(c)** Transitively matched neurons from **(b)**, colored matching the stars there. Non-matched neurons are in gray. **(d)** Kernel density and regression estimate of reconstruction time and cable for each FIBSEM augmentation larva. Summary statistics are given in the text. Points corresponding to neurons in **(c)** are stroked with those colors. **(e)** Complete reconstructions from both augmentation larvae projected into the reference larva over neurons there (gray). Larva colors are as in **(d)**.

in structural imaging quality, augmenting wiring diagrams with activity, neurotransmitter labels, or other fluorescent markers is feasible.

Chapter 6

Summary

Augmenting neural circuit wiring diagrams with activity and other information about neuron state and function aids in the creation of models that mechanistically explain behavior. Augmented wiring diagrams can extend the scope of connectomics-guided circuit modeling to larger and more complex neural systems coordinating multiple sensory modalities and behavioral outputs. The contributed methods of this thesis provide a template for augmenting the central nervous system wiring diagram of the *Drosophila* larva with activity, neurotransmitter, and arbitrary cell-specific marker labelings for multiple larvae, with reduced resource, time, and computational costs relative to the eight year, multi-group reconstruction of the reference larva. While the current results do not achieve the full extent of the aims of activity augmented wiring diagrams with respect to density of augmentation or robustness and speed of the process, the feasibility of each constituent method has been demonstrated. This work informs future methods to augment wiring diagrams, either by refinement of the contributed methods, both experimental and computational, or by substitution of constituent methods with alternatives discussed in Section 2.4.

6.1 Future Directions

Future directions for these methods fall into two scopes: improving the reliability of the contributed methods, and expanding the application of augmented wiring diagrams to other systems and questions.

The reliability of the current methods is predominantly limited by two factors: the fidelity of functional imaging to resolve densely packed somatic activity signals, and the integrity of ultrastructure in structural imaging following functional imaging. Quality of functional imaging can be improved by trading temporal resolution for spatial resolution, as activity-augmented wiring diagrams are valuable even if only co-activity of circuit elements

is observed without fast activity dynamics. Computationally, computer vision methods that generate deformation fields directly from functional imaging and electron microscopy to register them can also use structural information to better distinguish fluorescent signals, improving on the use of transformed electron microscopy nuclei masks employed here. To reduce tissue damage, investigating rates of apoptosis would allow evidence-based reduction of functional imaging time to optimize for ultrastructural integrity while maximizing observed function.

In *Drosophila* larva and other animals with stereotyped, individually identifiable neurons, augmented wiring diagrams enable not only inter-individual comparative connectomics, but also experimental connectomics by allowing observation of the functional perturbations induced by genetic interventions in a neural circuit, so long as primary neurite morphology is conserved. While more challenging, applications are also possible for animals without individually identifiable neurons. For example, in nervous systems with morphologically stereotyped neuronal types, such as adult *Drosophila*, wiring diagrams can still be augmented at the granularity of those types' populations. Though this may not identify individual neuronal connectivity with activity timeseries between animals, intra- and inter-type population activity is still informative in conjunction with their wiring diagram. Most such model organisms have nervous systems spatially larger than *Drosophila* larvae, so an extension of these methods would require alternative structural imaging approaches.

References

[1] D. W. Morton and H. J. Chiel. “Neural architectures for adaptive behavior”. In: *Trends in Neurosciences* 17.10 (Jan. 1, 1994), pp. 413–420. ISSN: 0166-2236.

[2] Kevin L. Briggman and William B. Kristan. “Imaging Dedicated and Multifunctional Neural Circuits Generating Distinct Behaviors”. In: *Journal of Neuroscience* 26.42 (Oct. 18, 2006), pp. 10925–10933. ISSN: 0270-6474, 1529-2401.

[3] Marta Zlatic, Matthias Landgraf, and Michael Bate. “Genetic specification of axonal arbors: atonal regulates robo3 to position terminal branches in the Drosophila nervous system”. In: *Neuron* 37.1 (2003), pp. 41–51.

[4] Tomoko Ohyama, Casey M. Schneider-Mizell, Richard D. Fetter, Javier Valdes Aleman, Romain Franconville, Marta Rivera-Alba, Brett D. Mensh, Kristin M. Branson, Julie H. Simpson, James W. Truman, Albert Cardona, and Marta Zlatic. “A multilevel multimodal circuit enhances action selection in Drosophila”. In: *Nature* 520.7549 (Apr. 2015), pp. 633–639. ISSN: 1476-4687.

[5] Barret D. Pfeiffer, Teri-T B. Ngo, Karen L. Hibbard, Christine Murphy, Arnim Jenett, James W. Truman, and Gerald M. Rubin. “Refinement of tools for targeted gene expression in Drosophila”. In: *Genetics* 186.2 (2010), pp. 735–755.

[6] Joshua T. Vogelstein, Youngser Park, Tomoko Ohyama, Rex A. Kerr, James W. Truman, Carey E. Priebe, and Marta Zlatic. “Discovery of brainwide neural-behavioral maps via multiscale unsupervised structure learning”. In: *Science* 344.6182 (2014), pp. 386–392.

[7] Stefan R. Pulver, Timothy G. Bayley, Adam L. Taylor, Jimena Berni, Michael Bate, and Berthold Hedwig. “Imaging fictive locomotor patterns in larval Drosophila”. In: *Journal of Neurophysiology* 114.5 (Aug. 26, 2015), pp. 2564–2577. ISSN: 0022-3077.

[8] David Berrigan and David J. Pepin. “How maggots move: Allometry and kinematics of crawling in larval Diptera”. In: *Journal of Insect Physiology* 41.4 (Apr. 1, 1995), pp. 329–337. ISSN: 0022-1910.

[9] Akira Fushiki, Maarten F Zwart, Hiroshi Kohsaka, Richard D Fetter, Albert Cardona, and Akinao Nose. “A circuit mechanism for the propagation of waves of muscle contraction in Drosophila”. In: *eLife* 5 (Feb. 15, 2016). Ed. by Leslie C Griffith, e13253. ISSN: 2050-084X.

[10] Eri Hasegawa, James W. Truman, and Akinao Nose. “Identification of excitatory premotor interneurons which regulate local muscle contraction during Drosophila larval locomotion”. In: *Scientific Reports* 6.1 (July 29, 2016), p. 30806. ISSN: 2045-2322.

[11] Arnaldo Carreira-Rosario, Aref Arzan Zarin, Matthew Q Clark, Laurina Manning, Richard D Fetter, Albert Cardona, and Chris Q Doe. "MDN brain descending neurons coordinately activate backward and inhibit forward locomotion". In: *eLife* 7 (Aug. 2, 2018). Ed. by Ronald L Calabrese and Eve Marder, e38554. ISSN: 2050-084X.

[12] Ellie S. Heckscher, Shawn R. Lockery, and Chris Q. Doe. "Characterization of Drosophila Larval Crawling at the Level of Organism, Segment, and Somatic Body Wall Musculature". In: *Journal of Neuroscience* 32.36 (Sept. 5, 2012), pp. 12460–12471. ISSN: 0270-6474, 1529-2401.

[13] Hiroshi Kohsaka, Maarten F. Zwart, Akira Fushiki, Richard D. Fetter, James W. Truman, Albert Cardona, and Akinao Nose. "Regulation of forward and backward locomotion through intersegmental feedback circuits in Drosophila larvae". In: *Nature Communications* 10.1 (June 14, 2019), p. 2654. ISSN: 2041-1723.

[14] Aref Arzan Zarin, Brandon Mark, Albert Cardona, Ashok Litwin-Kumar, and Chris Q Doe. "A multilayer circuit architecture for the generation of distinct locomotor behaviors in Drosophila". In: *eLife* 8 (Dec. 23, 2019). Ed. by Kristin Scott and Ronald L Calabrese, e51781. ISSN: 2050-084X.

[15] Irving E. Wang and Thomas R. Clandinin. "The Influence of Wiring Economy on Nervous System Evolution". In: *Current Biology* 26.20 (Oct. 24, 2016), R1101–R1108. ISSN: 0960-9822.

[16] Cynthia L. Hughes and John B. Thomas. "A sensory feedback circuit coordinates muscle activity in Drosophila". In: *Molecular and Cellular Neuroscience* 35.2 (2007), pp. 383–396.

[17] Julijana Gjorgjieva, Jimena Berni, Jan Felix Evers, and Stephen J Eglen. "Neural circuits for peristaltic wave propagation in crawling Drosophila larvae: analysis and modeling". In: *Frontiers in Computational Neuroscience* 7 (2013).

[18] Winfried Denk, Kevin L. Briggman, and Moritz Helmstaedter. "Structural neurobiology: missing link to a mechanistic understanding of neural computation". In: *Nature Reviews Neuroscience* 13.5 (2012), pp. 351–358.

[19] Eve Marder and Dirk Bucher. "Understanding circuit dynamics using the stomatogastric nervous system of lobsters and crabs". In: *Annu. Rev. Physiol.* 69 (2007), pp. 291–316.

[20] Davi D. Bock, Wei-Chung Allen Lee, Aaron M. Kerlin, Mark L. Andermann, Greg Hood, Arthur W. Wetzel, Sergey Yurgenson, Edward R. Soucy, Hyon Suk Kim, and R. Clay Reid. "Network anatomy and in vivo physiology of visual cortical neurons". In: *Nature* 471.7337 (Mar. 2011), pp. 177–182. ISSN: 1476-4687.

[21] William C. Lemon, Stefan R. Pulver, Burkhard Höckendorf, Katie McDole, Kristin Branson, Jeremy Freeman, and Philipp J. Keller. "Whole-central nervous system functional imaging in larval Drosophila". In: *Nature Communications* 6.1 (Aug. 11, 2015), p. 7924. ISSN: 2041-1723.

[22] Tsai-Wen Chen, Trevor J. Wardill, Yi Sun, Stefan R. Pulver, Sabine L. Renninger, Amy Baohan, Eric R. Schreiter, Rex A. Kerr, Michael B. Orger, Vivek Jayaraman, Loren L. Looger, Karel Svoboda, and Douglas S. Kim. "Ultrasensitive fluorescent proteins for imaging neuronal activity". In: *Nature* 499.7458 (July 2013), pp. 295–300. ISSN: 1476-4687.

[23] Hod Dana, Boaz Mohar, Yi Sun, Sujatha Narayan, Andrew Gordus, Jeremy P Hasseman, Getahun Tsegaye, Graham T Holt, Amy Hu, Deepika Walpita, Ronak Patel, John J Macklin, Cornelia I Bargmann, Misha B Ahrens, Eric R Schreiter, Vivek Jayaraman, Loren L Looger, Karel Svoboda, and Douglas S Kim. "Sensitive red protein calcium indicators for imaging neural activity". In: *eLife* 5 (Mar. 24, 2016). Ed. by Michael Häusser, e12727. ISSN: 2050-084X.

[24] Raghav K. Chhetri, Fernando Amat, Yinan Wan, Burkhard Höckendorf, William C. Lemon, and Philipp J. Keller. "Whole-animal functional and developmental imaging with isotropic spatial resolution". In: *Nature Methods* 12.12 (2015), pp. 1171–1178.

[25] Nathan C. Klapoetke, Yasunobu Murata, Sung Soo Kim, Stefan R. Pulver, Amanda Birdsey-Benson, Yong Ku Cho, Tania K. Morimoto, Amy S. Chuong, Eric J. Carpenter, Zhijian Tian, Jun Wang, Yinlong Xie, Zhixiang Yan, Yong Zhang, Brian Y. Chow, Barbara Surek, Michael Melkonian, Vivek Jayaraman, Martha Constantine-Paton, Gane Ka-Shu Wong, and Edward S. Boyden. "Independent optical excitation of distinct neural populations". In: *Nature Methods* 11.3 (Mar. 2014), pp. 338–346. ISSN: 1548-7105.

[26] C. Shan Xu, Kenneth J. Hayworth, Zhiyuan Lu, Patricia Grob, Ahmed M. Hassan, José G. García-Cerdán, Krishna K. Niyogi, Eva Nogales, Richard J. Weinberg, and Harald F. Hess. "Enhanced FIB-SEM systems for large-volume 3D imaging". In: *eLife* 6 (2017), e25916.

[27] Tihana Jovanic, Casey Martin Schneider-Mizell, Mei Shao, Jean-Baptiste Masson, Gennady Denisov, Richard Doty Fetter, Brett Daren Mensh, James William Truman, Albert Cardona, and Marta Zlatic. "Competitive Disinhibition Mediates Behavioral Choice and Sequences in Drosophila". In: *Cell* 167.3 (Oct. 20, 2016), 858–870.e19. ISSN: 0092-8674.

[28] Stephan Gerhard, Ingrid Andrade, Richard D. Fetter, Albert Cardona, and Casey M. Schneider-Mizell. "Conserved neural circuit structure across Drosophila larva development revealed by comparative connectomics". In: *bioRxiv* (2017), p. 143727.

[29] Kei Ito, Joachim Urban, and Gerhard Technau. "Distribution, classification, and development of Drosophila glial cells in the late embryonic and early larval ventral nerve cord". In: *Development Genes and Evolution* 204 (May 1, 1995), pp. 284–307.

[30] Wesley B. Grueber, Bing Ye, Chung-Hui Yang, Susan Younger, Kelly Borden, Lily Y. Jan, and Yuh-Nung Jan. "Projections of Drosophila multidendritic neurons in the central nervous system: links with peripheral dendrite morphology". In: *Development* 134.1 (Jan. 1, 2007), pp. 55–64. ISSN: 0950-1991, 1477-9129.

[31] Michael D. Kim, Yuhui Wen, and Yuh-Nung Jan. "Patterning and organization of motor neuron dendrites in the Drosophila larva". In: *Developmental Biology* 336.2 (Dec. 15, 2009), pp. 213–221. ISSN: 0012-1606.

[32] Haluk Lacin and James W Truman. "Lineage mapping identifies molecular and architectural similarities between the larval and adult Drosophila central nervous system". In: *eLife* 5 (Mar. 25, 2016). ISSN: 2050-084X.

[33] Matthias Landgraf, Torsten Bossing, Gerd M. Technau, and Michael Bate. "The Origin, Location, and Projections of the Embryonic Abdominal Motorneurons of Drosophila". In: *Journal of Neuroscience* 17.24 (Dec. 15, 1997), pp. 9642–9655. ISSN: 0270-6474, 1529-2401.

[34] M. Bate. “The embryonic development of larval muscles in Drosophila”. In: *Development* 110.3 (Nov. 1, 1990), pp. 791–804. ISSN: 0950-1991, 1477-9129.

[35] Matthias Landgraf, Victoria Jeffrey, Miki Fujioka, James B. Jaynes, and Michael Bate. “Embryonic Origins of a Motor System: Motor Dendrites Form a Myotopic Map in Drosophila”. In: *PLOS Biology* 1.2 (Nov. 17, 2003), e41. ISSN: 1545-7885.

[36] Alex Mauss, Marco Tripodi, Jan Felix Evers, and Matthias Landgraf. “Midline Signalling Systems Direct the Formation of a Neural Map by Dendritic Targeting in the Drosophila Motor System”. In: *PLOS Biology* 7.9 (Sept. 22, 2009), e1000200. ISSN: 1545-7885.

[37] Marla B. Sokolowski, Clement Kent, and Jonathan Wong. “Drosophila larval foraging behaviour: Developmental stages”. In: *Animal Behaviour* 32.3 (Aug. 1, 1984), pp. 645–651. ISSN: 0003-3472.

[38] Richard Y. Hwang, Lixian Zhong, Yifan Xu, Trevor Johnson, Feng Zhang, Karl Deisseroth, and W. Daniel Tracey. “Nociceptive Neurons Protect Drosophila Larvae from Parasitoid Wasps”. In: *Current Biology* 17.24 (Dec. 18, 2007), pp. 2105–2116. ISSN: 0960-9822.

[39] Zachary Durisko, Rebecca Kemp, Rameeshay Mubasher, and Reuven Dukas. “Dynamics of Social Behavior in Fruit Fly Larvae”. In: *PLOS ONE* 9.4 (Apr. 16, 2014), e95495. ISSN: 1932-6203.

[40] Mark Dombrovski, Leanne Poussard, Kamilia Moalem, Lucia Kmecova, Nic Hogan, Elisabeth Schott, Andrea Vaccari, Scott Acton, and Barry Condron. “Cooperative Behavior Emerges among Drosophila Larvae”. In: *Current Biology* 27.18 (Sept. 25, 2017), 2821–2826.e2. ISSN: 0960-9822.

[41] Albert Cardona, Camilla Larsen, and Volker Hartenstein. “Neuronal fiber tracts connecting the brain and ventral nerve cord of the early Drosophila larva”. In: *Journal of Comparative Neurology* 515.4 (2009), pp. 427–440. ISSN: 1096-9861.

[42] Christoph Melcher and Michael J. Pankratz. “Candidate Gustatory Interneurons Modulating Feeding Behavior in the Drosophila Brain”. In: *PLOS Biology* 3.9 (Aug. 30, 2005), e305. ISSN: 1545-7885.

[43] Matthew E Berck, Avinash Khandelwal, Lindsey Claus, Luis Hernandez-Nunez, Guangwei Si, Christopher J Tabone, Feng Li, James W Truman, Rick D Fetter, Matthieu Louis, Aravinthan DT Samuel, and Albert Cardona. “The wiring diagram of a glomerular olfactory system”. In: *eLife* 5 (May 13, 2016). Ed. by Ronald L Calabrese, e14859. ISSN: 2050-084X.

[44] Chun Hu, Meike Petersen, Nina Hoyer, Bettina Spitzweck, Federico Tenedini, Denan Wang, Alisa Gruschka, Lara S. Burchardt, Emanuela Szpotowicz, Michaela Schweizer, Ananya R. Guntur, Chung-Hui Yang, and Peter Soba. “Sensory integration and neuromodulatory feedback facilitate Drosophila mechanonociceptive behavior”. In: *Nature Neuroscience* 20.8 (Aug. 2017), pp. 1085–1095. ISSN: 1546-1726.

[45] Katharina Eichler, Feng Li, Ashok Litwin-Kumar, Youngser Park, Ingrid Andrade, Casey M. Schneider-Mizell, Timo Saumweber, Annina Huser, Claire Eschbach, Bertram Gerber, Richard D. Fetter, James W. Truman, Carey E. Priebe, L. F. Abbott, Andreas S. Thum, Marta Zlatic, and Albert Cardona. "The complete connectome of a learning and memory centre in an insect brain". In: *Nature* 548.7666 (Aug. 2017), pp. 175–182. ISSN: 1476-4687.

[46] Jimena Berni, Stefan R. Pulver, Leslie C. Griffith, and Michael Bate. "Autonomous Circuitry for Substrate Exploration in Freely Moving Drosophila Larvae". In: *Current Biology* 22.20 (Oct. 23, 2012), pp. 1861–1870. ISSN: 0960-9822.

[47] Anita Burgos, Ken Honjo, Tomoko Ohyama, Cheng Sam Qian, Grace Ji-eun Shin, Daryl M Gohl, Marion Silies, W Daniel Tracey, Marta Zlatic, Albert Cardona, and Wesley B Grueber. "Nociceptive interneurons control modular motor pathways to promote escape behavior in Drosophila". In: *eLife* 7 (Mar. 12, 2018). Ed. by David D Ginty, e26016. ISSN: 2050-084X.

[48] Anthony M. Zador, Joshua Dubnau, Hassana K. Oyibo, Huiqing Zhan, Gang Cao, and Ian D. Peikon. "Sequencing the Connectome". In: *PLOS Biology* 10.10 (Oct. 23, 2012), e1001411. ISSN: 1545-7885.

[49] Young-Gyu Yoon, Peilun Dai, Jeremy Wohlwend, Jae-Byum Chang, Adam H. Marblestone, and Edward S. Boyden. "Feasibility of 3D Reconstruction of Neural Morphology Using Expansion Microscopy and Barcode-Guided Agglomeration". In: *Frontiers in Computational Neuroscience* 11 (2017). ISSN: 1662-5188.

[50] Jeff W. Lichtman, Jean Livet, and Joshua R. Sanes. "A technicolour approach to the connectome". In: *Nature Reviews Neuroscience* 9.6 (June 2008), pp. 417–422. ISSN: 1471-0048.

[51] Kevin L Briggman and Winfried Denk. "Towards neural circuit reconstruction with volume electron microscopy techniques". In: *Current Opinion in Neurobiology*. Neuronal and glial cell biology / New technologies 16.5 (Oct. 1, 2006), pp. 562–570. ISSN: 0959-4388.

[52] J. G. White, Eileen Southgate, J. N. Thomson, and S. Brenner. "The Structure of the Ventral Nerve Cord of Caenorhabditis elegans". In: *Philosophical Transactions of the Royal Society of London. Series B, Biological Sciences* 275.938 (1976), pp. 327–348. ISSN: 0080-4622.

[53] Steven J. Cook, Travis A. Jarrell, Christopher A. Brittin, Yi Wang, Adam E. Bloniarz, Maksim A. Yakovlev, Ken C. Q. Nguyen, Leo T.-H. Tang, Emily A. Bayer, Janet S. Duerr, Hannes E. Bülow, Oliver Hobert, David H. Hall, and Scott W. Emmons. "Whole-animal connectomes of both Caenorhabditis elegans sexes". In: *Nature* 571.7763 (July 2019), pp. 63–71. ISSN: 1476-4687.

[54] Daniel Witvliet, Ben Mulcahy, James K. Mitchell, Yaron Meirovitch, Daniel R. Berger, Yuelong Wu, Yufang Liu, Wan Xian Koh, Rajeev Parvathala, Douglas Holmyard, Richard L. Schalek, Nir Shavit, Andrew D. Chisholm, Jeff W. Lichtman, Aravinthan D. T. Samuel, and Mei Zhen. "Connectomes across development reveal principles of brain maturation in C. elegans". In: *bioRxiv* (May 22, 2020), p. 2020.04.30.066209.

[55] Kerrianne Ryan, Zhiyuan Lu, and Ian A Meinertzhagen. "The CNS connectome of a tadpole larva of Ciona intestinalis (L.) highlights sidedness in the brain of a chordate sibling". In: *eLife* 5 (Dec. 6, 2016). Ed. by Eve Marder, e16962. ISSN: 2050-084X.

[56] Csaba Verasztó, Sanja Jasek, Martin Gühmann, Réza Shahidi, Nobuo Ueda, James David Beard, Sara Mendes, Konrad Heinz, Luis Alberto Bezares-Calderón, Elizabeth Williams, and Gáspár Jékely. "Whole-animal connectome and cell-type complement of the three-segmented Platynereis dumerilii larva". In: *bioRxiv* (Aug. 23, 2020), p. 2020.08.21.260984.

[57] Zhihao Zheng, J. Scott Lauritzen, Eric Perlman, Camenzind G. Robinson, Matthew Nichols, Daniel Milkie, Omar Torrens, John Price, Corey B. Fisher, Nadiya Sharifi, Steven A. Calle-Schuler, Lucia Kmecova, Iqbal J. Ali, Bill Karsh, Eric T. Trautman, John A. Bogovic, Philipp Hanslovsky, Gregory S. X. E. Jefferis, Michael Kazhdan, Khaled Khairy, Stephan Saalfeld, Richard D. Fetter, and Davi D. Bock. "A Complete Electron Microscopy Volume of the Brain of Adult Drosophila melanogaster". In: *Cell* 174.3 (July 26, 2018), 730–743.e22. ISSN: 0092-8674, 1097-4172.

[58] Jasper T. Maniates-Selvin, David Grant Colburn Hildebrand, Brett J. Graham, Aaron T. Kuan, Logan A. Thomas, Tri Nguyen, Julia Buhmann, Anthony W. Azevedo, Brendan L. Shanny, Jan Funke, John C. Tuthill, and Wei-Chung Allen Lee. "Reconstruction of motor control circuits in adult Drosophila using automated transmission electron microscopy". In: *bioRxiv* (Jan. 11, 2020), p. 2020.01.10.902478.

[59] C. Shan Xu et al. "A Connectome of the Adult Drosophila Central Brain". In: *bioRxiv* (Jan. 21, 2020), p. 2020.01.21.911859.

[60] David Grant Colburn Hildebrand, Marcelo Cicconet, Russel Miguel Torres, Woohyuk Choi, Tran Minh Quan, Jungmin Moon, Arthur Willis Wetzel, Andrew Scott Champion, Brett Jesse Graham, Owen Randlett, George Scott Plummer, Ruben Portugues, Isaac Henry Bianco, Stephan Saalfeld, Alexander David Baden, Kunal Lillaney, Randal Burns, Joshua Tzvi Vogelstein, Alexander Franz Schier, Wei-Chung Allen Lee, Won-Ki Jeong, Jeff William Lichtman, and Florian Engert. "Whole-brain serial-section electron microscopy in larval zebrafish". In: *Nature* 545.7654 (May 2017), pp. 345–349. ISSN: 1476-4687.

[61] Sven Dorkenwald, Philipp J. Schubert, Marius F. Killinger, Gregor Urban, Shawn Mikula, Fabian Svara, and Joergen Kornfeld. "Automated synaptic connectivity inference for volume electron microscopy". In: *Nature Methods* 14.4 (Apr. 2017), pp. 435–442. ISSN: 1548-7105.

[62] Nicholas L. Turner et al. "Multiscale and multimodal reconstruction of cortical structure and function". In: *bioRxiv* (Oct. 24, 2020), p. 2020.10.14.338681.

[63] Kevin L Briggman and Davi D Bock. "Volume electron microscopy for neuronal circuit reconstruction". In: *Current Opinion in Neurobiology*. Neurotechnology 22.1 (Feb. 1, 2012), pp. 154–161. ISSN: 0959-4388.

[64] R. Schalek, N. Kasthuri, K. Hayworth, D. Berger, J. Tapia, J. Morgan, S. Turaga, E. Fagerholm, H. Seung, and J. Lichtman. "Development of High-Throughput, High-Resolution 3D Reconstruction of Large-Volume Biological Tissue Using Automated Tape Collection Ultramicrotomy and Scanning Electron Microscopy". In: *Microscopy and Microanalysis* 17 (S2 July 2011), pp. 966–967. ISSN: 1435-8115, 1431-9276.

[65] Wenjing Yin, Derrick Brittain, Jay Borseth, Marie E. Scott, Derric Williams, Jedediah Perkins, Christopher S. Own, Matthew Murfitt, Russel M. Torres, Daniel Kapner, Gayathri Mahalingam, Adam Bleckert, Daniel Castelli, David Reid, Wei-Chung Allen Lee, Brett J. Graham, Marc Takeno, Daniel J. Bumbarger, Colin Farrell, R. Clay Reid, and Nuno Macarico da Costa. "A petascale automated imaging pipeline for mapping neuronal circuits with high-throughput transmission electron microscopy". In: *Nature Communications* 11.1 (Oct. 2, 2020), p. 4949. ISSN: 2041-1723.

[66] Winfried Denk and Heinz Horstmann. "Serial Block-Face Scanning Electron Microscopy to Reconstruct Three-Dimensional Tissue Nanostructure". In: *PLOS Biology* 2.11 (Oct. 19, 2004), e329. ISSN: 1545-7885.

[67] Graham Knott, Herschel Marchman, David Wall, and Ben Lich. "Serial Section Scanning Electron Microscopy of Adult Brain Tissue Using Focused Ion Beam Milling". In: *Journal of Neuroscience* 28.12 (Mar. 19, 2008), pp. 2959–2964. ISSN: 0270-6474, 1529-2401.

[68] C. Shan Xu, Song Pang, Kenneth J. Hayworth, and Harald F. Hess. "Enabling FIB-SEM Systems for Large Volume Connectomics and Cell Biology". In: *bioRxiv* (Nov. 25, 2019), p. 852863.

[69] Anna Lena Eberle and Dirk Zeidler. "Multi-Beam Scanning Electron Microscopy for High-Throughput Imaging in Connectomics Research". In: *Frontiers in Neuroanatomy* 12 (2018). ISSN: 1662-5129.

[70] Kenneth J. Hayworth, David Peale, Michał Januszewski, Graham W. Knott, Zhiyuan Lu, C. Shan Xu, and Harald F. Hess. "Gas cluster ion beam SEM for imaging of large tissue samples with 10 nm isotropic resolution". In: *Nature Methods* 17.1 (Jan. 2020), pp. 68–71. ISSN: 1548-7105.

[71] *MICCAI challenge on circuit reconstruction from electron microscopy images (CREMI)*. URL: https://cremi.org/.

[72] V. Jain, J. F. Murray, F. Roth, S. Turaga, V. Zhigulin, K. L. Briggman, M. N. Helmstaedter, W. Denk, and H. S. Seung. "Supervised Learning of Image Restoration with Convolutional Networks". In: *2007 IEEE 11th International Conference on Computer Vision*. 2007 IEEE 11th International Conference on Computer Vision. ISSN: 2380-7504. Oct. 2007, pp. 1–8. DOI: 10.1109/ICCV.2007.4408909.

[73] Björn Andres, Ullrich Köthe, Moritz Helmstaedter, Winfried Denk, and Fred A. Hamprecht. "Segmentation of SBFSEM Volume Data of Neural Tissue by Hierarchical Classification". In: *Pattern Recognition*. Ed. by Gerhard Rigoll. Lecture Notes in Computer Science. Berlin, Heidelberg: Springer, 2008, pp. 142–152. ISBN: 978-3-540-69321-5. DOI: 10.1007/978-3-540-69321-5_15.

[74] Jakob H. Macke, Nina Maack, Rocky Gupta, Winfried Denk, Bernhard Schölkopf, and Alexander Borst. "Contour-propagation algorithms for semi-automated reconstruction of neural processes". In: *Journal of Neuroscience Methods* 167.2 (Jan. 30, 2008), pp. 349–357. ISSN: 0165-0270.

[75] Srinivas C. Turaga, Joseph F. Murray, Viren Jain, Fabian Roth, Moritz Helmstaedter, Kevin Briggman, Winfried Denk, and H. Sebastian Seung. "Convolutional networks can learn to generate affinity graphs for image segmentation". In: *Neural Computation* 22.2 (Feb. 2010), pp. 511–538. ISSN: 1530-888X.

[76] Kevin Briggman, Winfried Denk, Sebastian Seung, Moritz Helmstaedter, and Srinivas C. Turaga. "Maximin affinity learning of image segmentation". In: *Advances in Neural Information Processing Systems* 22 (2009), pp. 1865–1873.

[77] Viren Jain, Srinivas C. Turaga, K. Briggman, Moritz Helmstaedter, Winfried Denk, and H. Seung. "Learning to Agglomerate Superpixel Hierarchies". In: *Advances in Neural Information Processing Systems* 24 (2011), pp. 648–656.

[78] Thorsten Beier, Constantin Pape, Nasim Rahaman, Timo Prange, Stuart Berg, Davi D. Bock, Albert Cardona, Graham W. Knott, Stephen M. Plaza, Louis K. Scheffer, Ullrich Koethe, Anna Kreshuk, and Fred A. Hamprecht. "Multicut brings automated neurite segmentation closer to human performance". In: *Nature Methods* 14.2 (Feb. 2017), pp. 101–102. ISSN: 1548-7105.

[79] J. Funke, F. Tschopp, W. Grisaitis, A. Sheridan, C. Singh, S. Saalfeld, and S. C. Turaga. "Large Scale Image Segmentation with Structured Loss Based Deep Learning for Connectome Reconstruction". In: *IEEE Transactions on Pattern Analysis and Machine Intelligence* 41.7 (July 2019), pp. 1669–1680. ISSN: 1939-3539.

[80] Michał Januszewski, Jörgen Kornfeld, Peter H. Li, Art Pope, Tim Blakely, Larry Lindsey, Jeremy Maitin-Shepard, Mike Tyka, Winfried Denk, and Viren Jain. "High-precision automated reconstruction of neurons with flood-filling networks". In: *Nature Methods* 15.8 (Aug. 2018), pp. 605–610. ISSN: 1548-7105.

[81] Junichi Nakai, Masamichi Ohkura, and Keiji Imoto. "A high signal-to-noise Ca 2+ probe composed of a single green fluorescent protein". In: *Nature Biotechnology* 19.2 (Feb. 2001), pp. 137–141. ISSN: 1546-1696.

[82] Lin Tian, S. Andrew Hires, Tianyi Mao, Daniel Huber, M. Eugenia Chiappe, Sreekanth H. Chalasani, Leopoldo Petreanu, Jasper Akerboom, Sean A. McKinney, Eric R. Schreiter, Cornelia I. Bargmann, Vivek Jayaraman, Karel Svoboda, and Loren L. Looger. "Imaging neural activity in worms, flies and mice with improved GCaMP calcium indicators". In: *Nature methods* 6.12 (Dec. 2009), pp. 875–881. ISSN: 1548-7091.

[83] Jelena Platisa and Vincent A. Pieribone. "Genetically encoded fluorescent voltage indicators: are we there yet?" In: *Current opinion in neurobiology* 50 (June 2018), pp. 146–153. ISSN: 0959-4388.

[84] Hod Dana, Tsai-Wen Chen, Amy Hu, Brenda C. Shields, Caiying Guo, Loren L. Looger, Douglas S. Kim, and Karel Svoboda. "Thy1-GCaMP6 Transgenic Mice for Neuronal Population Imaging In Vivo". In: *PLOS ONE* 9.9 (Sept. 24, 2014), e108697. ISSN: 1932-6203.

[85] Jan Huisken, Jim Swoger, Filippo Del Bene, Joachim Wittbrodt, and Ernst H. K. Stelzer. "Optical Sectioning Deep Inside Live Embryos by Selective Plane Illumination Microscopy". In: *Science* 305.5686 (Aug. 13, 2004), pp. 1007–1009. ISSN: 0036-8075, 1095-9203.

[86] Philipp J. Keller, Annette D. Schmidt, Joachim Wittbrodt, and Ernst H. K. Stelzer. "Reconstruction of Zebrafish Early Embryonic Development by Scanned Light Sheet Microscopy". In: *Science* 322.5904 (Nov. 14, 2008), pp. 1065–1069. ISSN: 0036-8075, 1095-9203.

[87] Raju Tomer, Khaled Khairy, Fernando Amat, and Philipp J. Keller. "Quantitative high-speed imaging of entire developing embryos with simultaneous multiview light-sheet microscopy". In: *Nature Methods* 9.7 (July 2012), pp. 755–763. ISSN: 1548-7105.

[88] Misha B. Ahrens, Michael B. Orger, Drew N. Robson, Jennifer M. Li, and Philipp J. Keller. "Whole-brain functional imaging at cellular resolution using light-sheet microscopy". In: *Nature Methods* 10.5 (May 2013), pp. 413–420. ISSN: 1548-7105.

[89] Nikita Vladimirov, Chen Wang, Burkhard Höckendorf, Avinash Pujala, Masashi Tanimoto, Yu Mu, Chao-Tsung Yang, Jason D. Wittenbach, Jeremy Freeman, Stephan Preibisch, Minoru Koyama, Philipp J. Keller, and Misha B. Ahrens. "Brain-wide circuit interrogation at the cellular level guided by online analysis of neuronal function". In: *Nature Methods* 15.12 (Dec. 2018), pp. 1117–1125. ISSN: 1548-7105.

[90] Deniz Atasoy, J. Nicholas Betley, Wei-Ping Li, Helen H. Su, Sinem M. Sertel, Louis K. Scheffer, Julie H. Simpson, Richard D. Fetter, and Scott M. Sternson. "A genetically specified connectomics approach applied to long-range feeding regulatory circuits". In: *Nature Neuroscience* 17.12 (Dec. 2014), pp. 1830–1839. ISSN: 1546-1726.

[91] Julian Ng, Alyssa Browning, Lorenz Lechner, Masako Terada, Gillian Howard, and Gregory S. X. E. Jefferis. "Genetically targeted 3D visualisation of Drosophila neurons under Electron Microscopy and X-Ray Microscopy using miniSOG". In: *Scientific Reports* 6.1 (Dec. 13, 2016), p. 38863. ISSN: 2045-2322.

[92] Réza Shahidi, Elizabeth A Williams, Markus Conzelmann, Albina Asadulina, Csaba Verasztó, Sanja Jasek, Luis A Bezares-Calderón, and Gáspár Jékely. "A serial multiplex immunogold labeling method for identifying peptidergic neurons in connectomes". In: *eLife* 4 (Dec. 15, 2015). Ed. by Ronald L Calabrese, e11147. ISSN: 2050-084X.

[93] Stephen R. Adams, Mason R. Mackey, Ranjan Ramachandra, Sakina F. Palida Lemieux, Paul Steinbach, Eric A. Bushong, Margaret T. Butko, Ben N. G. Giepmans, Mark H. Ellisman, and Roger Y. Tsien. "Multicolor Electron Microscopy for Simultaneous Visualization of Multiple Molecular Species". In: *Cell Chemical Biology* 23.11 (Nov. 17, 2016), pp. 1417–1427. ISSN: 2451-9456.

[94] Benjamin F. Fosque, Yi Sun, Hod Dana, Chao-Tsung Yang, Tomoko Ohyama, Michael R. Tadross, Ronak Patel, Marta Zlatic, Douglas S. Kim, Misha B. Ahrens, Vivek Jayaraman, Loren L. Looger, and Eric R. Schreiter. "Labeling of active neural circuits in vivo with designed calcium integrators". In: *Science* 347.6223 (Feb. 13, 2015), pp. 755–760. ISSN: 0036-8075, 1095-9203.

[95] Nils Eckstein, Alexander S. Bates, Michelle Du, Volker Hartenstein, Gregory S. X. E. Jefferis, and Jan Funke. "Neurotransmitter Classification from Electron Microscopy Images at Synaptic Sites in Drosophila". In: *bioRxiv* (Sept. 2, 2020).

[96] Emmanouil D Karagiannis and Edward S Boyden. "Expansion microscopy: development and neuroscience applications". In: *Current Opinion in Neurobiology*. Neurotechnologies 50 (June 1, 2018), pp. 56–63. ISSN: 0959-4388.

[97] Chih-Chieh (Jay) Yu, Nicholas C Barry, Asmamaw T Wassie, Anubhav Sinha, Abhishek Bhattacharya, Shoh Asano, Chi Zhang, Fei Chen, Oliver Hobert, Miriam B Goodman, Gal Haspel, and Edward S Boyden. "Expansion microscopy of C. elegans". In: *eLife* 9 (May 1, 2020). Ed. by Abby F Dernburg and David Ron, e46249. ISSN: 2050-084X.

[98] Tatsuya C. Murakami, Tomoyuki Mano, Shu Saikawa, Shuhei A. Horiguchi, Daichi Shigeta, Kousuke Baba, Hiroshi Sekiya, Yoshihiro Shimizu, Kenji F. Tanaka, Hiroshi Kiyonari, Masamitsu Iino, Hideki Mochizuki, Kazuki Tainaka, and Hiroki R. Ueda. "A three-dimensional single-cell-resolution whole-brain atlas using CUBIC-X expansion microscopy and tissue clearing". In: *Nature Neuroscience* 21.4 (Apr. 2018), pp. 625–637. ISSN: 1546-1726.

[99] Casey M. Schneider-Mizell, Agnes L. Bodor, Forrest Collman, Derrick Brittain, Adam A. Bleckert, Sven Dorkenwald, Nicholas L. Turner, Thomas Macrina, Kisuk Lee, Ran Lu, Jingpeng Wu, Jun Zhuang, Anirban Nandi, Brian Hu, JoAnn Buchanan, Marc M. Takeno, Russel Torres, Gayathri Mahalingam, Daniel J. Bumbarger, Yang Li, Tom Chartrand, Nico Kemnitz, William M. Silversmith, Dodam Ih, Jonathan Zung, Aleksandar Zlateski, Ignacio Tartavull, Sergiy Popovych, William Wong, Manuel Castro, Chris S. Jordan, Emmanouil Froudarakis, Lynne Becker, Shelby Suckow, Jacob Reimer, Andreas S. Tolias, Costas Anastassiou, H. Sebastian Seung, R. Clay Reid, and Nuno Maçarico da Costa. "Chandelier cell anatomy and function reveal a variably distributed but common signal". In: *bioRxiv* (Apr. 1, 2020), p. 2020.03.31.018952.

[100] David P. Hoffman, Gleb Shtengel, C. Shan Xu, Kirby R. Campbell, Melanie Freeman, Lei Wang, Daniel E. Milkie, H. Amalia Pasolli, Nirmala Iyer, John A. Bogovic, Daniel R. Stabley, Abbas Shirinifard, Song Pang, David Peale, Kathy Schaefer, Wim Pomp, Chi-Lun Chang, Jennifer Lippincott-Schwartz, Tom Kirchhausen, David J. Solecki, Eric Betzig, and Harald Hess. "Correlative three-dimensional super-resolution and block face electron microscopy of whole vitreously frozen cells". In: *bioRxiv* (Sept. 18, 2019), p. 773986.

[101] Larissa Heinrich, Davis Bennett, David Ackerman, Woohyun Park, John Bogovic, Nils Eckstein, Alyson Petruncio, Jody Clements, C. Shan Xu, Jan Funke, Wyatt Korff, Harald F. Hess, Jennifer Lippincott-Schwartz, Stephan Saalfeld, Aubrey V. Weigel, and COSEM Project Team. "Automatic whole cell organelle segmentation in volumetric electron microscopy". In: *bioRxiv* (Nov. 16, 2020), p. 2020.11.14.382143.

[102] Florian Drawitsch, Ali Karimi, Kevin M Boergens, and Moritz Helmstaedter. "FluoEM, virtual labeling of axons in three-dimensional electron microscopy data for long-range connectomics". In: *eLife* 7 (Aug. 14, 2018). Ed. by Jeremy Nathans and Eve Marder, e38976. ISSN: 2050-084X.

[103] Nicholas I. Clarke and Stephen J. Royle. "FerriTag is a new genetically-encoded inducible tag for correlative light-electron microscopy". In: *Nature Communications* 9.1 (July 4, 2018), p. 2604. ISSN: 2041-1723.

[104] Daniela Boassa, Sakina P. Lemieux, Varda Lev-Ram, Junru Hu, Qing Xiong, Sebastien Phan, Mason Mackey, Ranjan Ramachandra, Ryan Emily Peace, Stephen R. Adams, Mark H. Ellisman, and John T. Ngo. "Split-miniSOG for Spatially Detecting Intracellular Protein-Protein Interactions by Correlated Light and Electron

Microscopy". In: *Cell Chemical Biology* 26.10 (Oct. 17, 2019), 1407–1416.e5. ISSN: 2451-9456.

[105] Eva L. Dyer, William Gray Roncal, Judy A. Prasad, Hugo L. Fernandes, Doga Gürsoy, Vincent De Andrade, Kamel Fezzaa, Xianghui Xiao, Joshua T. Vogelstein, Chris Jacobsen, Konrad P. Körding, and Narayanan Kasthuri. "Quantifying Mesoscale Neuroanatomy Using X-Ray Microtomography". In: *eNeuro* 4.5 (Oct. 16, 2017). ISSN: 2373-2822.

[106] Matheus de Castro Fonseca, Bruno Henrique Silva Araujo, Carlos Sato Baraldi Dias, Nathaly Lopes Archilha, Dionísio Pedro Amorim Neto, Esper Cavalheiro, Harry Westfahl, Antônio José Roque da Silva, and Kleber Gomes Franchini. "High-resolution synchrotron-based X-ray microtomography as a tool to unveil the three-dimensional neuronal architecture of the brain". In: *Scientific Reports* 8.1 (Aug. 13, 2018), p. 12074. ISSN: 2045-2322.

[107] Aaron T. Kuan, Jasper S. Phelps, Logan A. Thomas, Tri M. Nguyen, Julie Han, Chiao-Lin Chen, Anthony W. Azevedo, John C. Tuthill, Jan Funke, Peter Cloetens, Alexandra Pacureanu, and Wei-Chung Allen Lee. "Dense neuronal reconstruction through X-ray holographic nano-tomography". In: *Nature Neuroscience* 23.12 (Dec. 2020), pp. 1637–1643. ISSN: 1546-1726.

[108] Sean Foxley, Vandana Sampathkumar, Vincent De Andrade, Scott Trinkle, Anastasia Sorokina, Katrina Norwood, Patrick La Riviere, and Narayanan Kasthuri. "Multi-modal imaging of a single postmortem mouse brain over five orders of magnitude of resolution". In: *bioRxiv* (Oct. 19, 2020), p. 2020.10.07.329789.

[109] Stephan Saalfeld, Albert Cardona, Volker Hartenstein, and Pavel Tomančák. "As-rigid-as-possible mosaicking and serial section registration of large ssTEM datasets". In: *Bioinformatics* 26.12 (June 15, 2010), pp. i57–i63. ISSN: 1367-4803.

[110] Stephan Saalfeld, Richard Fetter, Albert Cardona, and Pavel Tomancak. "Elastic volume reconstruction from series of ultra-thin microscopy sections". In: *Nature Methods* 9.7 (July 2012), pp. 717–720. ISSN: 1548-7105.

[111] Xiao Yang, Roland Kwitt, Martin Styner, and Marc Niethammer. "Quicksilver: Fast predictive image registration – A deep learning approach". In: *NeuroImage* 158 (Sept. 1, 2017), pp. 378–396. ISSN: 1053-8119.

[112] Viren Jain. "Adversarial Image Alignment and Interpolation". In: *arXiv:1707.00067 [cs]* (June 30, 2017). arXiv: 1707.00067.

[113] Albert Cardona, Stephan Saalfeld, Johannes Schindelin, Ignacio Arganda-Carreras, Stephan Preibisch, Mark Longair, Pavel Tomancak, Volker Hartenstein, and Rodney J. Douglas. "TrakEM2 Software for Neural Circuit Reconstruction". In: *PLOS ONE* 7.6 (June 19, 2012), e38011. ISSN: 1932-6203.

[114] Kevin M. Boergens, Manuel Berning, Tom Bocklisch, Dominic Bräunlein, Florian Drawitsch, Johannes Frohnhofen, Tom Herold, Philipp Otto, Norman Rzepka, Thomas Werkmeister, Daniel Werner, Georg Wiese, Heiko Wissler, and Moritz Helmstaedter. "webKnossos: efficient online 3D data annotation for connectomics". In: *Nature Methods* 14.7 (July 2017), pp. 691–694. ISSN: 1548-7105.

[115] Sven Dorkenwald, Claire McKellar, Thomas Macrina, Nico Kemnitz, Kisuk Lee, Ran Lu, Jingpeng Wu, Sergiy Popovych, Eric Mitchell, Barak Nehoran, Zhen Jia, J. Alexander Bae, Shang Mu, Dodam Ih, Manuel Castro, Oluwaseun Ogedengbe, Akhilesh Halageri, Zoe Ashwood, Jonathan Zung, Derrick Brittain, Forrest Collman, Casey Schneider-Mizell, Chris Jordan, William Silversmith, Christa Baker, David Deutsch, Lucas Encarnacion-Rivera, Sandeep Kumar, Austin Burke, Jay Gager, James Hebditch, Selden Koolman, Merlin Moore, Sarah Morejohn, Ben Silverman, Kyle Willie, Ryan Willie, Szi-chieh Yu, Mala Murthy, and H. Sebastian Seung. "FlyWire: Online community for whole-brain connectomics". In: *bioRxiv* (Aug. 30, 2020), p. 2020.08.30.274225.

[116] Stephan Saalfeld, Albert Cardona, Volker Hartenstein, and Pavel Tomančák. "CATMAID: collaborative annotation toolkit for massive amounts of image data". In: *Bioinformatics* 25.15 (2009), pp. 1984–1986.

[117] Casey M. Schneider-Mizell, Stephan Gerhard, Mark Longair, Tom Kazimiers, Feng Li, Maarten F Zwart, Andrew Champion, Frank Midgley, Richard Fetter, Stephan Saalfeld, and Albert Cardona. "Quantitative neuroanatomy for connectomics in Drosophila". In: *eLife* 5 (2016), e12059.

[118] Marta Costa, James D. Manton, Aaron D. Ostrovsky, Steffen Prohaska, and Gregory S. X. E. Jefferis. "NBLAST: Rapid, Sensitive Comparison of Neuronal Structure and Construction of Neuron Family Databases". In: *Neuron* 91.2 (July 20, 2016), pp. 293–311. ISSN: 0896-6273.

[119] J. Walton. "Lead asparate, an en bloc contrast stain particularly useful for ultrastructural enzymology.:" in: *Journal of Histochemistry & Cytochemistry* (Oct. 1, 1979).

[120] Zhiyuan Lu, C. Shan Xu, Kenneth J. Hayworth, Patricia Rivlin, Stephen M. Plaza, Louis Scheffer, Gerald M. Rubin, Harald F. Hess, and Ian A. Meinertzhagen. "En bloc preparation of Drosophila brains enables high-throughput FIB-SEM connectomics". In: *bioRxiv* (Nov. 27, 2019), p. 855130.

[121] David G. Lowe. "Distinctive Image Features from Scale-Invariant Keypoints". In: *International Journal of Computer Vision* 60.2 (Nov. 1, 2004), pp. 91–110. ISSN: 1573-1405.

[122] D. G. Lowe. "Object recognition from local scale-invariant features". In: *Proceedings of the Seventh IEEE International Conference on Computer Vision*. Proceedings of the Seventh IEEE International Conference on Computer Vision. Vol. 2. Sept. 1999, 1150–1157 vol.2. DOI: 10.1109/ICCV.1999.790410.

[123] Philipp Hanslovsky, John A. Bogovic, and Stephan Saalfeld. "Image-based correction of continuous and discontinuous non-planar axial distortion in serial section microscopy". In: *Bioinformatics* 33.9 (2017), p. 1379.

[124] John A. Bogovic, Igor Pisarev, Philipp Hanslovsky, Neil Thistlethwaite, and Stephan Saalfeld. "N5—a scalable Java API for hierarchies of chunked n-dimensional tensors and structured meta-data". In preparation, 2020.

[125] Igor Pisarev, Philipp Hanslovsky, and Stephan Saalfeld. *n5-spark*. URL: https://github.com/saalfeldlab/n5-spark (visited on 05/01/2020).

[126] Ting Zhao, Donald J. Olbris, Yang Yu, and Stephen M. Plaza. "NeuTu: Software for Collaborative, Large-Scale, Segmentation-Based Connectome Reconstruction". In: *Frontiers in Neural Circuits* 12 (2018). ISSN: 1662-5110.

[127] Philipp Hanslovsky. *Imglyb*. June 3, 2019. URL: https://github.com/imglib/imglyb.

[128] Constantin Pape. *Z5*. Feb. 16, 2020. DOI: 10.5281/zenodo.3585751. URL: https://doi.org/10.5281/zenodo.3585751.

[129] Jeremy Maitin-Shepard. *Neuroglancer*. URL: https://github.com/google/neuroglancer (visited on 05/01/2020).

[130] Wei Ouyang. *ImageJ.js*. Aug. 26, 2020. URL: https://github.com/imjoy-team/imagej.js.

[131] Andrew S. Champion. *rust-n5*. DOI: 10.5281/zenodo.4738789. URL: https://github.com/aschampion/rust-n5 (visited on 05/01/2020).

[132] William Patton, Christopher Barnes, and Andrew S. Champion. *pyn5*. URL: https://github.com/pattonw/rust-pyn5/ (visited on 05/01/2020).

[133] Andrew S. Champion. *n5gest*. DOI: 10.5281/zenodo.4738876. URL: https://github.com/aschampion/n5gest (visited on 05/01/2020).

[134] Andrew S. Champion. *H2N5*. DOI: 10.5281/zenodo.4738862. URL: https://github.com/aschampion/h2n5 (visited on 05/01/2020).

[135] Andrew S. Champion. *n5-wasm*. DOI: 10.5281/zenodo.4738885. URL: https://github.com/aschampion/n5-wasm (visited on 05/01/2020).

[136] Alistair Miles, John Kirkham, Martin Durant, Matthias Bussonnier, James Bourbeau, Tarik Onalan, Joe Hamman, Zain Patel, Matthew Rocklin, shikharsg, Ryan Abernathey, Josh Moore, Vincent Schut, raphael dussin, Elliott Sales de Andrade, Charles Noyes, Aleksandar Jelenak, Anderson Banihirwe, Chris Barnes, George Sakkis, Jan Funke, Jerome Kelleher, Joe Jevnik, Justin Swaney, Poruri Sai Rahul, Stephan Saalfeld, and Tommy Tran. *Zarr*. Oct. 6, 2020. DOI: 10.5281/zenodo.4069231. URL: https://zenodo.org/record/4069231 (visited on 11/19/2020).

[137] Tobias Pietzsch, Stephan Saalfeld, Stephan Preibisch, and Pavel Tomancak. "BigDataViewer: visualization and processing for large image data sets". In: *Nature Methods* 12.6 (June 2015), pp. 481–483. ISSN: 1548-7105.

[138] Benjamin Schmid, Philipp Tripal, Tina Fraaß, Christina Kersten, Barbara Ruder, Anika Grüneboom, Jan Huisken, and Ralf Palmisano. "3Dscript: animating 3D/4D microscopy data using a natural-language-based syntax". In: *Nature Methods* 16.4 (Apr. 2019), pp. 278–280. ISSN: 1548-7105.

[139] Olaf Ronneberger, Philipp Fischer, and Thomas Brox. "U-net: Convolutional networks for biomedical image segmentation". In: *International Conference on Medical Image Computing and Computer-Assisted Intervention*. Springer, 2015, pp. 234–241.

[140] Martín Abadi, Ashish Agarwal, Paul Barham, Eugene Brevdo, Zhifeng Chen, Craig Citro, Greg S. Corrado, Andy Davis, Jeffrey Dean, Matthieu Devin, et al. "Tensorflow: Large-scale machine learning on heterogeneous distributed systems". In: *arXiv preprint arXiv:1603.04467* (2016).

[141] Jan Funke, William Patton, Renate Krause, Julia Buhmann, Rodrigo Lentini, W. Grisaitis, Christopher Barnes, Caroline Malin-Mayor, Larissa Heinrich, Philipp Hanslovsky, Sherry Ding, Andrew Champion, A. Sheridan, and Constantin Pape. *Gunpowder*. URL: https://github.com/funkey/gunpowder (visited on 05/01/2020).

[142] Özgün Çiçek, Ahmed Abdulkadir, Soeren S. Lienkamp, Thomas Brox, and Olaf Ronneberger. "3D U-Net: learning dense volumetric segmentation from sparse annotation". In: *International Conference on Medical Image Computing and Computer-Assisted Intervention*. Springer, 2016, pp. 424–432.

[143] napari contributors. *napari: a multi-dimensional image viewer for python*. Nov. 24, 2020. DOI: 10.5281/zenodo.4289401. URL: https://zenodo.org/record/4289401 (visited on 11/25/2020).

[144] K. Kanatani. "Analysis of 3-D rotation fitting". In: *IEEE Transactions on Pattern Analysis and Machine Intelligence* 16.5 (May 1994), pp. 543–549. ISSN: 1939-3539.

[145] Michał Januszewski, Jeremy Maitin-Shepard, Peter Li, Jörgen Kornfeld, Winfried Denk, and Viren Jain. "Flood-filling networks". In: *arXiv preprint arXiv:1611.00421* (2016).

[146] Peter H. Li, Larry F. Lindsey, Michał Januszewski, Zhihao Zheng, Alexander Shakeel Bates, István Taisz, Mike Tyka, Matthew Nichols, Feng Li, Eric Perlman, Jeremy Maitin-Shepard, Tim Blakely, Laramie Leavitt, Gregory S. X. E. Jefferis, Davi Bock, and Viren Jain. "Automated Reconstruction of a Serial-Section EM Drosophila Brain with Flood-Filling Networks and Local Realignment". In: *bioRxiv* (Aug. 4, 2019), p. 605634.

[147] Andrew S. Champion. *Diluvian: flood filling networks for segmenting electron microscopy of neural tissue*. 2017. DOI: 10.5281/zenodo.4738889. URL: https://github.com/aschampion/diluvian.

[148] François Chollet et al. *Keras*. GitHub, 2015. URL: https://github.com/fchollet/keras.

[149] Kaiming He, Xiangyu Zhang, Shaoqing Ren, and Jian Sun. "Identity mappings in deep residual networks". In: *European Conference on Computer Vision*. Springer, 2016, pp. 630–645.

[150] Mie Sato, Ingmar Bitter, Michael A. Bender, Arie E. Kaufman, and Masayuki Nakajima. "TEASAR: Tree-structure extraction algorithm for accurate and robust skeletons". In: *Computer Graphics and Applications, 2000. Proceedings. The Eighth Pacific Conference on*. IEEE, 2000, pp. 281–449.

[151] Ingmar Bitter, Arie E. Kaufman, and Mie Sato. "Penalized-distance volumetric skeleton algorithm". In: *IEEE Transactions on Visualization and computer Graphics* 7.3 (2001), pp. 195–206.

[152] George Karypis and Vipin Kumar. "A fast and high quality multilevel scheme for partitioning irregular graphs". In: *SIAM Journal on Scientific Computing* 20.1 (1998), pp. 359–392.

[153] William Patton. *CATMAID-autoproofreader*. URL: https://github.com/pattonw/CATMAID-autoproofreader (visited on 11/05/2020).

[154] Manuel Forero, Jenny Pennack, Rocío Anabel, and Alicia Hidalgo. "DeadEasy Caspase: Automatic Counting of Apoptotic Cells in Drosophila". In: *PloS one* 4 (Feb. 1, 2009), e5441.

[155] Stephan Preibisch, Stephan Saalfeld, Johannes Schindelin, and Pavel Tomancak. "Software for bead-based registration of selective plane illumination microscopy data". In: *Nature Methods* 7.6 (June 2010), pp. 418–419. ISSN: 1548-7105.

[156] Elizabeth M.C. Hillman, Venkatakaushik Voleti, Wenze Li, and Hang Yu. "Light-Sheet Microscopy in Neuroscience". In: *Annual Review of Neuroscience* 42.1 (2019), pp. 295–313.

[157] Paul J. Besl and Neil D. McKay. "Method for registration of 3-D shapes". In: *Sensor Fusion IV: Control Paradigms and Data Structures*. Sensor Fusion IV: Control Paradigms and Data Structures. Vol. 1611. International Society for Optics and Photonics, Apr. 30, 1992, pp. 586–606. DOI: 10.1117/12.57955. URL: https://www.spiedigitallibrary.org/conference-proceedings-of-spie/1611/0000/Method-for-registration-of-3-D-shapes/10.1117/12.57955.short (visited on 11/28/2020).

[158] Steven Gold, Anand Rangarajan, Chien-Ping Lu, Suguna Pappu, and Eric Mjolsness. "New algorithms for 2D and 3D point matching: pose estimation and correspondence". In: *Pattern Recognition* 31.8 (Aug. 1, 1998), pp. 1019–1031. ISSN: 0031-3203.

[159] H. Huang, L. Shen, R. Zhang, F. Makedon, A. Saykin, and J. Pearlman. "A Novel Surface Registration Algorithm With Biomedical Modeling Applications". In: *IEEE Transactions on Information Technology in Biomedicine* 11.4 (July 2007), pp. 474–482. ISSN: 1558-0032.

[160] Luming Liang, Mingqiang Wei, Andrzej Szymczak, Anthony Petrella, Haoran Xie, Jing Qin, Jun Wang, and Fu Lee Wang. "Nonrigid iterative closest points for registration of 3D biomedical surfaces". In: *Optics and Lasers in Engineering* 100 (Jan. 1, 2018), pp. 141–154. ISSN: 0143-8166.

[161] Jean Feydy, Benjamin Charlier, François-Xavier Vialard, and Gabriel Peyré. "Optimal Transport for Diffeomorphic Registration". In: *Medical Image Computing and Computer Assisted Intervention - MICCAI 2017*. Ed. by Maxime Descoteaux, Lena Maier-Hein, Alfred Franz, Pierre Jannin, D. Louis Collins, and Simon Duchesne. Lecture Notes in Computer Science. Cham: Springer International Publishing, 2017, pp. 291–299. ISBN: 978-3-319-66182-7. DOI: 10.1007/978-3-319-66182-7_34.

[162] A. Myronenko and X. Song. "Point Set Registration: Coherent Point Drift". In: *IEEE Transactions on Pattern Analysis and Machine Intelligence* 32.12 (Dec. 2010), pp. 2262–2275. ISSN: 1939-3539.

[163] Martin Simonovsky, Benjamín Gutiérrez-Becker, Diana Mateus, Nassir Navab, and Nikos Komodakis. "A Deep Metric for Multimodal Registration". In: *Medical Image Computing and Computer-Assisted Intervention - MICCAI 2016*. Ed. by Sebastien Ourselin, Leo Joskowicz, Mert R. Sabuncu, Gozde Unal, and William Wells. Lecture Notes in Computer Science. Cham: Springer International Publishing, 2016, pp. 10–18. ISBN: 978-3-319-46726-9. DOI: 10.1007/978-3-319-46726-9_2.

[164] F. G. Prendergast and K. G. Mann. "Chemical and physical properties of aequorin and the green fluorescent protein isolated from Aequorea forskålea". In: *Biochemistry* 17.17 (Aug. 22, 1978), pp. 3448–3453. ISSN: 0006-2960.

[165] Nathan C. Shaner, Robert E. Campbell, Paul A. Steinbach, Ben N. G. Giepmans, Amy E. Palmer, and Roger Y. Tsien. "Improved monomeric red, orange and yellow fluorescent proteins derived from Discosoma sp. red fluorescent protein". In: *Nature Biotechnology* 22.12 (Dec. 2004), pp. 1567–1572. ISSN: 1546-1696.

[166] Stephan Preibisch, Fernando Amat, Evangelia Stamataki, Mihail Sarov, Robert H. Singer, Eugene Myers, and Pavel Tomancak. "Efficient Bayesian-based multiview deconvolution". In: *Nature Methods* 11.6 (2014), pp. 645–648.

[167] Katie McDole, Léo Guignard, Fernando Amat, Andrew Berger, Grégoire Malandain, Loïc A. Royer, Srinivas C. Turaga, Kristin Branson, and Philipp J. Keller. "In Toto Imaging and Reconstruction of Post-Implantation Mouse Development at the Single-Cell Level". In: *Cell* 175.3 (Oct. 18, 2018), 859–876.e33. ISSN: 0092-8674.

[168] Fernando Amat, Burkhard Höckendorf, Yinan Wan, William C. Lemon, Katie McDole, and Philipp J. Keller. "Efficient processing and analysis of large-scale light-sheet microscopy data". In: *Nature Protocols* 10.11 (Nov. 2015), pp. 1679–1696. ISSN: 1750-2799.

[169] J. A. Bogovic, P. Hanslovsky, A. Wong, and S. Saalfeld. "Robust registration of calcium images by learned contrast synthesis". In: *2016 IEEE 13th International Symposium on Biomedical Imaging (ISBI)*. 2016 IEEE 13th International Symposium on Biomedical Imaging (ISBI). ISSN: 1945-8452. Apr. 2016, pp. 1123–1126. DOI: 10.1109/ISBI.2016.7493463.

[170] Stuart Berg, Dominik Kutra, Thorben Kroeger, Christoph N. Straehle, Bernhard X. Kausler, Carsten Haubold, Martin Schiegg, Janez Ales, Thorsten Beier, Markus Rudy, Kemal Eren, Jaime I. Cervantes, Buote Xu, Fynn Beuttenmueller, Adrian Wolny, Chong Zhang, Ullrich Koethe, Fred A. Hamprecht, and Anna Kreshuk. "ilastik: interactive machine learning for (bio)image analysis". In: *Nature Methods* 16.12 (Dec. 2019), pp. 1226–1232. ISSN: 1548-7105.

[171] Nathan W. Gouwens and Rachel I. Wilson. "Signal Propagation in Drosophila Central Neurons". In: *Journal of Neuroscience* 29.19 (May 13, 2009), pp. 6239–6249. ISSN: 0270-6474, 1529-2401.

[172] Adrian V. Dalca, Guha Balakrishnan, John Guttag, and Mert R. Sabuncu. "Unsupervised learning of probabilistic diffeomorphic registration for images and surfaces". In: *Medical Image Analysis* 57 (Oct. 1, 2019), pp. 226–236. ISSN: 1361-8415.

[173] Zhe Xu, Jie Luo, Jiangpeng Yan, Ritvik Pulya, Xiu Li, William Wells, and Jayender Jagadeesan. "Adversarial Uni- and Multi-modal Stream Networks for Multimodal Image Registration". In: *Medical Image Computing and Computer Assisted Intervention – MICCAI 2020*. Ed. by Anne L. Martel, Purang Abolmaesumi, Danail Stoyanov, Diana Mateus, Maria A. Zuluaga, S. Kevin Zhou, Daniel Racoceanu, and Leo Joskowicz. Lecture Notes in Computer Science. Cham: Springer International Publishing, 2020, pp. 222–232. ISBN: 978-3-030-59716-0. DOI: 10.1007/978-3-030-59716-0_22.

[174] David Hörl, Fabio Rojas Rusak, Friedrich Preusser, Paul Tillberg, Nadine Randel, Raghav K. Chhetri, Albert Cardona, Philipp J. Keller, Hartmann Harz, Heinrich Leonhardt, Mathias Treier, and Stephan Preibisch. "BigStitcher: reconstructing high-resolution image datasets of cleared and expanded samples". In: *Nature Methods* 16.9 (Sept. 2019), pp. 870–874. ISSN: 1548-7105.

[175] James Munkres. "Algorithms for the Assignment and Transportation Problems". In: *Journal of the Society for Industrial and Applied Mathematics* 5.1 (Mar. 1, 1957), pp. 32–38. ISSN: 0368-4245.

[176] François Bourgeois and Jean-Claude Lassalle. “An extension of the Munkres algorithm for the assignment problem to rectangular matrices”. In: *Communications of the ACM* 14.12 (Dec. 1, 1971), pp. 802–804. ISSN: 0001-0782.

[177] Alexander Shakeel Bates, James D Manton, Sridhar R Jagannathan, Marta Costa, Philipp Schlegel, Torsten Rohlfing, and Gregory SXE Jefferis. “The natverse, a versatile toolbox for combining and analysing neuroanatomical data”. In: *eLife* 9 (Apr. 14, 2020). Ed. by K VijayRaghavan, e53350. ISSN: 2050-084X.